Surface Current Determination from Localized Measurements

Final Report

for

Contract No. N00014-97-1-0209

Submitted by: Signature Technology Laboratory
Georgia Tech Research Institute
Atlanta, GA 30332

DISTRIBUTION STATEMENT AUTHORIZATION RECORD

Title: Surface Current Determination from Localized Measurements

Authorizing Official: Ronald Radlinski

Agency: ONR Ph. No. (703) 696-0987

☐ Internet Document: URL: _____
(DTIC-OCA Use Only)

Distribution Statement: (Authorized by the source above.)

☒ **A:** Approved for public release, distribution unlimited.

☐ **B:** U. S. Government agencies only. (Fill in reason and date applied). Other requests shall be referred to (Insert controlling office).

☐ **C:** U. S. Government agencies and their contractors. (Fill in reason and date applied). Other requests shall be referred to (Insert controlling office).

☐ **D:** DoD and DoD contractors only. (Fill in reason and date applied). Other requests shall be referred to (Insert controlling office).

☐ **E:** DoD components only. (Fill in reason and date applied). Other requests shall be referred to (Insert controlling office).

☐ **F:** Further dissemination only as directed by (Insert controlling DoD office and date), or higher authority.

☐ **X:** U. S. Government agencies and private individuals or enterprises eligible to obtain export-controlled technical data in accordance with DoD Directive 5230.25.

NOTES: Submitted without a distribution statement

J Keith
DTIC Point of Contact

14 Mar 2000
Date

REPORT DOCUMENTATION PAGE

Form Approved
OMB No. 0704-0188

1. AGENCY USE ONLY *(Leave blank)*	2. REPORT DATE	3. REPORT TYPE AND DATES COVERED
	29 Feb 2000	**Final Report, 1 Jan 1997 to 31 Dec 1999**

4. TITLE AND SUBTITLE
Determination of Body Surface Currents from Localized Measurements

5. FUNDING NUMBERS
C - N00014-97-1-0209

6. AUTHORS
Morris P. Kesler, Jim Maloney, Paul Harms, Stephen Blalock, Eric Kuster and Glenn Smith

7. PERFORMING ORGANIZATION NAME(S) AND ADDRESS(ES)
Georgia Tech Research Institute
Atlanta, GA 30332

8. PERFORMING ORGANIZATION REPORT NUMBER

9. SPONSORING/MONITORING AGENCY NAME(S) AND ADDRESS(ES)
Office of Naval Research (ONR 334)
Ship Structures and Systems S&T Division
800 N. Quincy St.
Arlington, VA 22217-5660

10. SPONSORING/MONITORING AGENCY REPORT NUMBER

11. SUPPLEMENTARY NOTES

12a. DISTRIBUTION/AVAILABILITY STATEMENT
DISTRIBUTION STATEMENT A
Approved for Public Release
Distribution Unlimited

12b. DISTRIBUTION CODE

13. ABSTRACT *(Maximum 200 words)*

This report describes the results of a research program aimed at developing and demonstrating a technique for determining surface currents from a series of electromagnetic field measurements. Two back-propagation techniques were developed and validated through numerical simulations and measurements on laboratory-scale, conducting objects. The first technique is a planar spectral decomposition approach that utilizes magnetic field measurements on a plane in front of the body, and the second is a local back-propagation technique that operates using magnetic field measurements at a much smaller number of sample points. The back-propagation techniques were demonstrated through measurements on a series of laboratory-scale targets, including solid metallic plates, metallic plates with slots, and more complex objects, such as a scale-model ship and a frequency selective surface. The back-propagated results were compared to predictions of the surface current obtained using a finite-difference time-domain numerical code. The predicted and experimental results are in agreement, validating the back-propagation approaches for these targets.

This report contains a description and analysis of the back-propagation techniques, details of the measurements, and representative results.

14. SUBJECT TERMS
Electromagnetic scattering; back-propagation; microwave holography; surface currents

15. NUMBER OF PAGES
132

16. PRICE CODE

17. SECURITY CLASSIFICATION OF REPORT	18. SECURITY CLASSIFICATION OF THIS PAGE	19. SECURITY CLASSIFICATION OF ABSTRACT	20. LIMITATION OF ABSTRACT
UNCLASSIFIED	**UNCLASSIFIED**	**UNCLASSIFIED**	

Table of Contents

List of Figures

1 Executive Summary

This report culminates a three-year basic research program conducted by the Signature Technology Laboratory (STL) at the Georgia Tech Research Institute (GTRI). The underlying principle motivating this research effort is the fact that the surface current on an object completely characterizes its scattering behavior. Thus, knowledge of the surface current can be critical in understanding the scattering behavior of an object and how that scattering can be controlled. Unfortunately, there is no direct way to measure the surface current without modifying the object, for example, by incorporating magnetic field probes on the surface of the object. This effort was focused on developing and evaluating alternative techniques that do not require modification of the object under test. Such techniques utilize electromagnetic field measurements near, but not directly on, the surface of the object. A back-propagation procedure, using the field values from this secondary surface, can be employed to determine the magnetic field directly at the surface.

The major accomplishment of the research program is the development of two back-propagation techniques, validated through numerical simulations and measurements on laboratory-scale, conducting objects. The first technique is a planar spectral decomposition approach that utilizes magnetic field measurements on a plane in front of the body, and the second is a local back-propagation technique that operates using magnetic field measurements at a much smaller number of sample points. The first approach employs spectral and spatial filtering of the measured signal to capture the propagating spectrum as well as a portion of the evanescent spectrum. This technique is basically the electromagnetic version of the near field acoustic holography (NAH) method [1-4] and is similar to the microwave holography method [5]. Special consideration is given to avoiding exponential amplification of measurement noise during back-propagation of the evanescent spectrum. The local approach utilizes an optimal combination of a smaller number of measurements to estimate the surface current. The advantage of the local probe technique is that the surface current at key locations can be determined rapidly, without requiring a full set of measurements be performed.

Extensive numerical simulations of the back-propagation techniques were used to determine the potential performance of each technique and to determine the impact of key parameters; such as distance from the object to the measurement surface, spacing between measurement points, the

extent of the measurement surface, and measurement noise. These simulations were used to design an appropriate measurement configuration to demonstrate the techniques.

The back-propagation techniques were demonstrated through measurements on a series of laboratory-scale targets. Measurements have been completed for solid metallic plates, metallic plates with slots, and more complex objects, such as a scale-model ship and a small area of a frequency selective surface (FSS). A horn antenna was used to illuminate the targets, and the magnetic field was measured on a surface parallel to the front surface of the object, approximately a distance of 0.1λ in front. The magnetic field data were back-propagated to the surface of the plate to determine the surface current. The back-propagated results were compared to predictions of the surface current obtained using a finite-difference time-domain numerical code. The predicted and experimental results are in agreement, validating the back-propagation approaches for these conducting objects.

One application of the back-propagation technique is to determine the electromagnetic performance of an object or a sub-system of an object. This becomes more important when signature control is required. For example, frequency-selective surfaces are used to control the out-of-band signature of antennas. For best performance, the FSS must be carefully integrated into the surface of the vessel. It is difficult to determine from a visual inspection whether the integration has been adequately accomplished. The measurement and back-propagation procedures developed in this program may help with this problem. Thus, part of our effort was to apply the techniques to more complex surfaces that include, for example, an FSS, to explore the potential for this type of application.

The report is organized as follows. Section 2 presents the full back-propagation technique, while Sections 3 and 4 describe the studies performed to evaluate the performance of the technique and the impact of the key parameters. More rigorous modeling of potential measurement configurations is described in Section 5, leading into the measurement results contained in Section 6. Back-propagation using the local technique is described in Section 7 along with some measured results to show its performance. Sections 8 and 9 describe the measurements performed on more complex targets (FSS and scale model ship). Finally, Section 10 contains an evaluation of applying the full back-propagation technique to a tilted surface.

2 Back-Propagation Method

This section will describe the back-propagation method for the general case, and then the methodology employed in the two-dimensional study will be derived. Finally, the equations used with the actual three-dimensional measurements will be presented.

The goal of this approach is to obtain the surface current distribution from the field measurements on a scan plane in front of the object. The fields will be sampled at a finite number of points on the two-dimensional, finite scan plane and then filtered and back-propagated to compute the currents on the test object. This approach relies on Huygen's principle and uniqueness concepts in electromagnetics [9]. Accordingly, the fields within a volume of space (without sources) enclosed completely by a surface can be computed from the tangential electric or magnetic field over the whole enclosing surface or from the tangential electric field components over part of the surface and the tangential magnetic field over the rest of the surface.

To reduce the complexity of the measurements, only the tangential electric or magnetic field components are measured, and the scan plane covers only a finite portion of the enclosing surface. The use of a finite scan plane size assumes the fields are significant only on the scan plane and are negligible everywhere else. This approach is sufficient if most of the energy passes through the scan plane; this occurs, for example, if the current is distributed over a finite surface and radiates in a dominant direction, and the scan plane is large enough to capture this field. Thus, the tangential electric or magnetic field measured at the scan plane is sufficient for determining the surface current if the majority of the radiated and evanescent fields from the surface current pass through the plane.

The algorithms used in this study of the back-propagation method in two and three dimensions are divided into two parts. The first part is the forward propagation algorithm, which computes the magnetic or electric fields due to the known surface current and propagates them out to the scan or measurement plane. These field components become the simulated measured fields. To model measurement conditions, the fields are processed; for example, noise is added to them in the spatial domain. In actual measurements, this algorithm will be replaced by the measurements themselves. The second part of the simulations is the back-propagation algorithm that is used to back-propagate these fields to the test object. From these the surface current is reconstructed and compared with the original current distribution. In this fashion many parameters of the back-

propagation technique are studied so that interrelationships between them and the feasibility of the technique can be determined.

Every simulation, except for the FDTD analysis, is performed using Matlab on a personal computer with a 200 MHz Pentium processor and up to 64 Megabytes of memory. For the simple two-dimensional problems that are initially employed to study this approach, numerical errors are kept minimal by making the spatial cell size 0.02 λ or 50 samples per wavelength. This can be done for the two-dimensional problem without requiring excessive computer memory or run times. The spatial cell size is reduced further when dimensions on the order of 0.1 λ are studied. In addition, typically 2^{16} points are used in modeling the current and field distributions to make efficient use of the FFT algorithm in Matlab. These parameters provide sufficient resolution and tolerable aliasing levels for our modeling purposes.

For the three-dimensional simulations, which require two-dimensional arrays, it is more difficult to employ a large number of points. Given the personal computer limitations, a total of approximately 2^8 and 2^9 samples per dimension can be used, which amounts to a two-dimensional grid of 256x256 or 512x512 points. With 20 – 30 samples per wavelength, this number of points provides a modeling domain of approximately 11x11 λ which is sufficient for our three-dimensional studies.

The following formulations assume harmonic time dependence with an $e^{j\omega t}$ factor throughout, and all dimensions are given in terms of the free space wavelength [9].

2.1 Two-Dimensional Forward Propagation Model

The geometry for the two-dimensional formulation is shown in Figure 2-1. In this figure, the y directed surface current is contained in the x-y plane, and z is normal to the surface. The variable s is the distance in z from the measurement plane, or line in the two-dimensional case, to the surface current, and d is the width in x of the current.

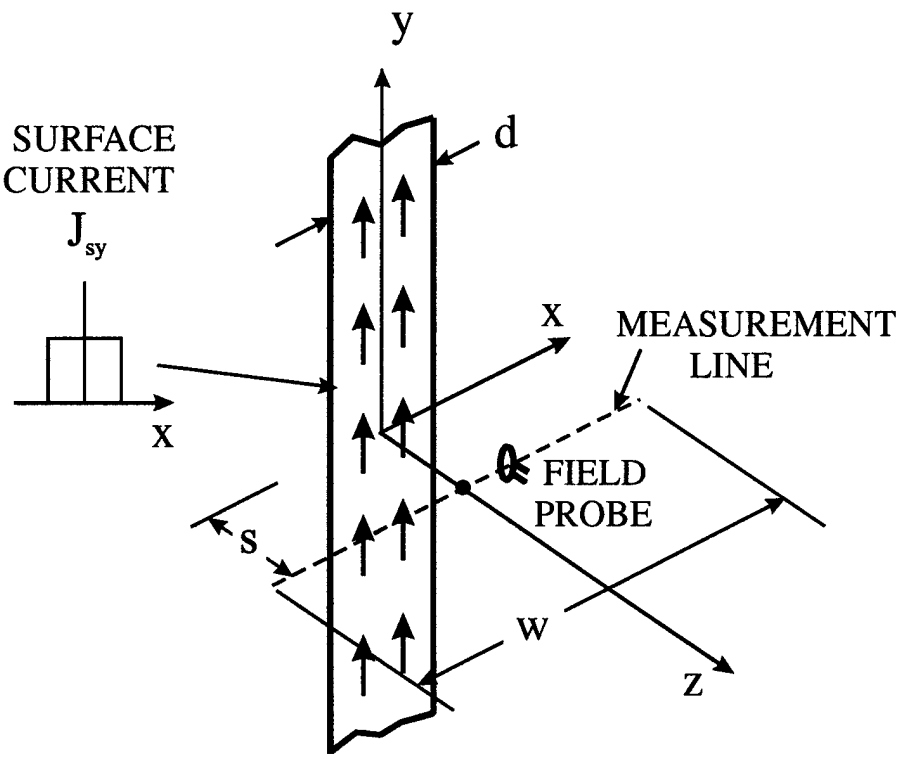

Figure 2-1 Two-dimensional geometry for back-propagation study.

The first steps involve generating the measured field at the measurement line from the assumed current distribution. Given a current distribution which is a pulse

$$J_y(x)=\begin{cases}1, & |x|\le d/2\\ 0, & |x|>d/2\end{cases} \tag{2.1}$$

on the plane $z=0$, the tangential component of the magnetic field due to this current is

$$H_x\left(x,z=0^+\right)=\frac{1}{2}J_y(x). \tag{2.2}$$

To propagate the fields of the current in the half-space $z>0$, they are expressed in the spectral domain by taking the Fourier Transform of (2.2) giving

$$\tilde{H}_x\left(k_x,z=0^+\right)=\int_{-\infty}^{\infty}H_x\left(x,z=0^+\right)e^{jk_x x}dx, \tag{2.3}$$

which for the pulse of current is the Sinc function. Note that for this two-dimensional problem, the field components are $\tilde{H}_x,\tilde{H}_z,\tilde{E}_y$. However, only the tangential (x and y) components are needed for

the back-propagation procedure, so the z components will not be discussed. If the electric field is being simulated, it can be obtained from the magnetic field via Maxwell's equation,

$$\tilde{E}_y = -\eta \frac{k_0}{k_z} \tilde{H}_x \tag{2.4}$$

where η is the impedance of free space, k_0 is the propagation constant in free space and

$$k_z = \begin{cases} \sqrt{k_0^2 - k_x^2}, & |k_x| \le k_0 \\ -j\sqrt{k_x^2 - k_0^2}, & |k_x| > k_0 \end{cases} \tag{2.5}$$

The field at the measurement line is found by propagating the plane wave spectrum to the measurement line with the plane wave propagation factor. For example, the magnetic field is propagated using

$$\tilde{H}_x(k_x, z = s) = \tilde{H}_x(k_x, z = 0^+) e^{-jk_z s}, \tag{2.6}$$

where k_z is given in (2.5). The fields in the spatial domain at the measurement line are then given by

$$H_x(x, z = s) = \frac{1}{2\pi} \int_{-\infty}^{\infty} \tilde{H}_x(k_x, z = 0^+) e^{-jk_x x} e^{-jk_z s} dk_x, \tag{2.7}$$

and, if the electric field is needed, it is given by

$$E_y(x, z = s) = -\eta k_0 \frac{1}{2\pi} \int_{-\infty}^{\infty} \frac{1}{k_z} \tilde{H}_x(k_x, z = 0^+) e^{-jk_x x} e^{-jk_z s} dk_x. \tag{2.8}$$

2.2 Two-Dimensional Back-Propagation Model

The next set of equations describe the back-propagation model. Once the fields tangential to the measurement line are known, they are processed in order to model the characteristics of the actual measurement equipment,

$$\begin{Bmatrix} E_y \\ H_x \end{Bmatrix} \xrightarrow{\substack{measurement \\ process}} \begin{Bmatrix} E_y^m \\ H_x^m \end{Bmatrix}. \tag{2.9}$$

The superscript 'm' indicates measured field component. For example, Gaussian noise is added to the spatial fields to simulate some types of measurement noise. After the fields are processed they are transformed into the spectral domain according to the equation

$$\tilde{H}_x^m(k_x, z=s) = \int_{-\infty}^{\infty} H_x^m(x, z=s) e^{jk_x x} dx \tag{2.10}$$

A spectral domain filter is then applied. This reduces the noise that dominates the signal at the high end of the spectrum. The filter is implemented by the equation

$$\tilde{H}_x^{mf}(k_x, z=s) = \tilde{H}_x^m(k_x, z=s)\,\text{filter}(k_x) \tag{2.11}$$

where the superscript 'f' indicates a field component filtered in the spectral domain. The filter employed in this report is given by

$$\text{filter}(k_x) = \begin{cases} 1.0, & k_x \le \alpha k_{cut} \\ e^{-(k_x - \alpha k_{cut})^2/\gamma^2}, & k_x > \alpha k_{cut} \end{cases} \tag{2.12}$$

with

$$\gamma = (1-\alpha)\sqrt{\frac{k_{cut}}{s}}\,. \tag{2.13}$$

The filter in (2.12) was devised to sufficiently dampen out the noise in the evanescent spectrum at the measurement line/plane, otherwise, the back-propagator causes this noisy evanescent spectrum to grow and swamp the actual signal or current at the surface. The filter is flat until αk_{cut}, and then it falls off rapidly with a Gaussian-shaped roll-off to dampen any noise without adding excessive ringing as would occur with a flat filter. The value of α determines the starting point and in conjunction with γ the sharpness of the roll off. A value of approximately 0.9 or greater causes the filter to fall rapidly beyond αk_{cut}, approximating a flat filter, and a value of approximately 0.5 causes it to behave similar to the Hamming window. The value of k_{cut} was generally chosen as the point where the actual spectrum, i.e., without noise, was four standard deviations above the average noise level. A comparison of the Hamming window and filter in (2.12) is shown in Figure 2-2.

After being filtered, the plane wave spectrum is back-propagated with the equation

$$\tilde{H}_x^{fm}\left(k_x, z=0^+\right) = \tilde{H}_x^{fm}\left(k_x, z=s\right)e^{+jk_z s} \tag{2.14}$$

and it is transformed into the spatial domain via

$$H_x^{fm}\left(x, z=0^+\right) = \frac{1}{2\pi}\int_{-\infty}^{\infty} \tilde{H}_x^{fm}\left(k_x, z=0^+\right)e^{-jk_x x}dk_x \tag{2.15}$$

The measured or reconstructed current distribution is obtained from the equation

$$J_y^{fm} = 2H_x^{fm}\left(x, z=0^+\right) \tag{2.16}$$

This current is compared with the original current to determine the effectiveness of the method for ranges of various parameters as will be discussed in section 3.

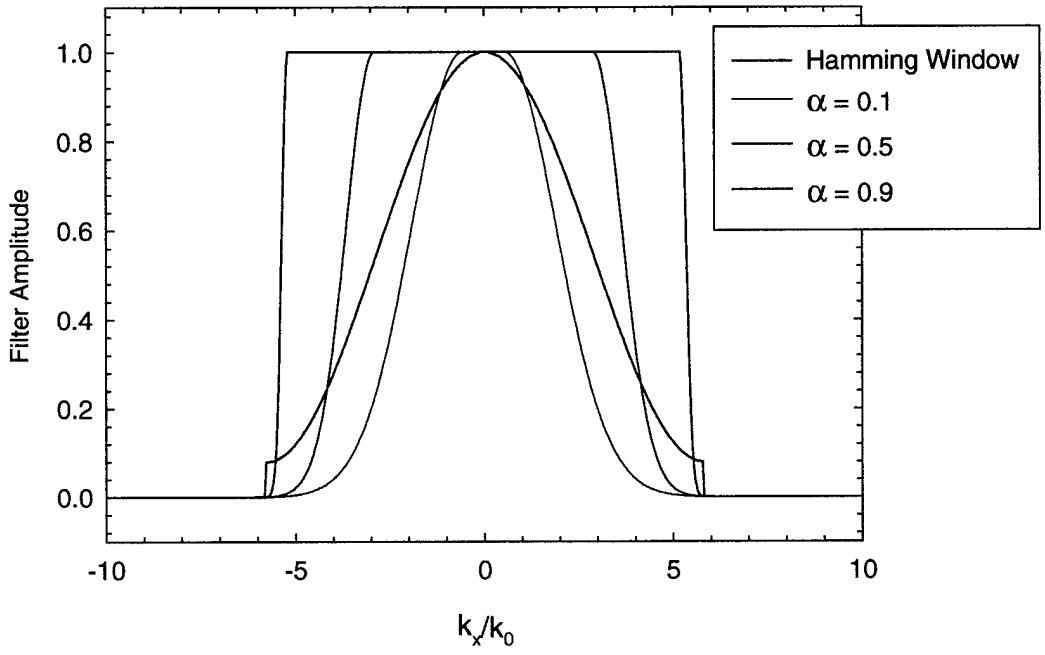

Figure 2-2 Comparison of the Hamming window with the filter for α = 0.1, 0.5 and 0.9 (k_{cut}/k_0 = 5.8).

2.3 Three-Dimensional Forward Propagation Model

The geometry for the three-dimensional formulation is shown in Figure 2-3. In this figure, the *y* directed surface current is distributed over a square patch (dxd) contained on the *x*-*y* plane, and *z* is normal to the surface. The variable s is the distance in *z* from the measurement plane to the

surface current, and w is the width and height of the square measurement or scan plane. All dimensions are given in terms of λ.

The first step involves generating the measured field at the measurement plane from the current distribution. Given a current distribution which is a pulse

$$J_y(x,y)=\begin{cases}1., |x|\cap|y|\le d/2\\ 0., |x|\cup|y|>d/2\end{cases}, \tag{2.17}$$

on the plane $z=0^+$, the tangential component of the magnetic field is

$$H_x\left(x,y,z=0^+\right)=\frac{1}{2}J_y(x,y) \tag{2.18}$$

To propagate the field of the current in the half-space $z>0^+$, they are expressed in the spectral domain by taking the Fourier Transform of (2.18) giving

$$\tilde{H}_x\left(k_x,k_y,z=0^+\right)=\iint_{\infty} H_x\left(x,y,z=0^+\right)e^{jk_x x}e^{jk_y y}dxdy, \tag{2.19}$$

which for the pulse of current is the two-dimensional sinc function. Note that for this problem $\tilde{H}_y=0$ due to the assumed current distribution. However, in general for z > 0^+ all six field components are nonzero. The tangential electric field can be obtained from the tangential magnetic field using Maxwell's equations [9],

$$\tilde{E}_y=-\eta\frac{k_0}{k_z}\left(\left(1-\left(\frac{k_y}{k_0}\right)^2\right)\tilde{H}_x+\frac{k_xk_y}{k_0^2}\tilde{H}_y\right) \tag{2.20}$$

and

$$\tilde{E}_x=\eta\frac{k_0}{k_z}\left(\left(1-\left(\frac{k_x}{k_0}\right)^2\right)\tilde{H}_y+\frac{k_xk_y}{k_0^2}\tilde{H}_x\right) \tag{2.21}$$

where k_x and k_y are the spectral domain independent variables, and

$$k_z = \begin{cases} \sqrt{k_0^2 - k_x^2 - k_y^2}, & k_x^2 + k_y^2 \le k_0^2 \\ -j\sqrt{k_x^2 + k_y^2 - k_0^2}, & k_x^2 + k_y^2 > k_0^2 \end{cases}. \tag{2.22}$$

The z field components can be readily computed from Maxwell's equations but are not used in the algorithm. Once the plane wave spectrum is computed, it is propagated to the measurement plane with the plane wave propagation factor. For example, the magnetic field is propagated using

$$\tilde{H}_x(k_x, k_y, z = s) = \tilde{H}_x(k_x, k_y, z = 0^+) e^{-jk_z s} \tag{2.23}$$

where k_z is given in (2.22). The spatial domain fields at the measurement plane are then given by

$$H_x(x, y, z = s) = \frac{1}{4\pi^2} \int_{-\infty}^{\infty} \int_{-\infty}^{\infty} \tilde{H}_x(k_x, k_y, z = 0^+) e^{-jk_x x} e^{-jk_y y} e^{-jk_z s} dk_x dk_y , \tag{2.24}$$

and similarly for the other tangential components.

2.4 Three-Dimensional Back-Propagation Model

Once the field tangential to the measurement plane is known, it is processed in order to model the characteristics of the actual measurement equipment as shown in (2.9). For example, Gaussian noise is added to the spatial fields to simulate some types of measurement noise to give

$$\begin{Bmatrix} H_x \\ H_y \\ E_x \\ E_y \end{Bmatrix} \xrightarrow{\text{measurement process}} \begin{Bmatrix} H_x^m \\ H_y^m \\ E_x^m \\ E_y^m \end{Bmatrix} \tag{2.25}$$

where the superscript 'm' again indicates measured field component. All four tangential field components are shown for completeness. After the field is processed it is transformed back into the spectral domain according to the equation

$$\tilde{H}_x^m(k_x, k_y, z = s) = \int_{-\infty}^{\infty} \int_{-\infty}^{\infty} H_x^m(x, y, z = s) e^{jk_x x} e^{jk_y x} dxdy \tag{2.26}$$

Then, as in the two-dimensional case, a spectral domain filter is applied to reduce the noise. The filter is implemented by the equation

$$\tilde{H}_x^{mf}\left(k_x,k_y,z=s\right)=\tilde{H}_x^{m}\left(k_x,k_y,z=s\right)\text{filter}\left(k_x,k_y\right) \tag{2.27}$$

where the superscript 'f' again indicates spectral-filtered field component. The filter is an extension of the one-dimensional filter (2.12):

$$\text{filter}\left(k_x,k_y\right)=f\left(k_x\right)f\left(k_y\right), \tag{2.28}$$

where

$$f\left(k_i\right)=\begin{cases}1.0, & k_i\le\alpha k_{icut}\\ e^{-\left(k_i-\alpha k_{icut}\right)^2/\gamma_i^2}, & k_i\ge\alpha k_{icut}\end{cases} \tag{2.29}$$

and

$$\gamma_i=\left(1-\alpha\right)\sqrt{\frac{k_{icut}}{s}} \tag{2.30}$$

with $i=x,y$. Note the filter is unity over a rectangular domain. Similar to the one-dimensional filter, the value of α determines the starting point and sharpness of the roll off, and k_{icut} is the highest spectral component (k_x or k_y)of interest. A value of α of approximately 0.9 or greater causes the filter to fall rapidly beyond k_{icut}, approximating a two-dimensional flat filter, and a value of approximately 0.5 causes it to behave similarly to the two-dimensional Hamming window.

After being filtered, the plane wave spectrum is back-propagated with the equation

$$\tilde{H}_x^{fm}\left(k_x,k_y,z=0^+\right)=\tilde{H}_x^{fm}\left(k_x,k_y,z=s\right)e^{+jk_zs}. \tag{2.31}$$

Next, it is transformed into the spatial domain via

$$H_x^{fm}\left(x,y,z=0^+\right)=\frac{1}{4\pi^2}\int_{-\infty}^{\infty}\int_{-\infty}^{\infty}\tilde{H}_x^{fm}\left(k_x,k_y,z=0^+\right)e^{-jk_xx}e^{-jk_yy}dk_xdk_y. \tag{2.32}$$

The measured or reconstructed current distribution is obtained from the equation

$$J_y^{fm}=2H_x^{fm}\left(x,y,z=0^+\right) \tag{2.33}$$

This current distribution is compared with the original surface current to determine the effectiveness of the method.

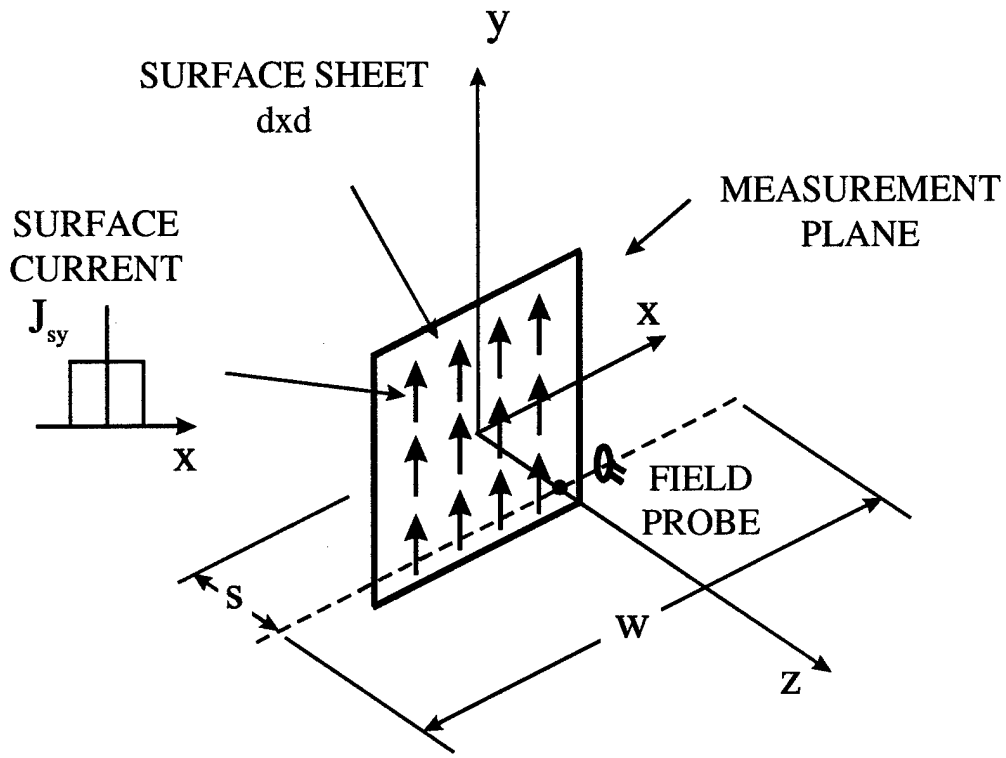

Figure 2-3 Three-dimensional geometry for back-propagation study.

3 Two-Dimensional Current Distribution Study.

The various parameters such as measurement window size, distance to the measurement plane, amount of spectral content required to reconstruct the current and others are studied using the two-dimensional current distribution and geometry described in section 2 and shown in Figure 2-1. The characteristics of the surface current employed to determine the effectiveness of the technique are the general pulse shape and sharpness of the pulse edges. In section 3.1, the effect of the distance, s, from the object to the measurement line and signal to noise ratio (SNR) on the current pulse characteristics are studied. In sections 3.2 and 3.3 two measurement characteristics related to the probe are studied: the sampling rate due to the measurement probe spacing and field averaging due to the finite probe size. In section 3.4 the resolution of small feature size is analyzed using a current pulse containing a small notch. The last section, 3.5, compares the advantages/disadvantages of measuring the electric field as opposed to the magnetic field with finite sized measurement windows.

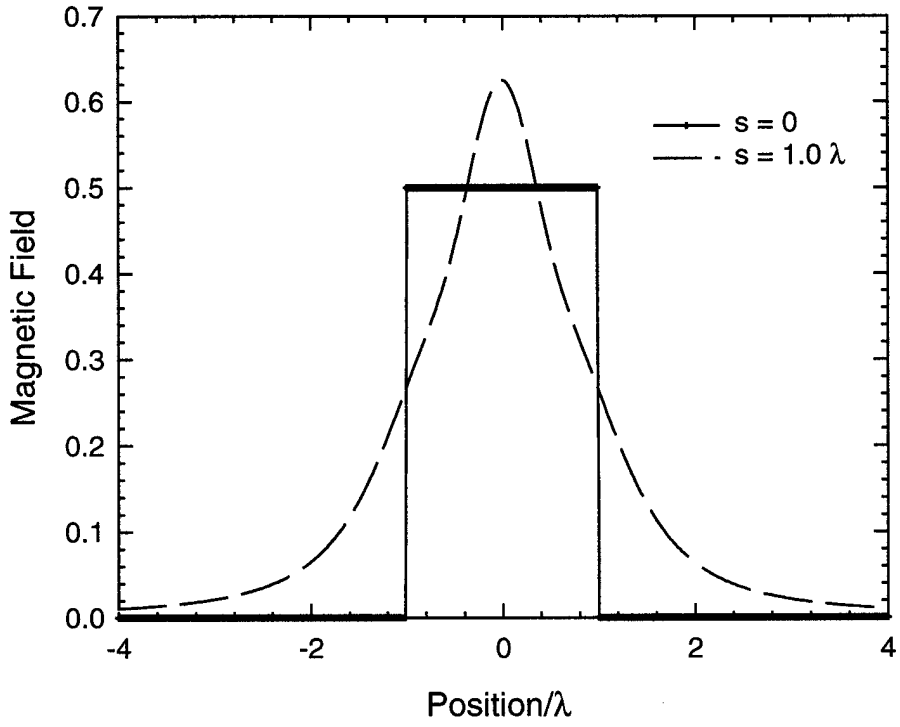

Figure 3-1 Magnetic field at the source and the measurement line. ($d = 2\ \lambda$, $SNR = 80$ dB)

3.1 Effect of Measurement Distance and SNR on Surface Current Reconstruction

The effect of the distance, s, and SNR on the reconstruction of the current pulse are studied in this section using the criteria of spectral bandwidth and pulse sharpness. The spectral bandwidth is defined as the spectrum within a distance of k_{cut} from the origin, since the spectral filter roll off starts near this value, at αk_{cut}. The sharpness of the pulse is called the *Rise* or *R* which is the 10% to 90% rise with respect to the pulse edges. In this section, first, the magnetic field plots at key steps in a typical forward and back-propagation calculation will be shown, and then the graphs of the results will be given and discussed.

Note that the term *SNR* is the signal-to-noise ratio. In this report, a Gaussian noise distribution is used to approximate spatial measurement noise. Consider a complex Gaussian noise distribution,

$$Z(x) = G_{re}(x) + jG_{im}(x) \tag{3.1}$$

where Z(x) is the complex noise and G is the real (subscript *re*) or imaginary (subscript *im*) Gaussian distribution. The mean of G is 0 and standard deviation is σ. The noisy measured field then is given by

$$H_x^m(x) = H_x(x) + Z(x) \tag{3.2}$$

Since the complex noise distribution is added directly to the magnetic (or electric field) at the measurement line (or plane in the three-dimensional case), the *SNR* is given by the equation,

$$SNR = \frac{\left|H_x^{(\max)}\right|}{\sigma} dB \tag{3.3}$$

A typical forward and back-propagation simulation is shown in Figure 3-1 - Figure 3-3 for $s = 1\lambda$, $d = 2.0\lambda$ and *SNR* = 80 dB. The forward propagation algorithm computes the magnetic field at the measurement line as shown in Figure 3-1. In reality, -80 dB of noise is also added to this signal but this level of noise is too small to be noticed in the spatial domain. The figure also shows the magnetic field distribution at $z = 0^+$. The figure indicates that the field distribution broadens in x the further it is from the source.

Before back-propagating the fields, the spectrum is obtained with the FFT as shown in Figure 3-2. This figure compares the magnetic field spectrum without noise (labeled 'Spectrum') to the spectrum with noise (labeled 'With Noise') and the filtered spectrum (labeled 'Windowed') which was obtained by applying (2.12) to the noisy spectrum. The need for filtering the spectral domain signal can be seen in this figure. The spatial domain noise, which is not readily apparent in the spatial magnetic field distribution is obvious in the spectral domain because the magnetic field spectrum falls off rapidly with increasing magnitude of k_x. If this noise is not filtered out sufficiently, the back-propagator, (2.14), which amplifies the evanescent spectrum by approximately $e^{k_x s}$ for large k_x, can cause the noise floor to grow when it is back-propagated and wash out the signal. Therefore, the filter is applied to reduce the noise floor below that of the actual magnetic field spectrum.

Any filter will function provided the result after filtering is at or below the actual spectrum of the field. The filter in this report was previously discussed in section 2.2. For this case, $k_{cut}/k_0 \approx 1.25$ and $\alpha = 0.8$. The variable, α, is typically chosen to be 0.8 or 0.7 in all of the two-dimensional examples to avoid excessive damping of the desired evanescent spectrum which would reduce the sharpness or rise of the reconstructed current distribution.

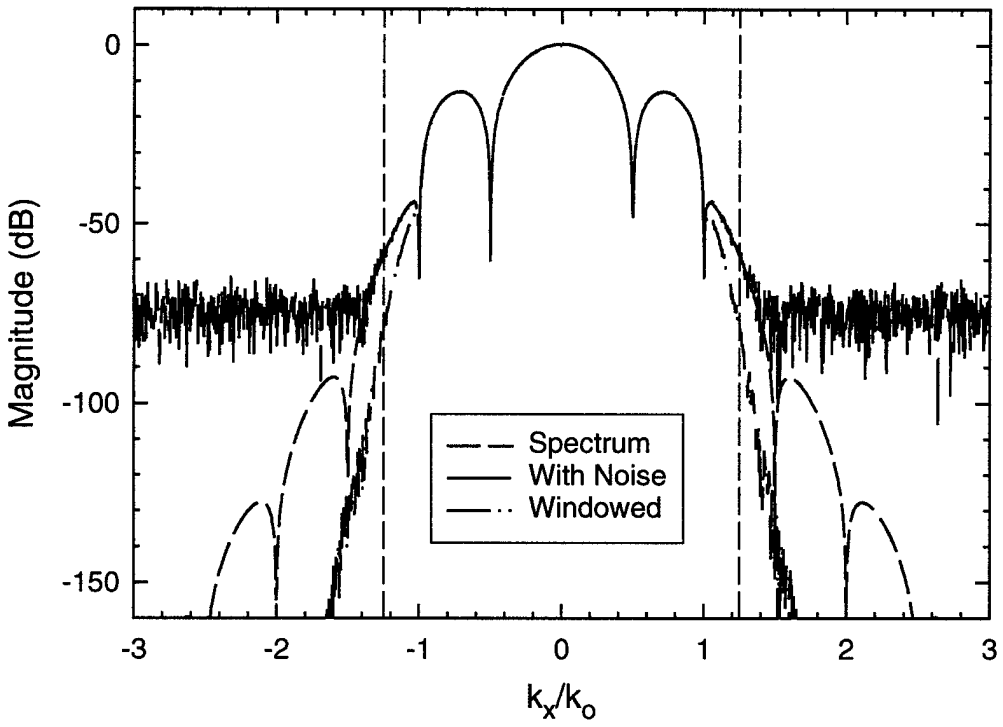

Figure 3-2 **Spectrum of spatial magnetic field at the measurement plane. ($d = 2\ \lambda$, SNR = 80 dB)**

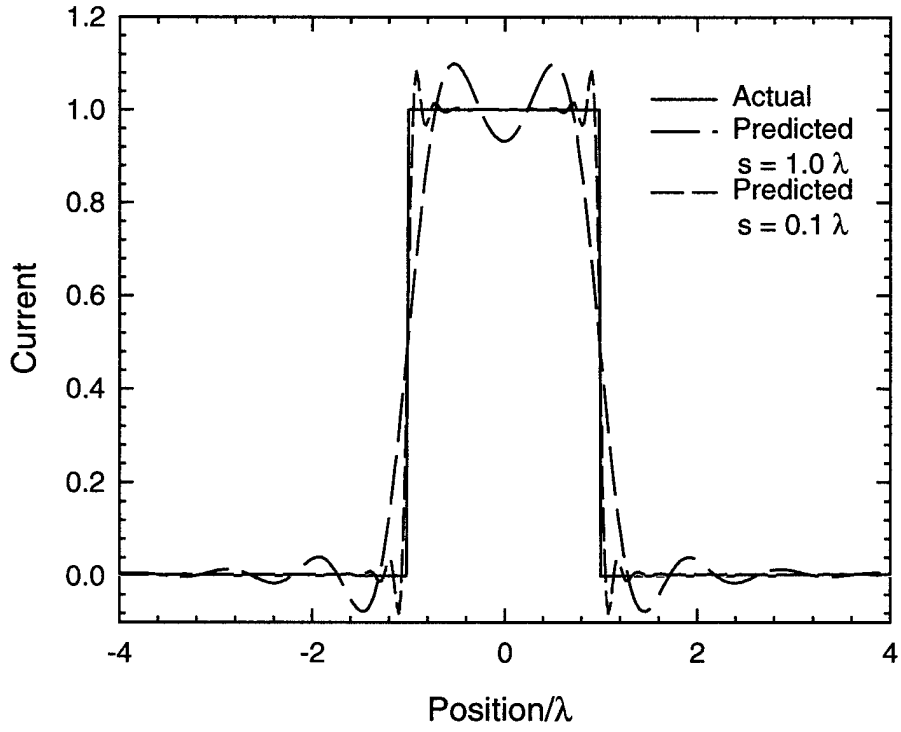

Figure 3-3 **Reconstruction of current from back-propagation for $d = 2\ \lambda$, $s = 1.0\ \lambda$ and $s = 0.1\ \lambda$.**

After back-propagating the fields and taking the inverse Fourier transform, the current distribution is obtained and is shown in Figure 3-3. In this figure, two cases for $s = 0.1\ \lambda$ and $1.0\ \lambda$ are shown and compared with the actual current distribution. The *rise* or R is given by $R = 0.42\ \lambda$ for $s = 1.0\ \lambda$ and $R = 0.08\ \lambda$ for $s = 0.1\ \lambda$.

The first results of the back-propagation study concern the relationship between the spectral content determined by k_{cut} and the SNR for various distances, s, of the measurement line to the surface current. The results of this analysis are shown in Figure 3-4. These data were processed to remove the ripples caused by the 'lobes' in the Sinc-type shape of the magnetic field spectrum. The processing involved averaging k_{cut} over $2 < d < 10$. This is done since k_{cut} approaches a relatively constant value with increasing d. The results in Figure 3-4 indicate the value of k_{cut} is proportional to the SNR and inversely proportional to s.

The inverse proportionality of k_{cut} to s is related to the fact the field distribution becomes wider in space as the measurement line moves further from the surface current. The wider field distribution has a narrower spectrum, and consequently, the amount of spectrum above the noise floor will be less.

The direct proportionality of k_{cut} to the SNR can be seen from the relation of k_{cut} and the SNR to the noise floor level. As the SNR increases, the noise floor relative to the magnitude of the field decreases, and a wider spectrum is available, which leads to a larger value of k_{cut}.

A similar study was performed to relate the signal sharpness or *Rise* to SNR, and the results are shown in Figure 3-5. Comparing Figure 3-4 and Figure 3-5 one can see the *Rise* is inversely proportional to k_{cut}. This demonstrates the known fact that sharp edges that require a low value for R require a broad spectrum or a large value for k_{cut}.

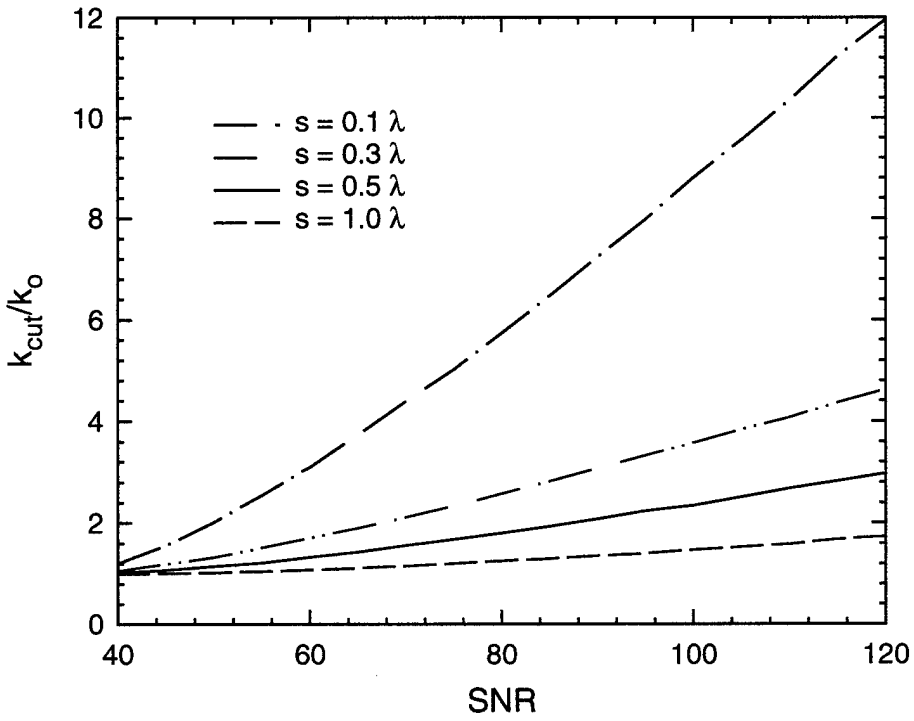

Figure 3-4 The variation of k_{cut} with *SNR* for several distances, *s*, of the measurement plane from the source plane.

This analysis shows that s and SNR determine sharpness of features. In addition, by invoking the Nyquist criterion, the minimum number of samples per wavelength required for reconstructing a current distribution with a particular sharpness or rise can be approximated. The Nyquist criterion states that to accurately compute the spectral frequency up to k_{cut}, the sampling rate must be at least twice k_{cut} which turns out to be a sampling interval of 0.5 λ_c, the cutoff wavelength corresponding to k_{cut}. Assuming $Rise$ is no better than approximately 0.5 λ_c,

$$N \approx \frac{\lambda_c}{Rise} \tag{3.5}$$

where N is the number of samples per wavelength at the Nyquist rate. To conclude this section, since the $Rise$ and k_{cut} values are both related to the cut off wavelength, λ_c, their product is approximately constant as shown in Figure 3-6 for different SNR and s values.

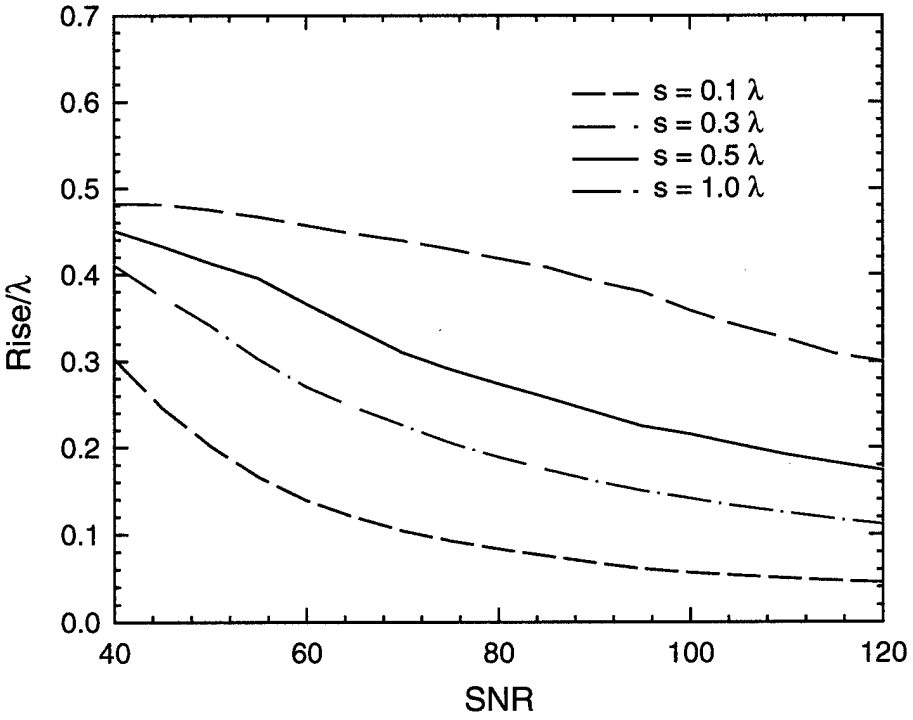

Figure 3-5 ***Rise/λ* vs *SNR* for different *s*.**

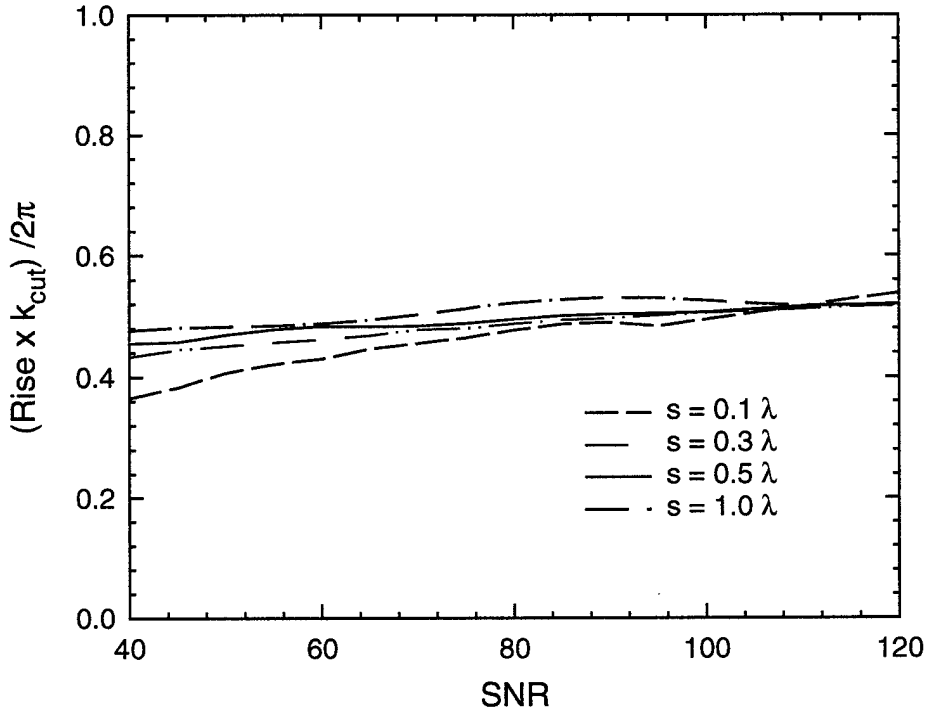

Figure 3-6 ***Rise*k*$_{cut}$ vs *SNR* for (2 < *d*)**

3.2 Effects of Undersampling on Surface Current Reconstruction

In this section the effect of aliasing caused by undersampling, or sampling at a rate slower than the Nyquist, criterion is shown. Aliasing can occur because the DFT, which is a periodic transform, is used to approximate the continuous Fourier transform of an aperiodic signal, i.e., the current pulse or the magnetic or electric fields. If the sampling rate is too low or, equivalently, the samples are too far apart in the spatial domain, the periodic repetitions of the spectra will be too close together in the spectral domain causing unwanted interference or aliasing. If the aliasing is severe enough, it can lead to distortions in the original signal when the aliased plane wave spectrum is employed in the back-propagation method.

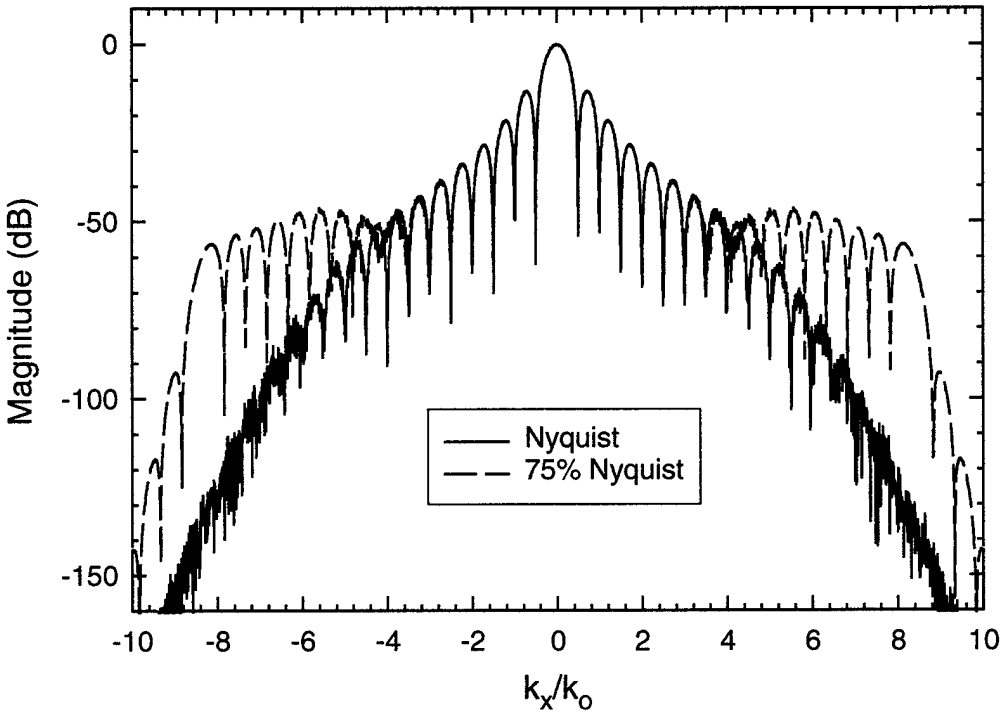

Figure 3-7 Aliasing due to undersampling. The k_{cut} value $k_{cut}/k_0 = 5.7$ is at the dashed lines. ($d = 2\ \lambda$, $s = 0.1\ \lambda$, $SNR = 80$ dB)

Figure 3-7 shows aliasing in the spectrum resulting from sampling at 75% of the Nyquist rate determined by the k_{cut} value. The solid line result was sampled at the Nyquist rate and shows no significant aliasing while the dashed line result was sampled at 75% of the Nyquist rate, and the aliasing is readily apparent. If a moderate amount of aliasing is present, and the sampling rate can not be increased, a filter, e.g. (2.12) can be employed to filter out the more severely aliased part of the spectrum by truncating the spectrum appropriately.

The effect of aliasing on the reconstruction of the current pulse can be seen in Figure 3-8 when a filter given by (2.12) with

$$\gamma = \sqrt{1-\alpha}\sqrt{\frac{k_{cut}}{s}} \tag{3.6}$$

is employed. The filter with γ given by (2.13) was not employed because it damps out the aliasing effect so that the aliasing does not stand out as dramatically. This figure demonstrates that aliasing, improperly handled, can severely distort the reconstructed current. However, by sampling at the Nyquist rate or above, aliasing of spectral components below k_{cut} is avoided.

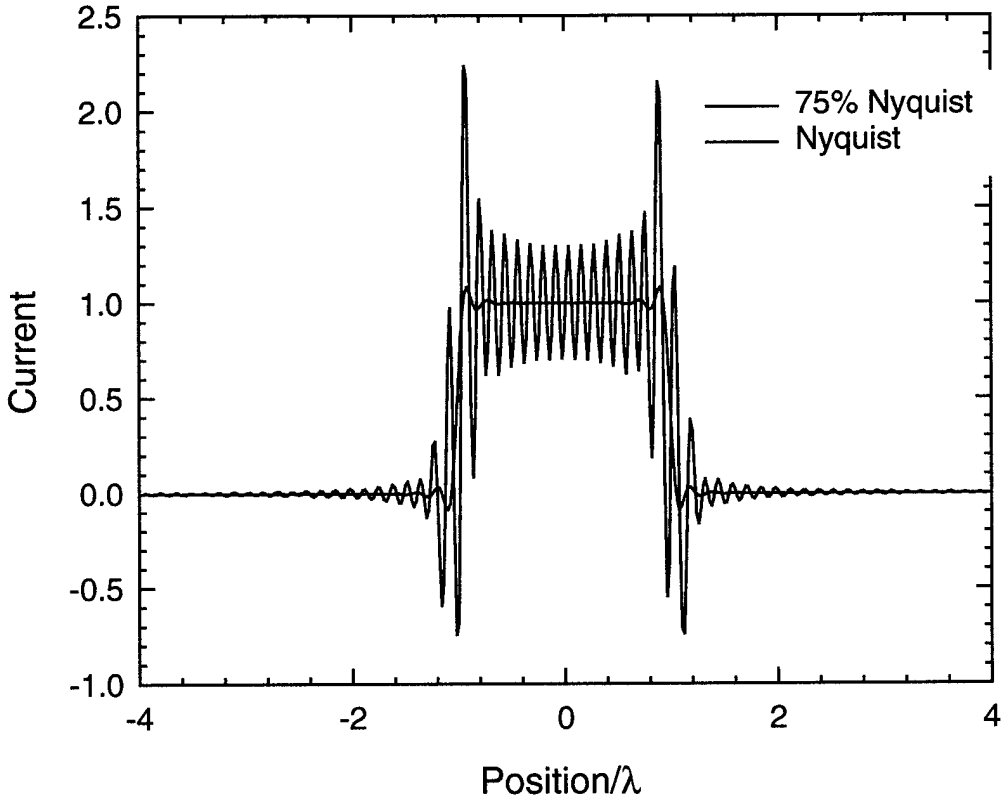

Figure 3-8 Reconstruction of current from back-propagation of aliased spectrum shown in Fig. 11. (d= 2 λ, s = 0.1 λ, SNR = 80 dB)

3.3 Effect of Probe Averaging on Surface Current Reconstruction

Another measurement parameter besides sample spacing is the effect of the probe size on the measurements. Since the probe has a finite size, it measures the fields over a region of space instead of at a point. An approximate means of simulating this 'probe averaging' is to locally average the

fields around each measurement point at the measurement line. In this study, it is assumed that the probe can measure at least one-half of λ_c. Hence, the fields at each point on the measurement line are averaged over a distance of 0.5 λ_c. The effect of this averaging process on the surface current reconstruction is shown in Figure 3-9. The probe averaging reduces the sharp features, and R/λ is reduced from 0.09 to 0.4.

3.4 Resolving Small Features in a Surface Current Distribution

This analysis studies the effectiveness of the back-propagation algorithm at modeling small features of the current distribution. The criterion of the study is the accuracy of reproducing a notch in the current distribution for different *SNR*'s and different distances from the current surface. First a sample simulation will be shown and then the graph of the results will be given and discussed.

Several plots of the magnetic field taken at different steps during a typical back-propagation procedure are shown in Figure 3-10 – Figure 3-12. Figure 3-10 shows the magnetic field distribution at the source plane and the measurement plane 0.1 λ away for $d = 2.1\ \lambda$ and $SNR = 80$ dB. The notch is reproduced in the magnetic field at the measurement line, but it is much smaller and less sharp. Figure 3-11 shows the spectrum of the magnetic field at the measurement line, the spectrum with noise added, and the filtered spectrum. For this case, $k_{cut}/k_0 = 8.28$ and $\alpha = 0.8$. The reconstructed current distribution is shown in Figure 3-12 and compared with the original current. For this set of parameters, the current reconstruction matched the original current with the notch in general with oscillatory components resulting mainly from the finite spectrum and filtering that was employed in the back-propagation.

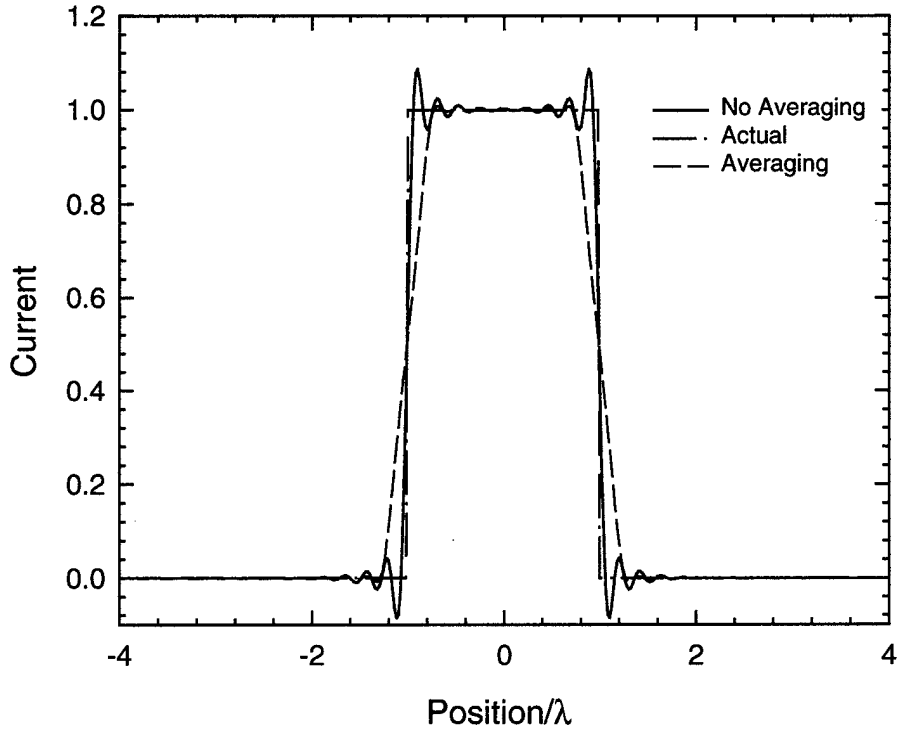

Figure 3-9 Current reconstruction with and without probe averaging. (d= 2 λ, s = 0.1 λ, SNR = 80 dB)

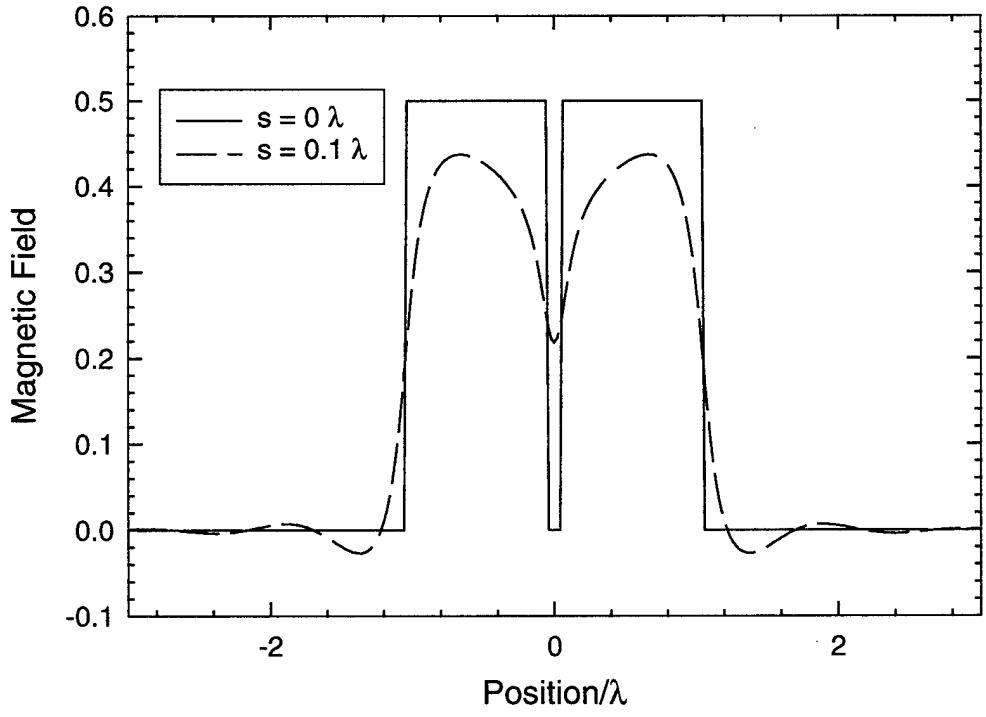

Figure 3-10 Magnetic field at the source and s = 0.1 λ of double pulse current distribution. (d = 2.1 λ with a 0.1 λ gap, SNR = 80 dB)

The final results of the analysis are shown in Figure 3-13. Here the resolving power or ability to reconstruct the small, sharp details in the current is defined as the null height. These results show that the null height approaches zero in an oscillatory fashion as the *SNR* increases. Also, the resolving power is greater when the measurement line is closer to the surface current for the given *SNR*. Even though the null height does not converge uniformly to zero, this study indicates the general trend is that resolving power increases for the larger *SNR* and smaller distances, s, which is in agreement with the analyses in preceding sections.

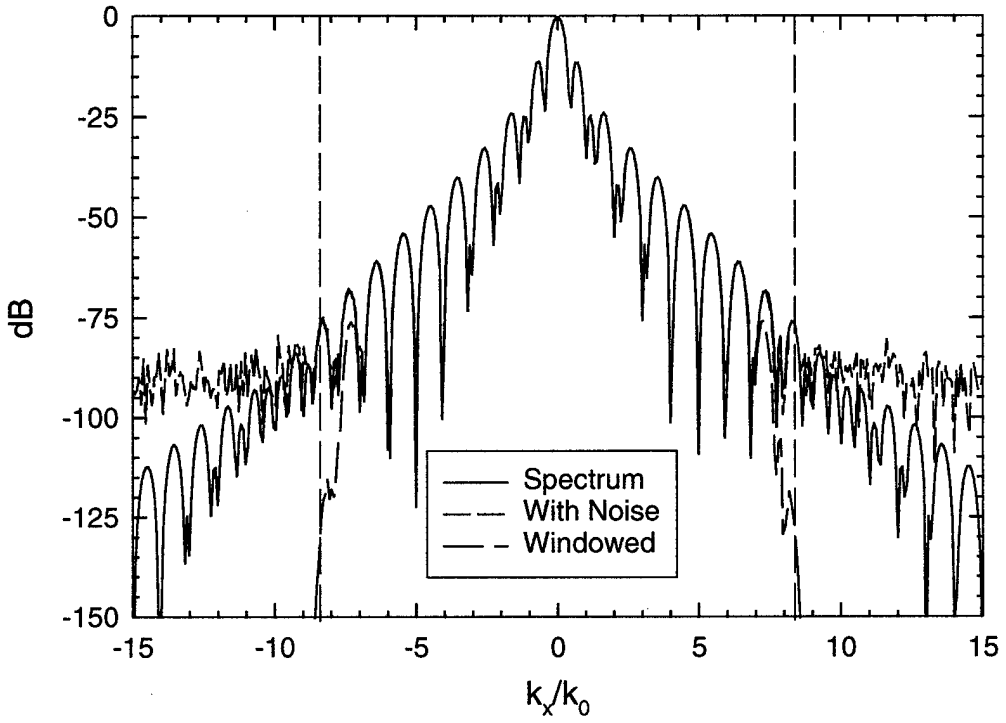

Figure 3-11 Spectra of magnetic field at the measurement plane. ($d = 2.1\ \lambda$ with a $0.1\ \lambda$ gap, *SNR* = 80 dB)

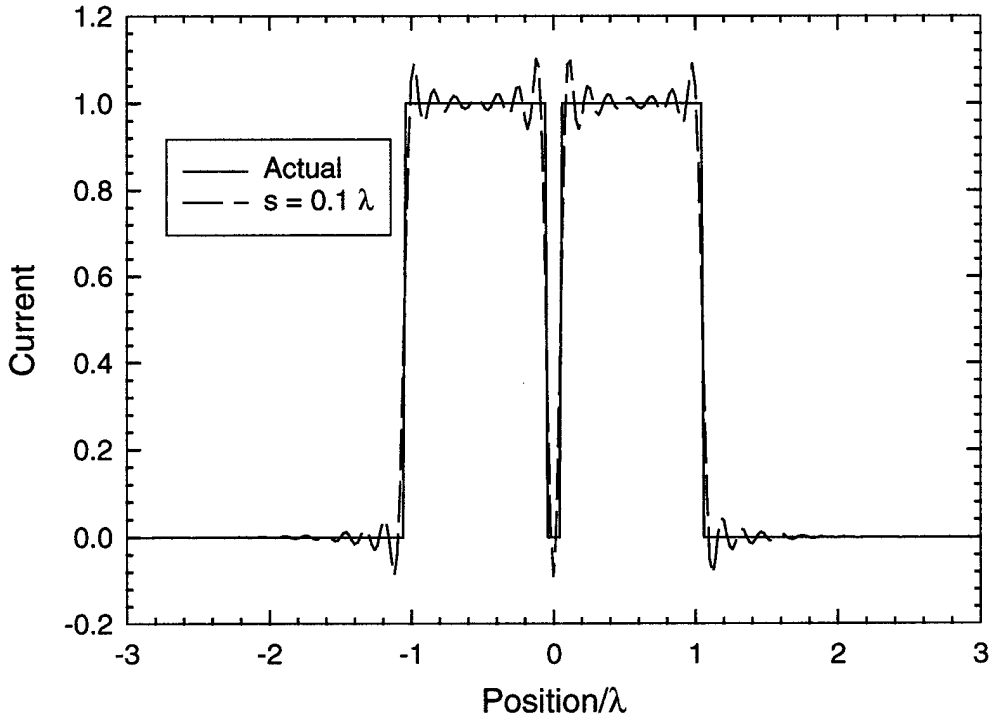

Figure 3-12 Reconstructed current distribution from filtered spectrum shown in Figure 3-11. (d = 2.1 λ with a 0.1 λ gap, SNR = 80 dB)

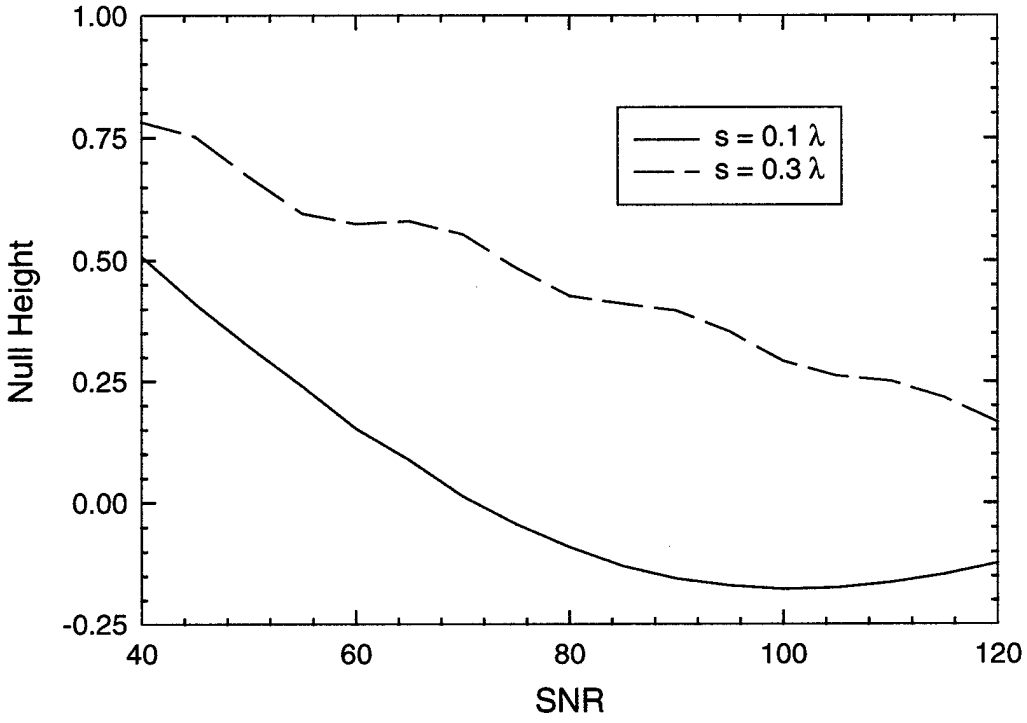

Figure 3-13 Null height vs *SNR* for s = 0.1 λ and 0.3 λ. (d = 2.1 λ with a 0.1 λ gap, *SNR* = 80 dB)

3.5 Use of Electric Field Simulations with Finite Measurement Window Size for Surface Current Reconstruction

The simulations so far have used the magnetic field at the measurement line, but back-propagation can also be performed from a measurement of the electric field. In this section, the use of the electric field as opposed to the magnetic field for back-propagation will be investigated. This analysis will be done with a finite measurement window length, because as expected no difference is apparent when one or the other field is used with the infinite or very large window. Thus the effect of the finite measurement window on reconstruction of the current is also included in this study.

The difference in the electric and magnetic field distributions at the measurement plane can be seen in Figure 3-14 for a distance of s=0.1 λ. Since the electric field decays more slowly than the magnetic field, it will require a wider measurement window to provide the same amount of accuracy as with the magnetic field. Providing the measurement window, shown by W in the figure, is large enough, either field quantity can be used for the reconstruction of the current. However, since the actual measurement window is of finite size, it becomes important which field is

employed. For this example, the window is set to $W = 3\ \lambda$. Both fields were back-propagated, and the resulting current distributions are shown in Figure 3-15 and Figure 3-16.

The effect of the window is evident in the oscillations or peaks at $\pm$ 1.5 λ. In both figures, the results with the measurement window are compared to results computed with an infinite window. The 'infinite window' was actually finite but very large. No noticeable difference is seen in the current distribution of the finite and 'infinite' windows for the magnetic field case except near the window edges, but differences are noticed in the electric field case, and the effect of the window edges are more pronounced.

This study indicates the magnetic field is better to employ because its narrower spatial distribution in comparison with the electric field will require a smaller measurement window than that required by the electric field. In addition, the electric field close to the conductor where the current distribution resides is very small (it is zero on the conductor), and it may be more difficult to measure than the magnetic field which does not become zero on the conductor.

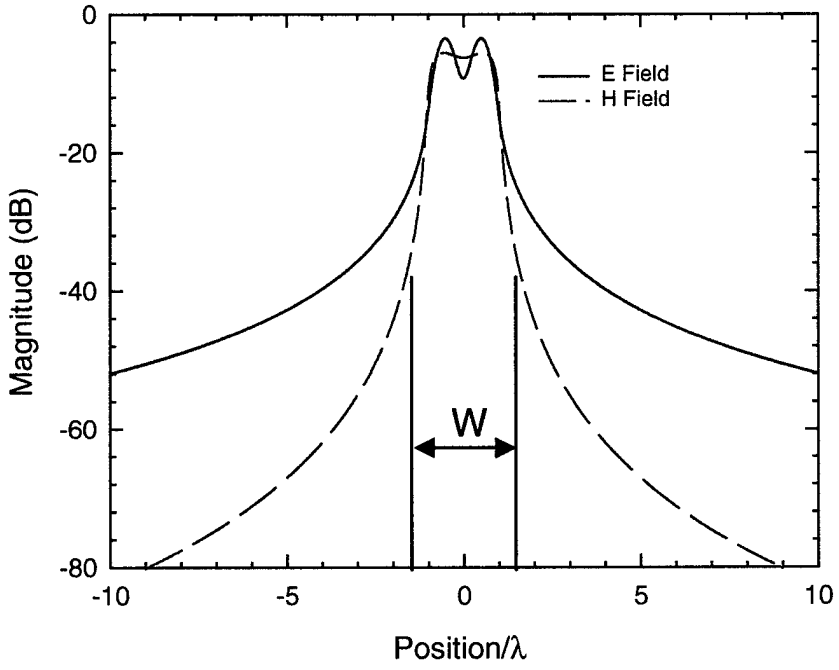

Figure 3-14 Comparison of electric and magnetic fields at the measurement plane. (s = 0.1 λ, d = 2 λ, SNR = 80 dB, W = 3 λ)

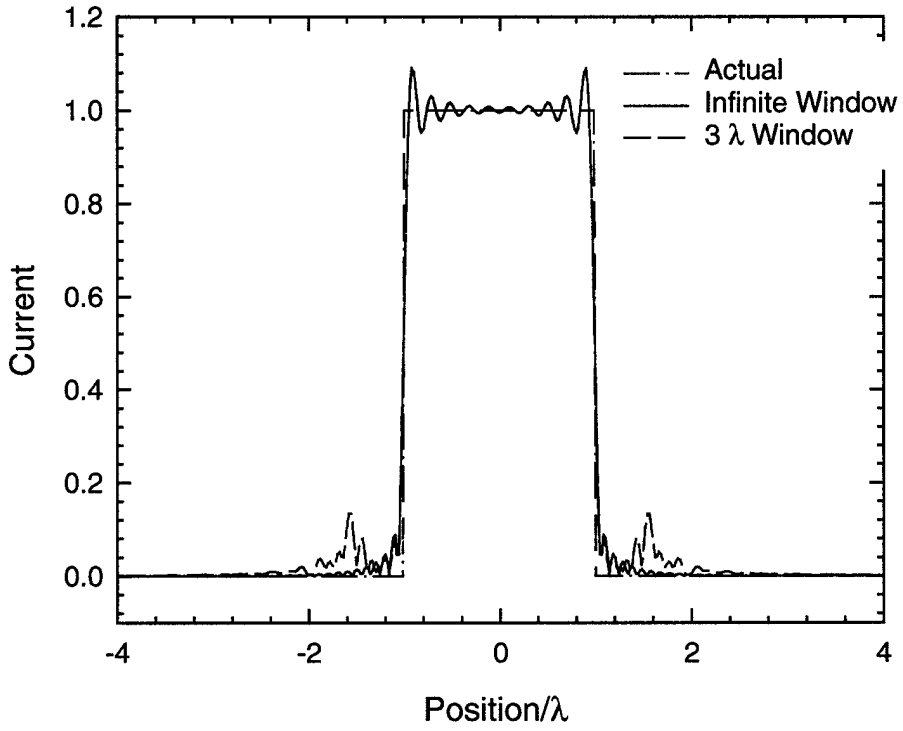

Figure 3-15 Current reconstructed from magnetic field distribution. 'Infinite window' refers to entire spectrum which was finite but very large.

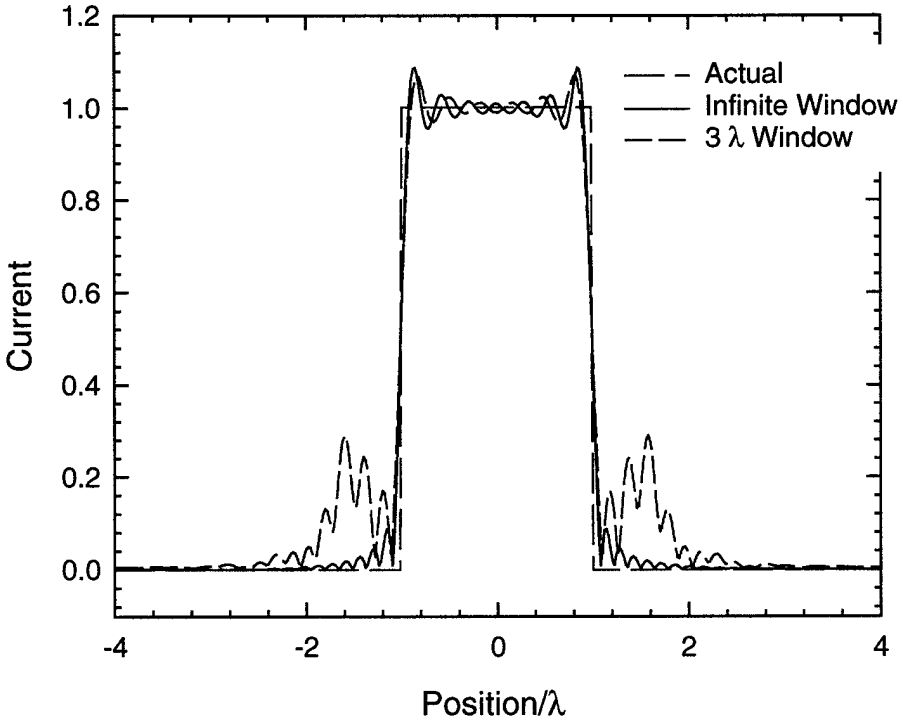

Figure 3-16 Current reconstructed from electric field distribution. 'Infinite window' refers to entire spectrum which was finite but very large.

4 Three-Dimensional Simulation of Back-Propagation

In this section the three-dimensional back-propagation method is demonstrated by reconstructing two-dimensional current distributions. The algorithm is discussed in section 2.3 and 2.4. The geometry under consideration is shown in Figure 4-1 where a two-dimensional pulse of surface current, J_{sy}, exists over a region of dimension d x d on the surface $z=0$. The measurement is now on a plane, and the equations are for three-dimensional fields. To summarize the procedure, first, the magnetic field, H_x, at the measurement plane is computed with the forward propagation algorithm from the J_{sy} current distribution. This field is processed, e.g., Gaussian noise may be added, and becomes the measured field over a rectangular surface at $z=s$. Then, the result is back-propagated, and the surface current is reconstructed.

Results from a typical case, without Gaussian noise, are shown in Figure 4-2 through Figure 4-4. Figure 4-2 shows an image of the spatial field distribution at the measurement plane, $s = 0.2\ \lambda$, looking down on the measurement surface. Figure 4-3 shows the reconstruction of the surface current from the evanescent and propagating spectrum of the magnetic field, and Figure 4-4 shows the reconstruction of the surface current from just the propagating spectra of the magnetic field. The parameter $k_{cut}/k_0 = 1.7$ instead of 1 for the results in Figure 4-4, but due to the spectral filter, (2.12), the spectrum is mostly the propagating portion because the evanescent waves which exist for $|k_{cut}|/k_0 > 1$ are rapidly reduced with the filter. These results show that the evanescent spectrum adds a substantial amount of information towards reconstruction of the current distribution.

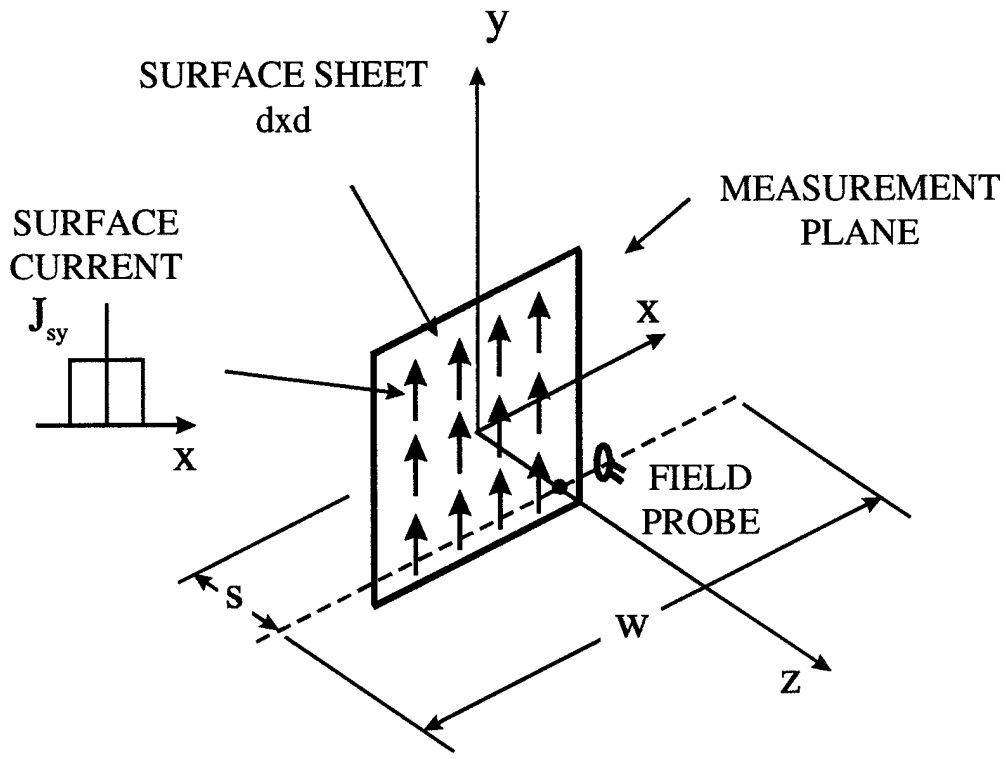

Figure 4-1 Three-dimensional simulation of measurement.

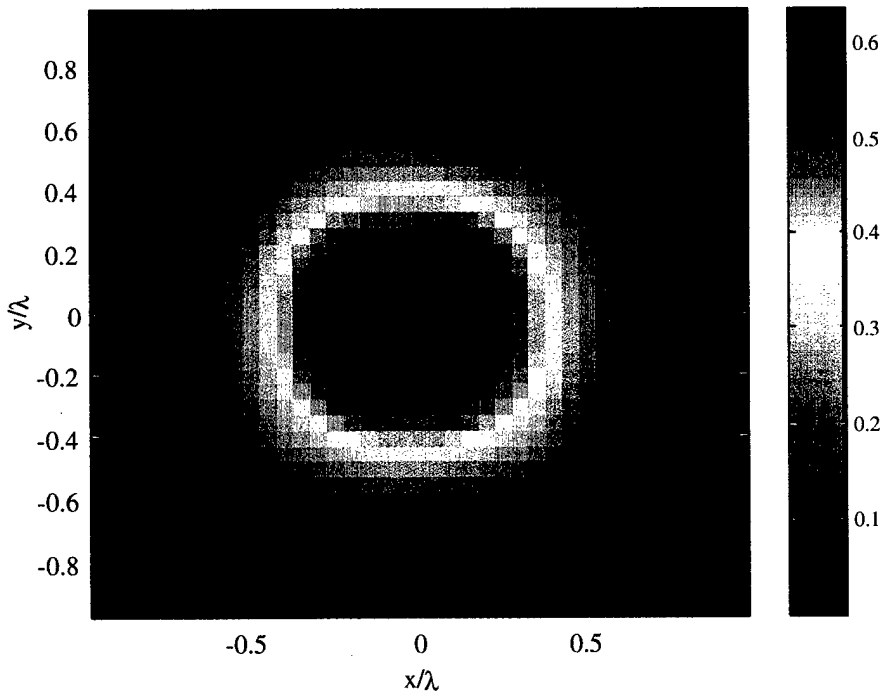

Figure 4-2 Image of magnetic field at the measurement surface. ($s = 0.2\ \lambda$, $d = 1\ \lambda$, current distribution is over a 1x1 λ surface, color bar is in A/m)

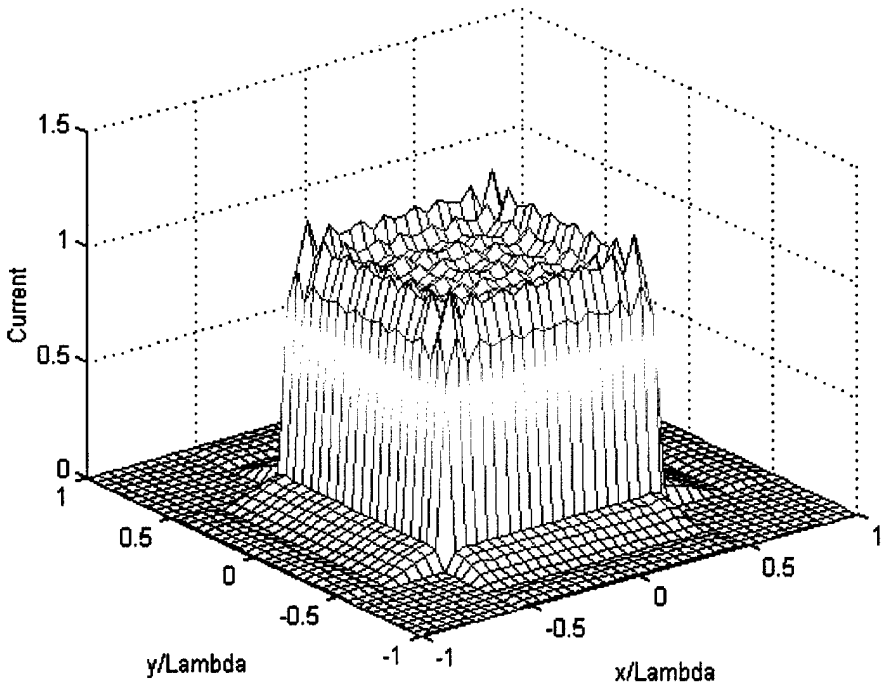

Figure 4-3 Reconstruction of current distribution from the evanescent and propagating spectrum of the measured magnetic field ($k_{cut}/k_0 = 10$).

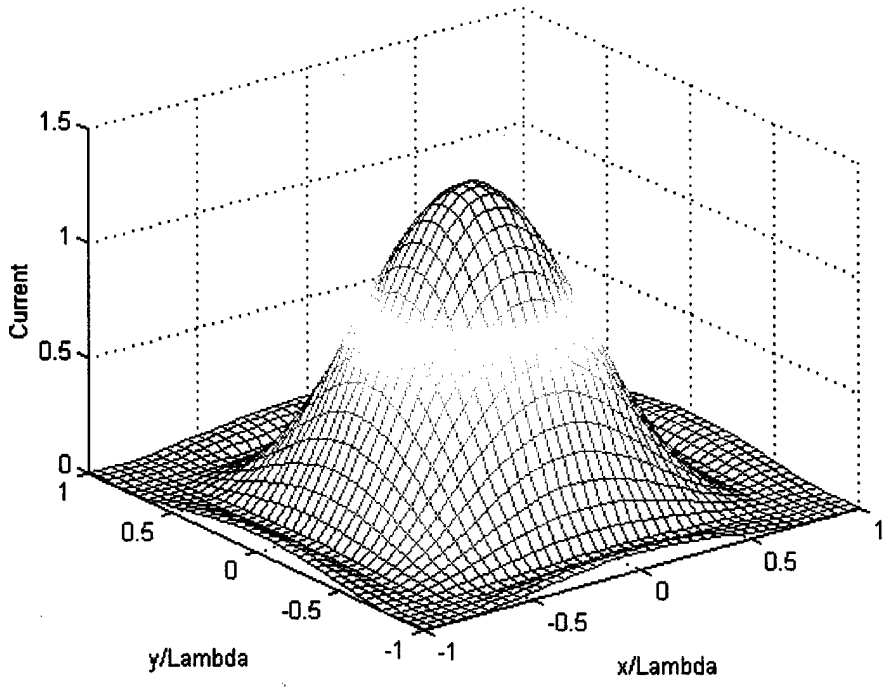

Figure 4-4 Reconstruction of current from the propagating spectrum of the measured magnetic field ($k_{cut}/k_0 = 1.17$).

The next example studies the reconstruction of a current distribution with sub-wavelength features, again without any Gaussian noise added at the measurement plane. An image of the measured field distribution at $s = 0.2\ \lambda$ is shown in Figure 4-5. Notice that no fine features are evident in the magnetic field at this distance. The reconstruction of the surface current from the measured fields is shown in Figure 4-6 and compared with the original current distribution in Figure 4-7. The fine features are readily visible, and the reconstructed current distribution is very close to the actual one.

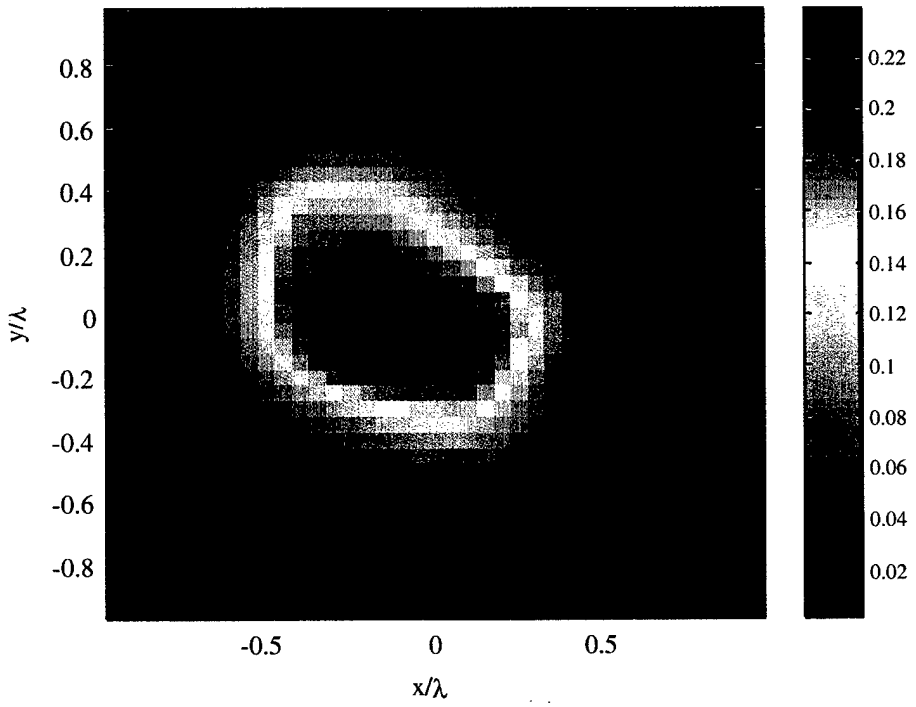

Figure 4-5. Image of magnetic field at measurement plane. ($s = 0.2\ \lambda$)

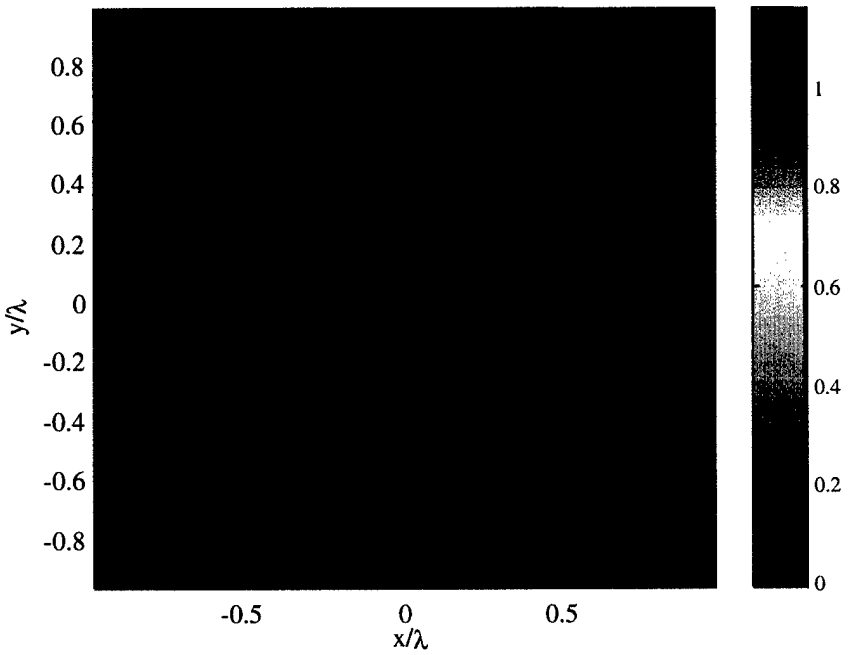

Figure 4-6. Reconstruction of surface current from measured magnetic field data.

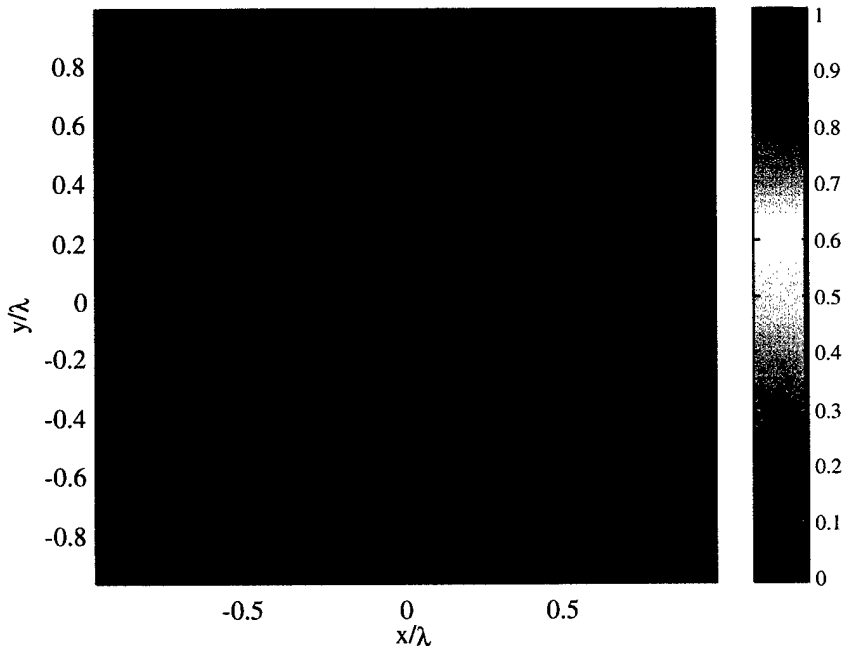

Figure 4-7. Original current distribution with sub-wavelength features.

5 FDTD Modeling of Measurement Configurations

Numerical simulations of the measurement configurations were performed using the finite-difference time-domain (FDTD) method. The simulations were used to evaluate the expected performance of the back-propagation technique for more realistic configurations. Potential measurement errors (noise and position error) were added to the simulations as well.

The basic measurement geometry is illustrated schematically in Figure 5-1. A horn antenna illuminates a metallic plate, shown with two slots, and a field probe samples the magnetic field on a plane in front of the plate. For the FDTD simulations, a somewhat simpler geometry was used to speed the calculations. This is shown in Figure 5-2 and Figure 5-3 for a square solid plate and a square slotted plate, respectively. A plane-wave, with E_y and H_x components, is normally incident on the 1 λ x 1 λ conducting plate, and the resultant scattered magnetic field is sampled at the measurement surface a distance of 0.2 λ from the plates. The sampled field at the measurement surface is tapered with a Hamming window to reduce the effects of measurement window truncation. The windowed, sampled field is transformed to obtain the plane wave spectrum, and then a spectral domain filter is applied to smoothly truncate the spectrum and remove any excessively noisy evanescent parts.

For these studies, the spectral domain filter variables k_{cut} and α can be more difficult to choose than in the two-dimensional cases, because there is no ideal spectrum with which to compare the noisy spectrum for determining k_{xcut} and k_{ycut}, and the spectral distributions are functions of two independent variables: k_x and k_y. The filter employed for the analyses in this section has three degrees of freedom: α, k_{xcut} and k_{ycut}. As with the two-dimensional results, the minimum signal acceptable was chosen to be the signal level that is four standard deviations above the mean noise floor. The signal levels at the periphery of the spectrum were taken to be the noise floor because the actual magnetic field spectrum is generally far below the noise floor at the limits of the spectrum. Once the noise floor was computed for the spectral signal along both the k_x and k_y axes, k_{xcut} and k_{ycut} were determined as the largest values of k_x and k_y for which the spectrum is four standard

deviations above the noise floor. The other variable, α, was set to 0.8 as for the two-dimensional case.

Three analyses are carried out for both plates using an *SNR* of 80 dB. The *SNR* was computed with respect to the peak value of each field component: H_x and H_y. The first analysis computes the back-propagated currents from measurements on an oversized 11 λ x 11 λ area on the measurement plane to provide a bench mark for the other studies which use smaller areas. The second study computes the back-propagated currents for a more realistic finite-sized measurement plane by truncating the scattered magnetic fields on the original measurement surface with a 2 λ x 2 λ Hamming window instead of a 11 λ x 11 λ Hamming window. The third study concerns the inaccuracies inherent in determining the probe location during the measurement process.

In all cases, the measurement or scan plane is 11 λ x 11 λ which contains 330 x 330 points at a sample spacing of 1/30 λ. To efficiently compute the FFT, zero padding is added to round the total number of points up to a power of 2 (512x512 points). For the second analysis, 512x512 points are still employed, but the magnetic fields at all points outside of the 2 λ x 2 λ Hamming window are zeroed.

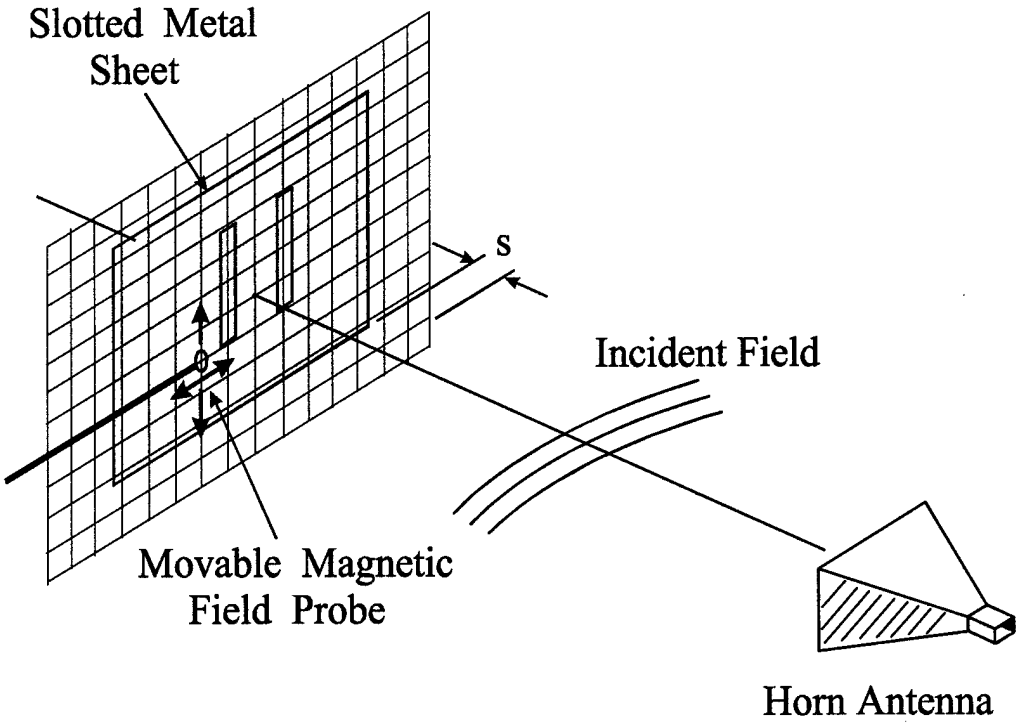

Figure 5-1 Measurement configuration.

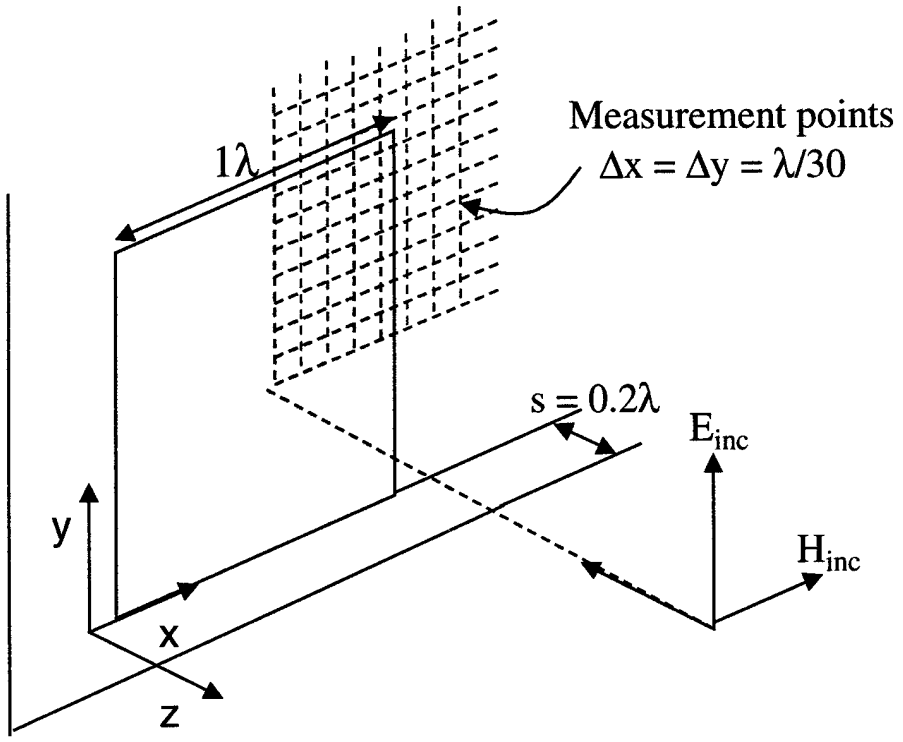

Figure 5-2 FDTD model for the measurement configuration for the flat plate. ($s = 0.2\ \lambda$, $d = 1.0\ \lambda$)

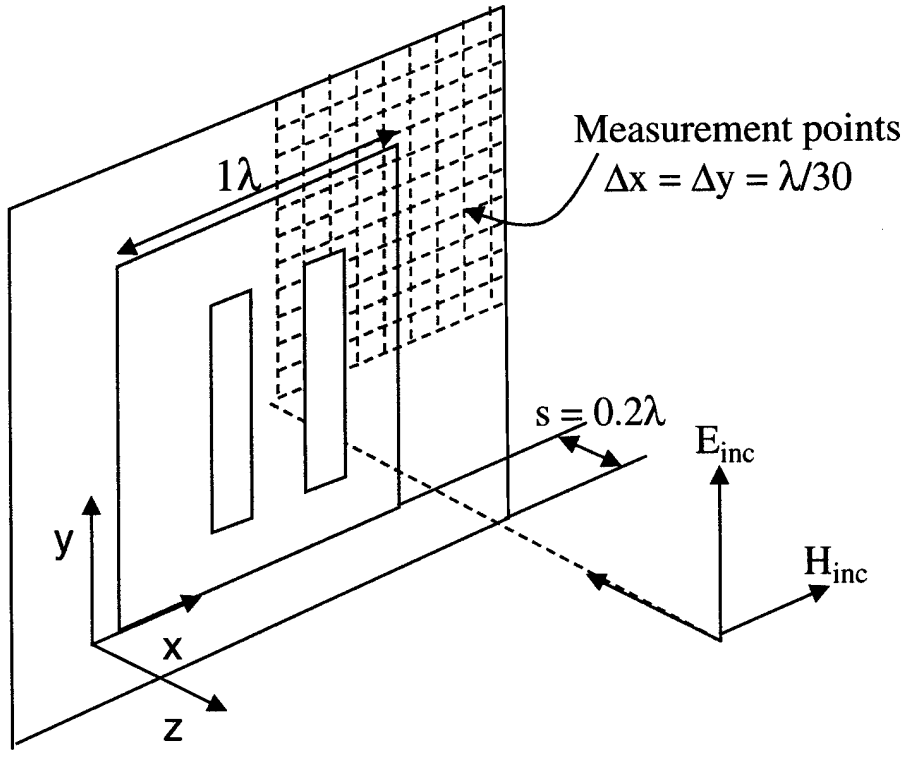

Figure 5-3 FDTD model for the measurement configuration for the slotted plate. ($s = 0.2\ \lambda$, $d = 1.0\ \lambda$)

For the third analysis, the locations of the magnetic field samples on the 11 λ x 11 λ measurement plane are randomized to study the effect of inaccuracies in measurement position on the surface current reconstruction. In actual measurements, the probe position can only be approximated, but the position error generally increases with distance along the scan or measurement plane instead of varying in a completely random fashion. The results presented here are based on a random choice of position that is more severe than encountered in the measurements. This approach is taken because it leads to a simple algorithm for randomizing the original scattered magnetic field data from the FDTD method.

The randomization procedure takes several steps. First, consider that the original scattered magnetic field data is located at spatial points that are 1/60 λ apart in a two-dimensional grid on the scan plane. Then, consider a second grid that is identical to the first except the field values are chosen from the first grid according to the probability distribution given in Figure 5-4. For each point in the new grid, the field value is chosen from among nine possible points clustered at the equivalent point in the original grid. For example, there is a 64% probability that the correct magnetic field value is used at each point. Once the locations are randomized over this plane, every other point is chosen to increase the spacing between samples from 60/λ to 30/λ (decrease the number of samples by a factor of four).

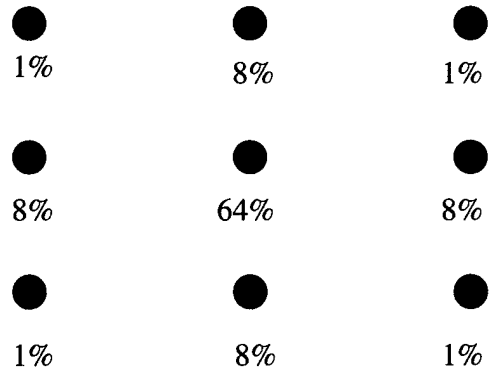

Figure 5-4 Probability for choosing the magnetic field value at a point surrounded by its neighbors. There is a 64% probability that the correct field value is employed, a 1% probability that the field value at a point located diagonally from the center is used and an 8% probability that the field value above, below or to either side is used for the field value at the central point.

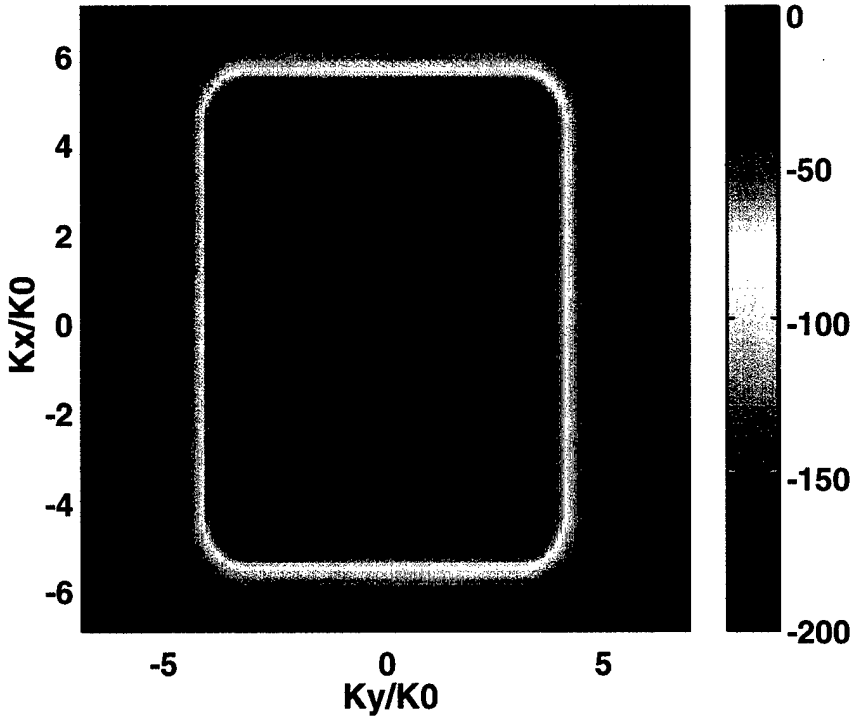

Figure 5-5 Spectral Filter for H_x shown in Figure 5-6. ($k_{xcut}/k_0 = 5.45$, $k_{ycut}/k_0 = 3.98$, $\alpha = 0.8$)

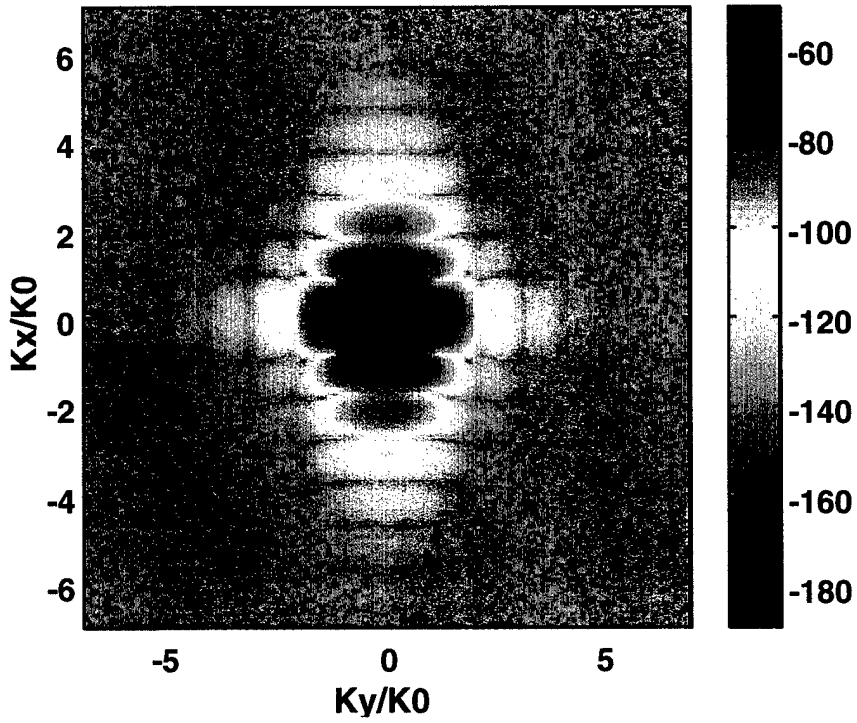

Figure 5-6 Image of Spectrum of H_x for square plate. ($s = 0.2\ \lambda$, $d = 1.0\ \lambda$, SNR=80 dB)

An example of the spectral filter is given in Figure 5-5 for the magnetic field spectrum shown in Figure 5-6. Note the filter is actually rectangular in shape since the spectrum upon which the k_{xcut} and k_{ycut} values are based has a diamond shape which fits better in a rectangular filter than a square filter. Also, the value for α is 0.8, which causes the edges of the filter to stand out since its magnitude rolls off quickly after αk_{xcut} and αk_{ycut}.

The k_{cut} values for all three analyses are given in Tables 1 and 2 for the square plate and plate with slots, respectively. The values are largest for the 11 λ x 11 λ measurement plane and decrease successively from the second analysis to the last or random position analysis.

Table 1. K_{cut} values for back-propagation for the square plate.

K_{cut} Values for H_x or J_y			K_{cut} Values for H_y or J_x		
Analysis	k_{xcut}/k_0	k_{ycut}/k_0	Analysis	k_{xcut}/k_0	k_{ycut}/k_0
11 λ x 11 λ	5.45	3.98	11 λ x 11 λ	3.52	4.69
2 λ x 2 λ	5.21	3.22	2 λ x 2 λ	2.52	3.05
Random Position	2.34	1.76	Random Position	1.46	1.11

Table 2. K_{cut} values for back-propagation for the square plate with slots.

K_{cut} Values for H_x or J_y			K_{cut} Values for H_y or J_x		
Analysis	k_{xcut}/k_0	k_{ycut}/k_0	Analysis	k_{xcut}/k_0	k_{ycut}/k_0
11 λ x 11 λ	6.27	3.98	11 λ x 11 λ	4.86	4.04
2 λ x 2 λ	5.27	3.28	2 λ x 2 λ	3.16	3.16
Random Position	2.75	1.82	Random Position	2.17	1.87

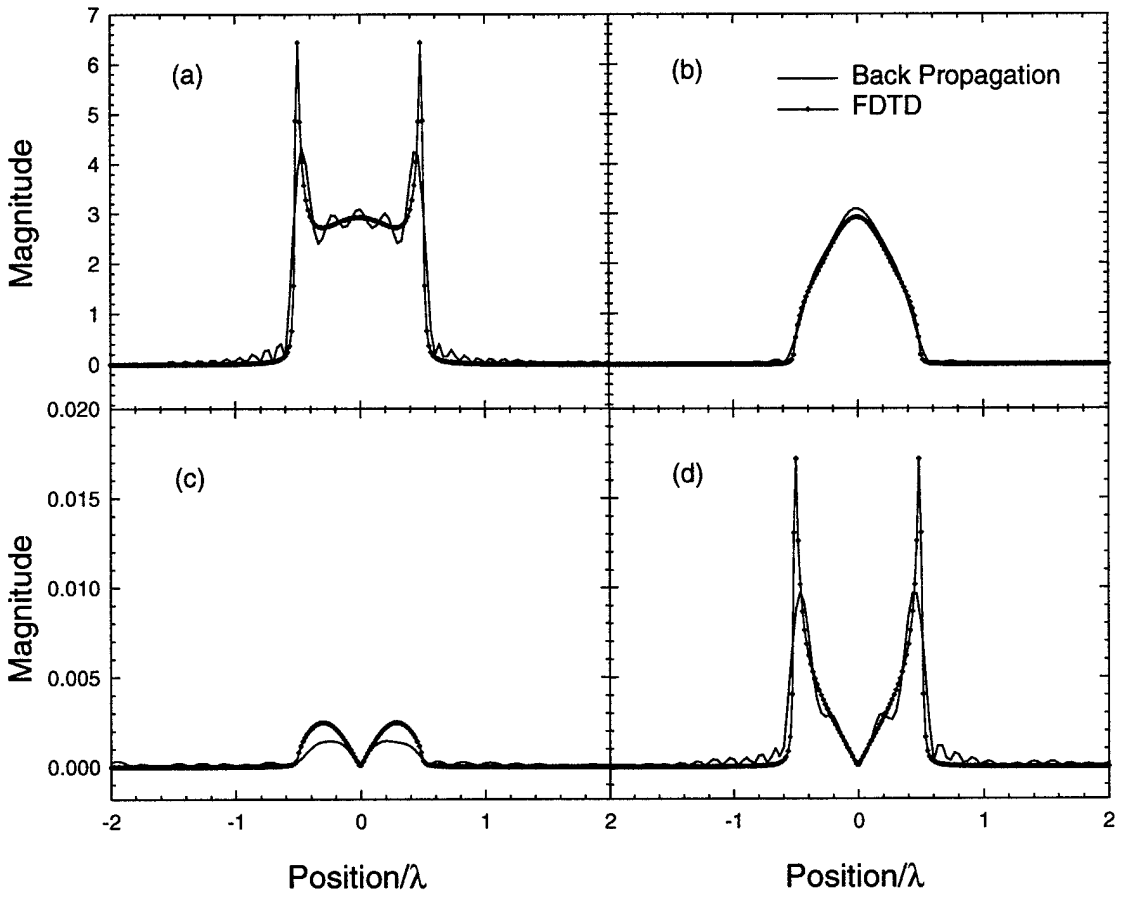

Figure 5-7 Normalized surface current computed with the back-propagation method using a 11 λ x 11 λ measurement window and the FDTD technique for a square solid plate. (s = 0.2 λ, d = 1 λ, SNR = 80 dB, 512x512 total points) (a) X- Cut for J_y/H_{inc} (b) Y-Cut for J_y/H_{inc} (c) X-Cut for J_x/H_{inc} (d) Y-Cut for J_x/H_{inc}

The results of the three analyses for the square plate are shown in Figure 5-7 - Figure 5-9. In each case s = 0.2 λ, d = 1 λ, and SNR = 80 dB. Both X and Y cuts of the J_x and J_y current distributions are shown normalized by the magnitude of the incident magnetic field. By X cut we mean a slice along the x axis through the center of the distribution, and similarly for Y cut. In the figures, the surface currents reconstructed with the back-propagation method are compared with the currents computed from the FDTD algorithm, which has been extensively verified for other problems. In addition, preliminary comparisons of the back-propagated currents were made with results in the technical literature which indicated the surface currents were reasonably accurate. Note that Table 1 gives the k_{cut} values for the three cases that will be presented next.

Figure 5-7 shows the results for the 11 λ X 11 λ measurement window with SNR =80 dB. The current distribution obtained with the back-propagation technique compares well with the current computed directly from the FDTD analysis in both shape and magnitude in general, except for the very sharp edges which require much more of the evanescent spectrum for reconstruction.

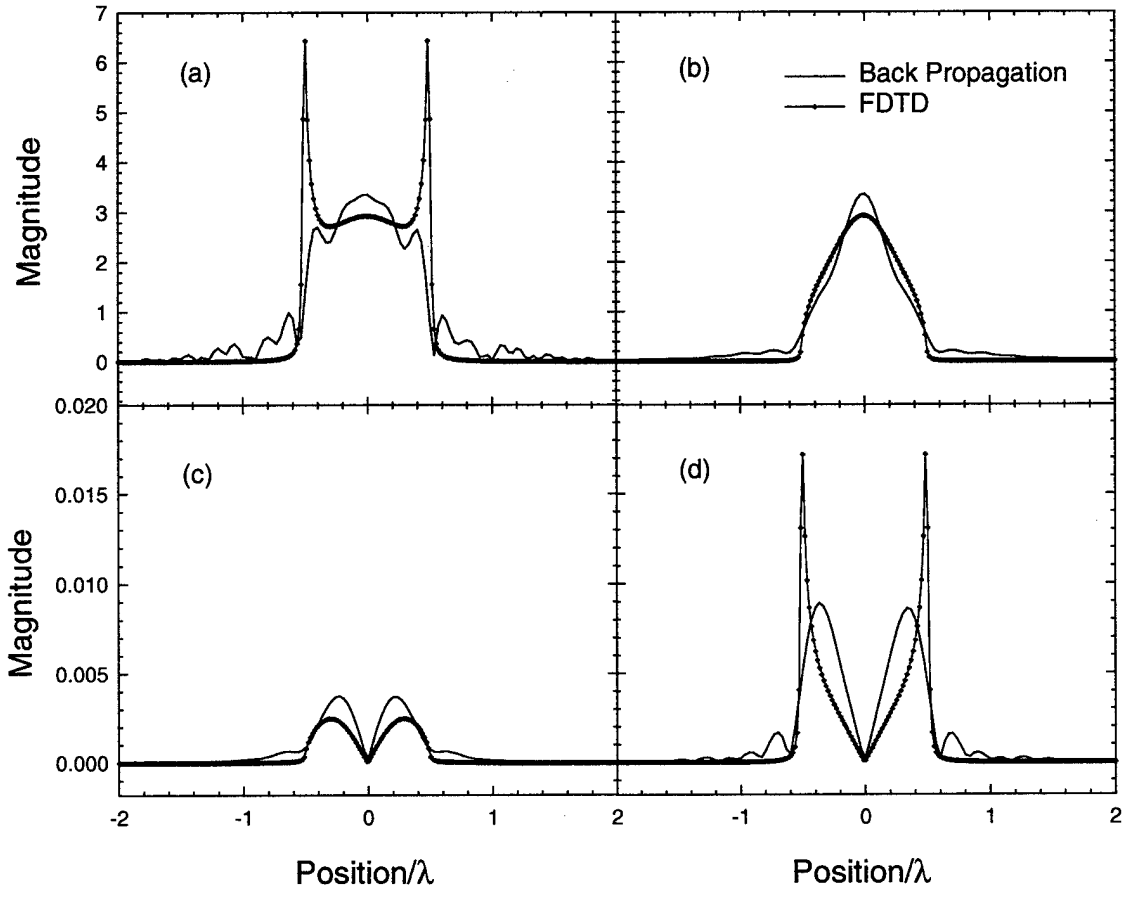

Figure 5-8 Normalized surface current, J/H_{inc} computed with the back-propagation method using a 2 λ x 2 λ measurement window and the FDTD technique for a square solid plate. (s = 0.2 λ, d = 1 λ, SNR = 80 dB, 512 total points) (a) X- Cut for J_y/H_{inc} (b) Y-Cut for J_y/H_{inc} (c) X-Cut for J_x/H_{inc} (d) Y-Cut for J_x/H_{inc}

The results for the truncated 2 λ x 2 λ measurement plane are shown in Figure 5-8. Comparing these results with those in Figure 5-7 shows the effects of truncation of the window: distortion of the shape of the current, and the introduction of artifacts near the edges of the window (± 1 λ). With the more realistic sized measurement window of 2 λ x 2 λ, the reconstructed current distribution is similar to that of the FDTD analysis except for the sharp peaks.

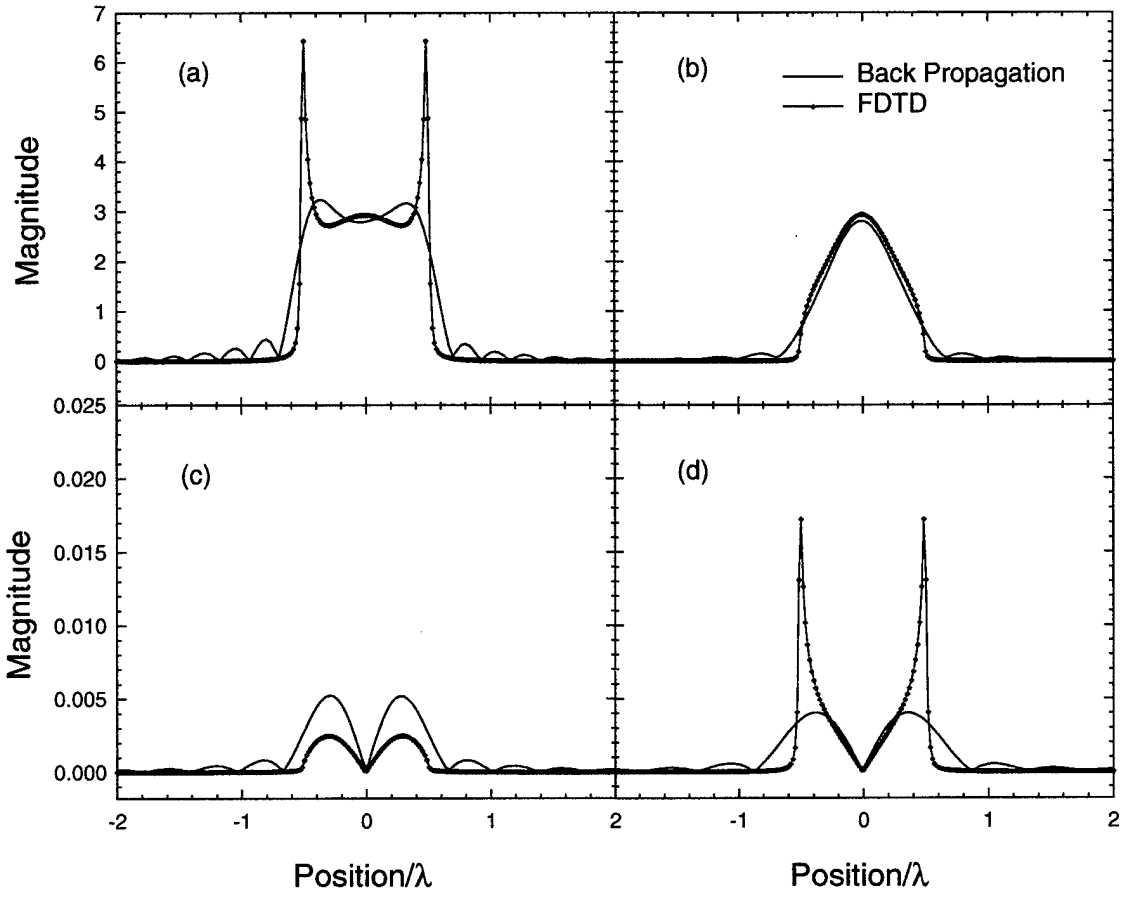

Figure 5-9 Normalized surface current computed with the back-propagation method using a 11 λ x 11 λ measurement window with a 64% probability of locating the measurement correctly and the FDTD technique for a square solid plate. ($s = 0.2\ \lambda$, $d = 1\ \lambda$, $SNR = 80$ dB, 512 total points) (a) X- Cut for J_y/H_{inc} (b) Y-Cut for J_y/H_{inc} (c) X- Cut for J_x/H_{inc} (d) Y-Cut for J_x/H_{inc}

In Figure 5-9 the surface current results from the back-propagation of the magnetic field at randomized locations is compared with the surface current results from the FDTD analysis. These results indicate the randomization smooths out the sharp peaks of the current waveforms.

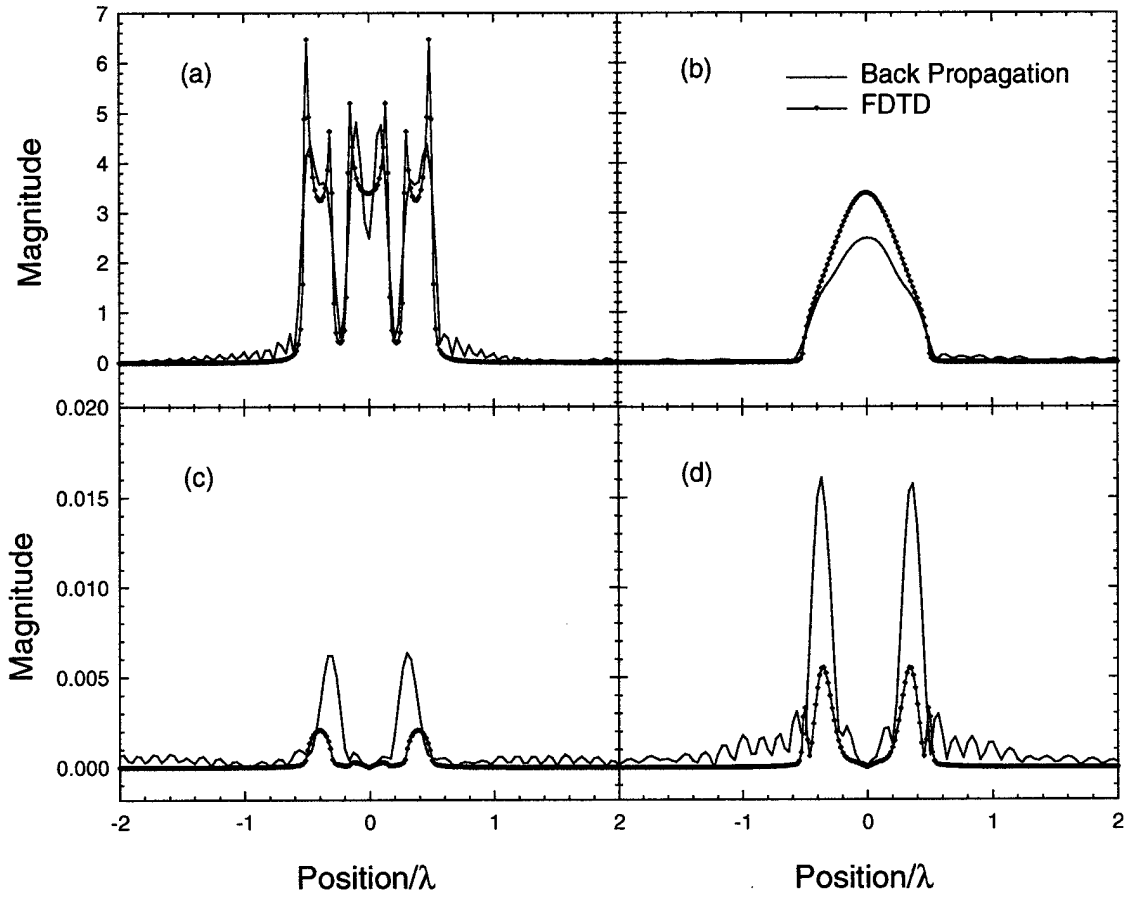

Figure 5-10 Normalized surface current computed with the back-propagation method using a 11 λ x 11 λ measurement window and the FDTD technique for a square slotted plate. (s = 0.2 λ, d = 1 λ, *SNR*=80 dB, 512 total points) (a) X- Cut for J_y/H_{inc} (b) Y-Cut for J_y/H_{inc} (c) X- Cut for J_x/H_{inc} (d) Y-Cut for J_x/H_{inc}

The results in Figure 5-10 through Figure 5-12 were obtained from the three analyses for the slotted plate shown in Figure 5-3. In each case s = 0.2 λ, d = 1 λ and *SNR* = 80 dB. Both X and Y cuts of the J_x and J_y current distributions are shown normalized by the magnitude of the incident magnetic field. In the figures, the currents obtained from the FDTD analysis are compared with the back-propagation currents. It is presumed that the currents obtained from the FDTD method are correct. The k_{cut} values are given in Table 2.

Figure 5-10 shows the surface current results for the 11 λ X 11 λ measurement window. The magnitude and shape of the surface currents reconstructed with the back-propagation method agree in general with the current obtained with the FDTD method. The largest difference occurs in the magnitude of the cross polarization term, J_x. The J_x surface currents are more difficult to

reconstruct probably because they are approximately 1000 times smaller than the main or J_y distribution.

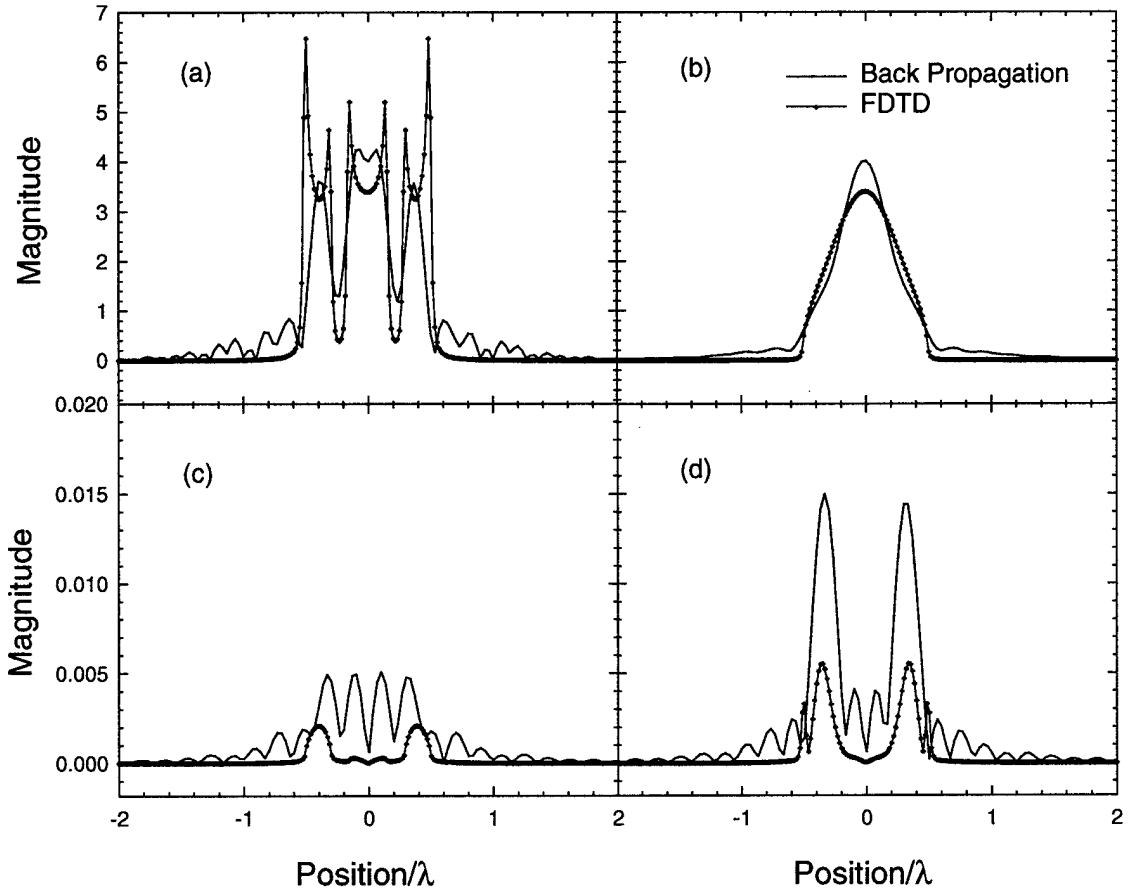

Figure 5-11 Normalized surface current, J/H_{inc} computed with the back-propagation method using a 2 λ x 2 λ measurement window and the FDTD technique for a square slotted plate. (s = 0.2 λ, d = 1 λ, *SNR*=80 dB, 512 total points) (a) X- Cut for J_y/H_{inc} (b) Y-Cut for J_y/H_{inc} (c) X- Cut for J_x/H_{inc} (d) Y-Cut for J_x/H_{inc}

The surface current results for the truncated 2 λ x 2 λ measurement plane are shown in Figure 5-11. Comparing these results with those in Figure 5-10 shows the window distorts the current shape, for example, the sharp edges shown in the FDTD result in Figure 5-11 (a) have been rounded off. In addition, the window leaves some artifact signals near the window edges of +- 1 λ. Again, the dominant current component, J_y, is more accurately reconstructed than the much smaller component, J_x.

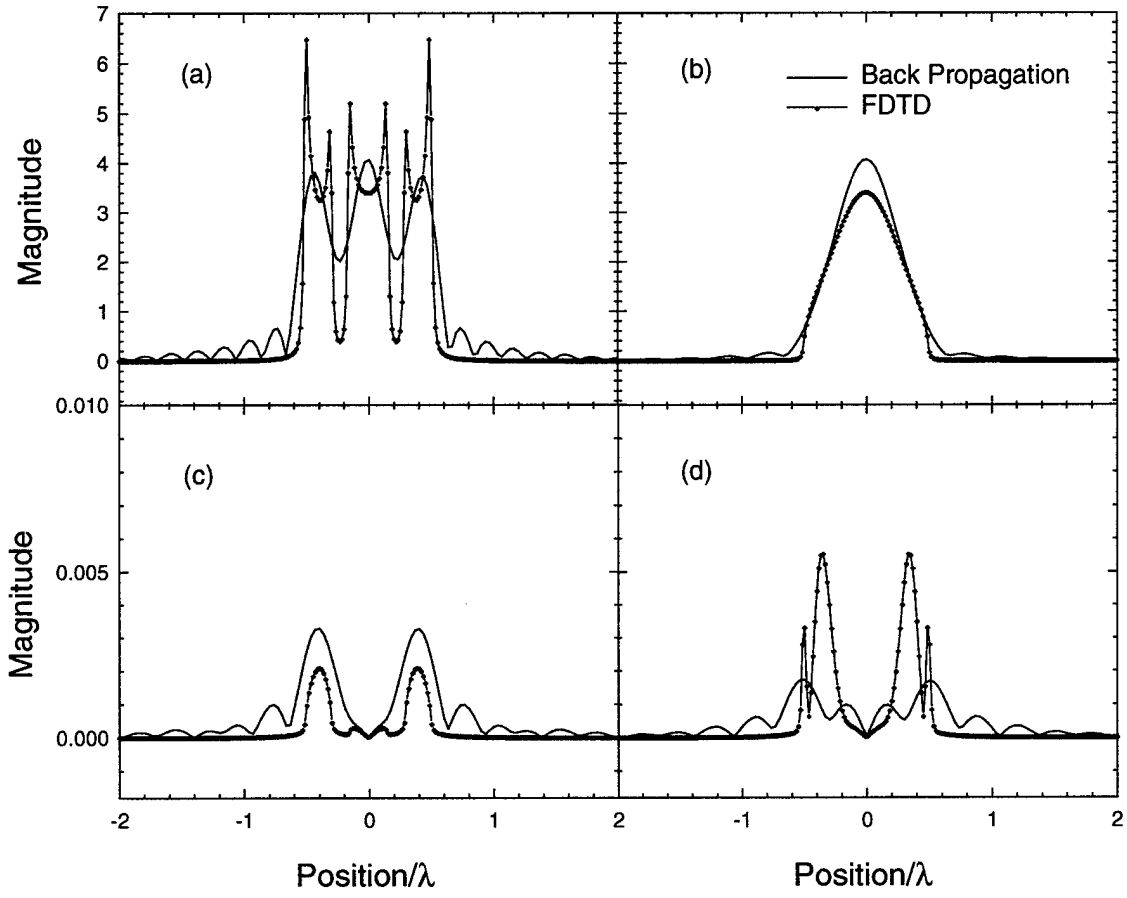

Figure 5-12 Normalized surface current computed with the back-propagation method using a 11 λ x 11 λ measurement window with a 64% probability of locating the measurement correctly and the FDTD technique for a square slotted plate. (s = 0.2 λ, d = 1 λ, SNR=80 dB, 512 total points) (a) X- Cut for J_y/H_{inc} (b) Y-Cut for J_y/H_{inc} (c) X- Cut for J_x/H_{inc} (d) Y-Cut for J_x/H_{inc}

In Figure 5-12, the surface current reconstructed from the magnetic field at randomized locations is compared with the surface current obtained from the FDTD analysis. These results indicate the randomization smooths out the current distribution. Since the data is more severely randomized than data in an actual measurement will be, these results are probably will actually occur in a measurement. As in the previous two cases, the dominant current component, J_y, is more accurately reconstructed than the much smaller component, J_x.

This study shows the back-propagation method can reconstruct the overall shape and amplitude of the surface current for these geometries under various test conditions; however, the sharp edges of the surface currents are difficult to reconstruct. In addition, the approximately 1000

times smaller cross polarized J_x component is less accurately modeled than the dominant J_y component for all six cases.

The difficulty in reconstructing the sharp edges is clarified by observing the spectrum available for back-propagation as determined by the k_{cut} values in Tables 1 and 2. These tables show the spectral bandwidth decreases from the first case to the second to the last or third case for both geometries. In addition, the figures show the sharp edges of the current distributions become less accurate from the first to the last or third case. This behavior is indicative of the property that k_{cut} is inversely proportional to R, the rise or current sharpness, as discussed at the end of section 3.1 and shown in Figure 3-6.

The back-propagation technique had more difficulty overall reconstructing the J_x component probably because it is approximately 1000 times smaller. However, in spite of the wide amplitude variation from the J_y to J_x, the amplitudes of the current distributions reconstructed with the back-propagation method were always of the same order of magnitude as the surface current amplitudes obtained with the FDTD method for all of the cases.

It is expected that as we continue to improve the technique, for example, by further optimizing the measurement truncation window and spectral domain filter, the surface current reconstruction will be improved further. At least some more improvement is expected especially since signal artifacts at the window edges shown in this section as slight ripples in Figure 5-8 and Figure 5-11 are substantially smaller than they were in preliminary computations which were made with the same spectral filter but with different α and k_{cut} values.

6 Measurements of Surface Current

In this section, the measurement system is described, along with a detailed analysis of the magnetic field probe. FDTD simulations of potential probe designs were performed to determine the best geometry for obtaining an accurate measure of the magnetic field in the presence of the probe and its associated hardware (e.g. cables). Measurements of the surface current on a slotted plate will also be presented and compared to FDTD predictions of the surface current.

6.1 Measurement System

The measurement system is shown in Figure 6-1. The purpose of this arrangement is to measure the currents on a flat plate excited by the incident field produced by the horn antenna. The measurements are taken with a computer-controlled system that moves the probe and instructs the network analyzer to take stepped frequency measurements. The target is a 30.5 cm x 30.5 cm x 0.32 cm aluminum plate containing two slots. The two slots are 20 cm x 3.8 cm and are symmetrically located about the plate center and spaced 11.1 cm apart. The plate is approximately the distance l = 107 cm in front of a standard-gain horn antenna. We chose to measure the current at 2 GHz, which is within the recommended frequency range of the waveguide feed for the horn antenna (WR 430, 1.7 GHz – 2.6 GHz).

The parameters for back-propagation (s, w, and Δx) were chosen based on the trends observed in the two-dimensional numerical analysis, discussed previously, and on the limitations of the physical system. Based on the numerical analysis, the optimum parameters are a small distance, s, a large scan window, w, and a small sample spacing, Δx. We chose a sample spacing of 1.27 cm which at the measurement frequency of 2 GHz gives $\Delta x \approx 0.1\lambda$. Thus, we could resolve features in the current on the order of 0.1λ at 2 GHz provided the SNR is high enough so that the whole measured spectrum ($\approx 10k_0$) could be used.

The size of the measurement window (w) was chosen as large as practical; in this case it extended 1λ at 2 GHz or 15 cm beyond the edges of the plate. Symmetry was employed to reduce the actual scan area to approximately one quadrant of the measurement window. A total of 29 x 27 = 783 measurement points were used over the 35.6 cm x 33.0 cm scan plane. Symmetry was used to reconstruct the measurements over the entire scan plan from the information on the one quadrant.

The last parameter, the distance, s, was made as small as feasible which turned out to be s = 1.27 cm.

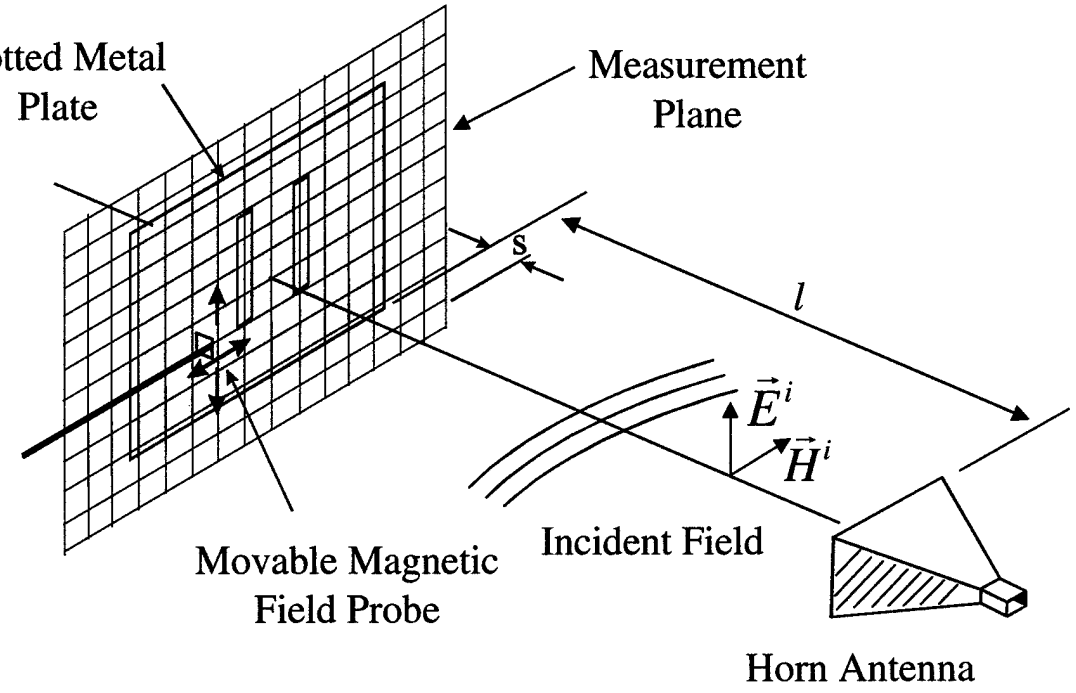

Figure 6-1. Experimental arrangement for determining the surface current on a slotted plate.

6.2 Probe Design

A balanced loop probe is employed to measure the magnetic field at the scan plane [11],[22]-[26]. Several probe configurations were tried before arriving at the design used for the measurements reported in this work. The loop design is important because the loop must operate in an environment where the fields are of arbitrary polarization due to scattering from the target. Currents will be generated in the loop by the desired magnetic field component, which is perpendicular to the plane of the loop, by electric field components that are in the plane of the loop, and by fields from any surface currents that develop on the cable attached to the loop.

6.2.1 Identifying Errors Introduced into the Measurements by the Preliminary Probe Design

The preliminary measurement system employed a simple loop probe design shown in Figure 6-2 made of a rigid coaxial cable with an outer diameter of approximately 2 mm. The loop was formed into a tear drop shape of roughly 6 cm in circumference that was in the same plane as the

twisted coax feeding the loop. A notch was cut in the coaxial cable shielding at the far side of the loop; this effectively places the load impedance at this point.

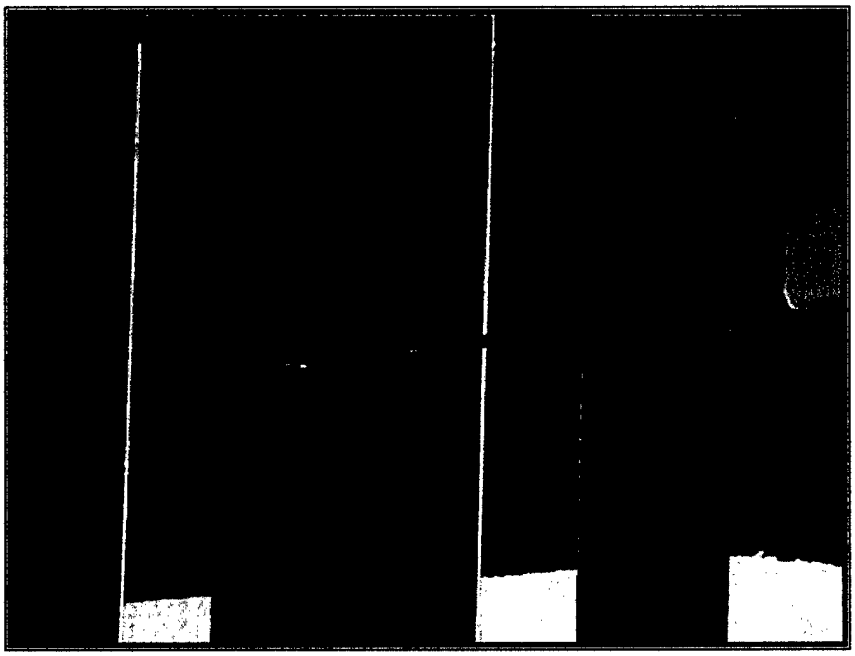

Figure 6-2. Photograph of preliminary probe being used in near field measurements for a slotted plate.

The measurement system was tested by measuring the surface current on a 30.48 cm x 30.48 cm square aluminum plate, and this surface current was compared with that computed using a finite-difference time-domain (FDTD) simulation. A comparison of the current for one of the cross sections of the plate is shown in Figure 6-3. The current reconstructed from the measurements has similar behavior and overall amplitude to the computed current distribution, but it also has many oscillations and sharper peaks near the edges of the plate. One of the differences between the measurement configuration and simulation was the absence of the probe in the simulation. Therefore, some of these errors may be due to a faulty probe design. It turns out that multiple reflections between the plate and horn also add to the error. The technique used to reduce these errors is described in Section 6.3.

To determine if the probe design is adversely affecting the measurements, a numerical simulation of the probe and plate geometry shown in Figure 6-4 was performed with a plane wave as the incident field and polarized as shown in the figure. The probe model included a perfectly

conducting bar to model the cable and a square, thin wire loop to model the actual loop. The simulated square loop had a circumference of approximately 6 cm, in order to roughly match the actual loop dimensions. A small dipole was placed where the load or gap is shown in the figure.

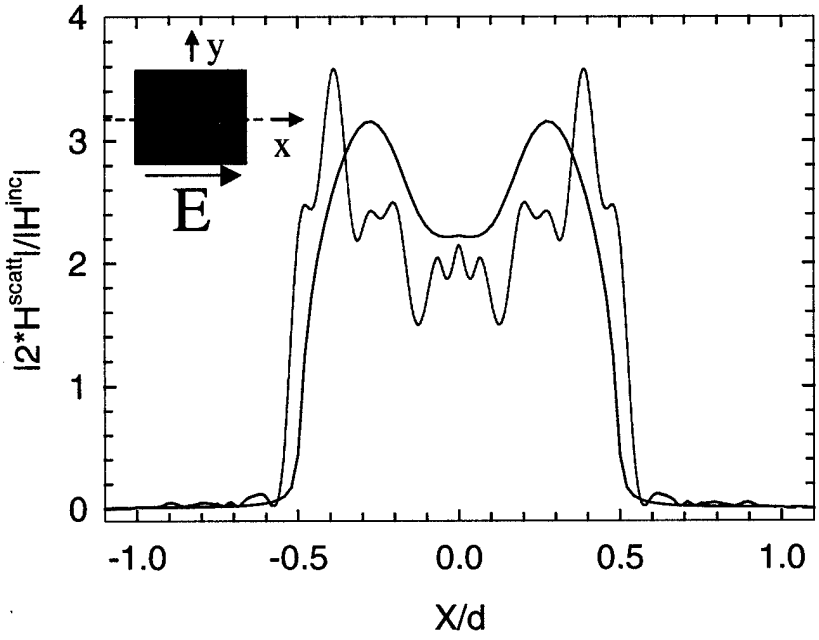

Figure 6-3. Back-propagated current and FDTD computation of current with horn source.

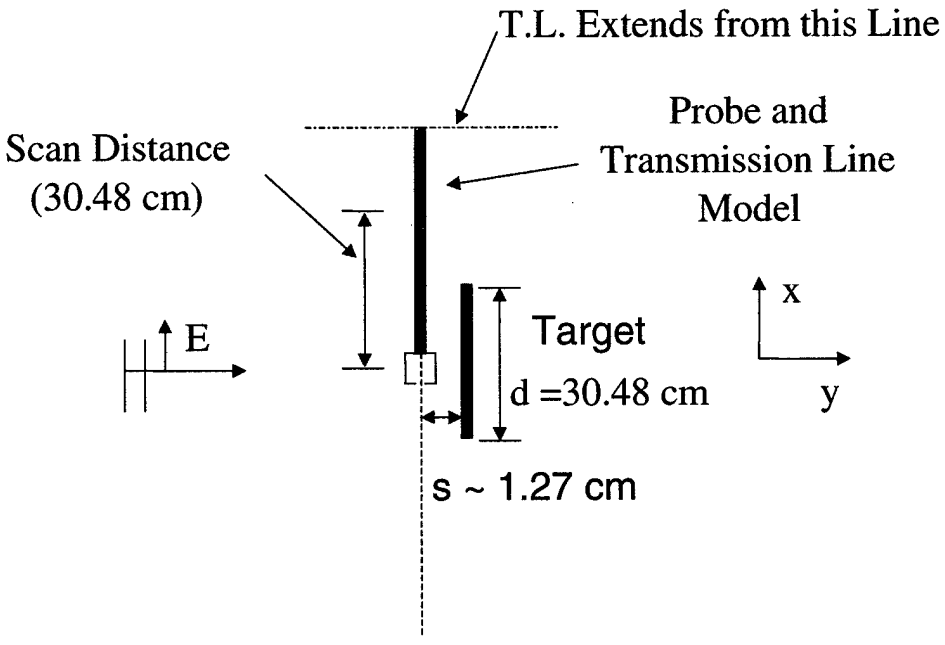

Figure 6-4. Top view of probe and plate.

The probe was scanned in the x direction over a distance of 30.48 cm (12 inches) starting at the plate center as shown in the figure. The scan line was positioned over the plate center in the vertical direction, which is not shown in this view. The probe was moved approximately 1.016 cm (0.4 inches) and then the FDTD simulation was run to compute the dipole output voltage. A total of approximately 30 FDTD simulations were performed to obtain the voltage data at all of the probe locations. Next, the plate was removed and the probe was scanned again to obtain the dipole voltages for the clear site. The clear site data were subtracted from the total voltage data to obtain the voltages corresponding to the scattered field. For comparison purposes, a separate FDTD simulation of the plate was made without the probe, and the magnetic field at the scan line was recorded. A clear site was run without the plate, and the clear site was subtracted from the field data calculated with the plate to obtain the scattered field results. The quantity picked up by the probe along the scan line is compared with the simulated scattered fields in Figure 6-5. The probe data and simulated data are both normalized by the average value of the respective clear sites. The comparison shows the probe does not accurately measure the magnetic field components at the scan line. Therefore, a better probe design is warranted.

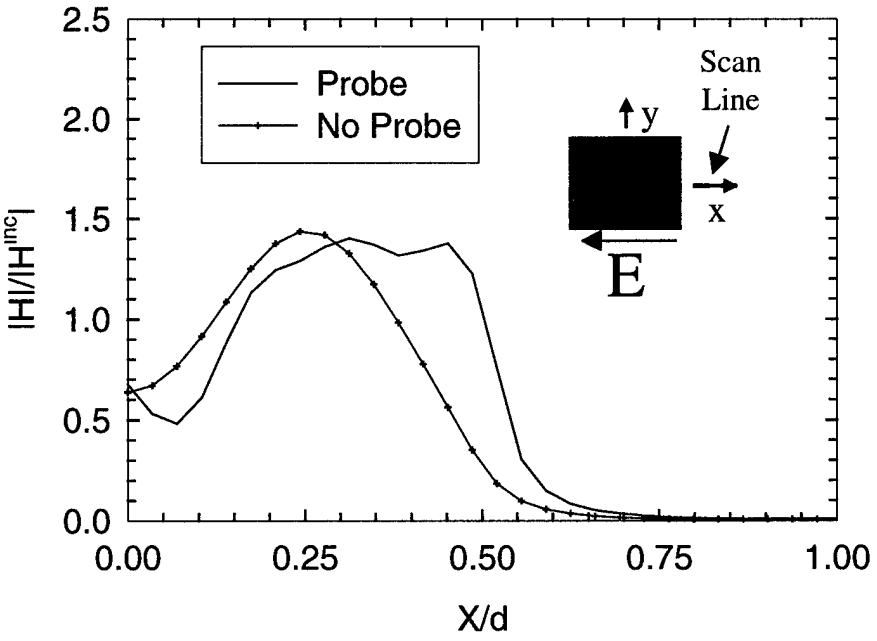

Figure 6-5. Comparison of normalized scattered fields computed from the probe to normalized scattered fields computed without the probe along the scan line.

6.2.2 Theory

To express the problem mathematically, consider the circular loop shown in Figure 6-23(a). The current in the loop can be expanded as a Fourier series in the angle ϕ [22]-[24]. The load voltage is subsequently expressed as

$$\begin{aligned} V_L &= Z_L I_0 + Z_L \sum_{n=1}^{\infty} \left(I_n e^{jn\phi} + I_{-n} e^{-jn\phi} \right) \\ &= K\omega A \hat{n} \cdot \vec{H} + Z_L \sum_{n=1}^{\infty} \left(I_n e^{jn\phi} + I_{-n} e^{-jn\phi} \right) \end{aligned}, \tag{6.1}$$

where K is a constant of proportionality, A is the area of the loop, $\hat{n}$ is normal to the surface of the loop, $\vec{H}$ is the magnetic field at the center of the loop, ω is the radian frequency, Z_L is the load impedance and the I_n are the modal currents. By Faraday's law, the $n=0$ current component has been replaced with the desired magnetic field component that is received by the loop. This equation indicates that the modal currents for $n=1,2\ldots$ must be negligible in comparison with the current for the first mode, $n=0$, for the load voltage to be mainly due to this magnetic field. Hence, the loop must be constructed and oriented so that these higher modal currents, $n=1,2\ldots$ do not contribute to the load voltage.

An equivalent circuit of an ideal probe that neglects the higher order current terms is shown in Figure 6-6. This equivalent circuit includes both the loop inductance and capacitance, which are approximately given by [22],[24]

$$L = \mu_0 b \left(\ln\left(8\frac{b}{a} \right) - 2 \right), \tag{6.2}$$

and

$$C = \frac{2\varepsilon_0 b}{\ln\left(\frac{8b}{a} \right) - 2}. \tag{6.3}$$

The parameter b is the loop radius, a is the radius of the wire, and μ_o and ε_o are the permeability and permittivity of free space, respectively. The load voltage is related to the magnetic field by the equation

$$V_L = \frac{R_L}{R_L - R_L LC\omega^2 + j\omega L} V_{oc}, \tag{6.4}$$

where the open circuit voltage V_{oc} is

$$V_{oc} \propto \omega A\left(\hat{n} \cdot \vec{H}\right). \tag{6.5}$$

The equivalent circuit indicates the ideal probe exhibits the frequency response of a low-pass filter.

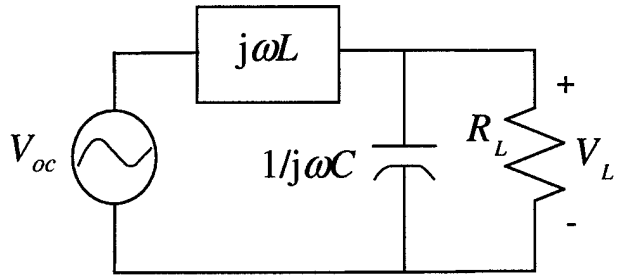

Figure 6-6. Equivalent circuit for the ideal loop probe.

6.2.3 Numerical Modeling

A numerical experiment was carried out using an FDTD simulation to determine an appropriate probe geometry for use in the near-field measurements; the different geometries tested are shown in Figure 6-7. The parameters that were varied to determine the best design are the location of discrete electrical loads on the loop, the number of loads (one or two at most), and the location and orientation of the coaxial line as shown in Figure 6-7. To keep down the memory and CPU requirements of the numerical simulations, a very simplified model of the probe was used. A plane wave with the polarization in Figure 6-7 instead of the spherical wave launched by the actual horn was employed as the source. A square loop (approximately 1.59 cm x 1.59 cm) of similar size to the initial probe employed in the GTRI measurement system was studied. The loop was fed by transmission lines matched to a load of 50 or 100 ohms. For this study, the singly-loaded loop probes were loaded with 100 ohms, and the doubly-loaded loop probes were loaded with two 50 ohm loads.

To model the currents on the outside of the coaxial cable connected to the actual probe, a perfectly conducting bar of approximately 0.53 cm x 0.53 cm square x 19 cm in length was attached

to the loop as shown in Figure 6-7. The length of the bar was chosen to be longer than 1 wavelength at the actual measurement frequency of 2 GHz.

Ideally, the probe should be sensitive only to the magnetic field normal to the loop area. Three probe geometries shown in Figure 6-7 were studied. They were the ideal probe, which was modeled as a wire loop in free space (*Loops* in Figure 6-7), and the two more realistic probe models, which consisted of a wire loop attached to a perfectly conducting metal bar (0.53 cm x 0.53 cm x 19 cm) oriented either parallel to the electric field (*E-Bar Loop*) or parallel to the magnetic field (*H-Bar Loop*). The simulations were performed by taking a single loop configuration from this matrix of geometries and placing it in the FDTD grid.

The characteristic used to determine the effectiveness of the loop at sensing the magnetic field was the probe sensitivity or transfer function given by

$$\text{Probe Sensitivity} = \left| \frac{V_L(\omega)}{\omega A \hat{n} \cdot \vec{H}(\omega)} \right| \tag{6.6}$$

where $\vec{H}$ is the incident magnetic field with the loop absent, and V_L is the voltage across the single load (*singly-loaded loop*) or the sum or difference of the voltages across the two loads (*doubly-loaded loop*). For the doubly-loaded or balanced loop, the magnetic field response corresponds to the difference voltage.

The sensitivity of the most effective probe geometry should approximate that of an ideal circular loop of equivalent area, which has the response given by (2.5) and is independent of the electric field present at the loop.

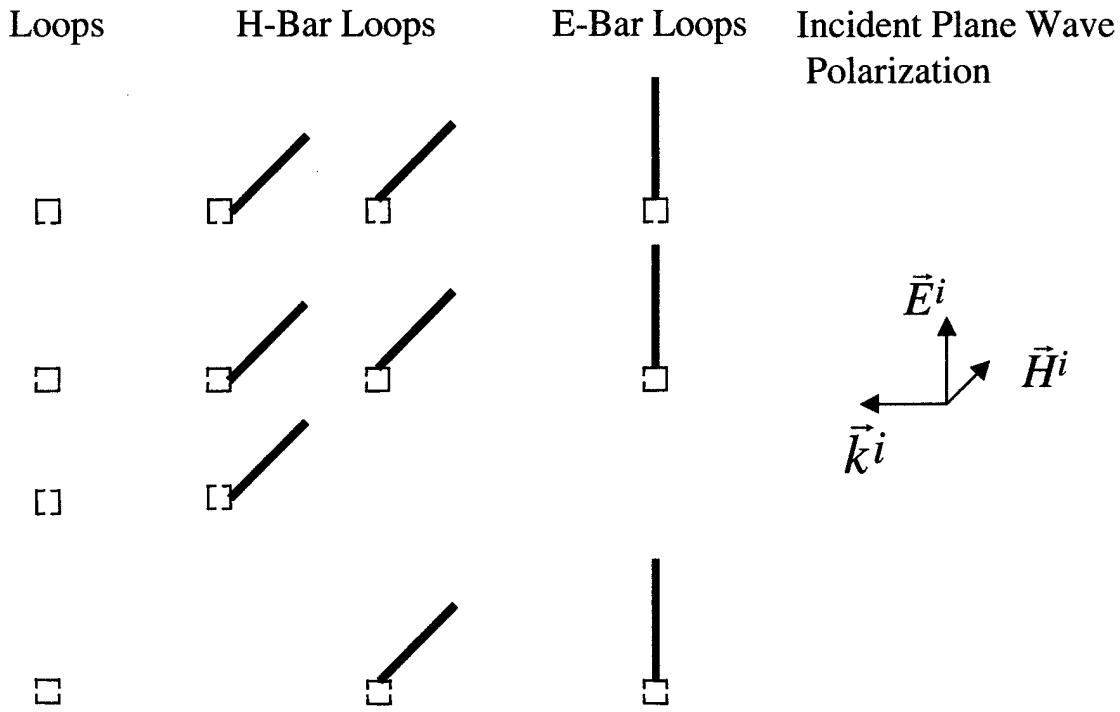

Figure 6-7. Probe configurations used in the study. Singly-loaded probes have a 100Ω termination and doubly-loaded probes have two 50Ω terminations.

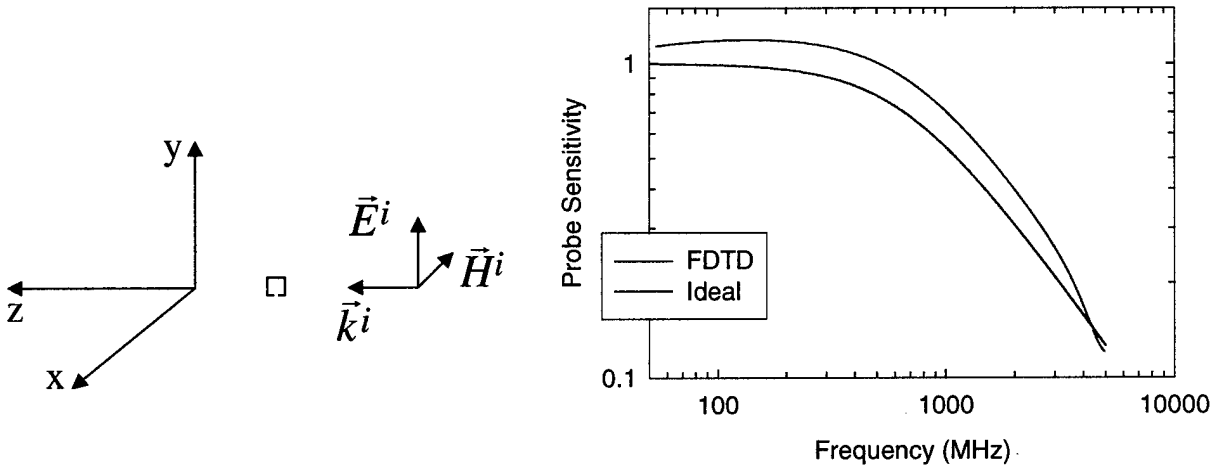

Figure 6-8. Probe sensitivity for singly-loaded loop perpendicular to the electric field compared to probe sensitivity computed for the equivalent circuit of the ideal loop.

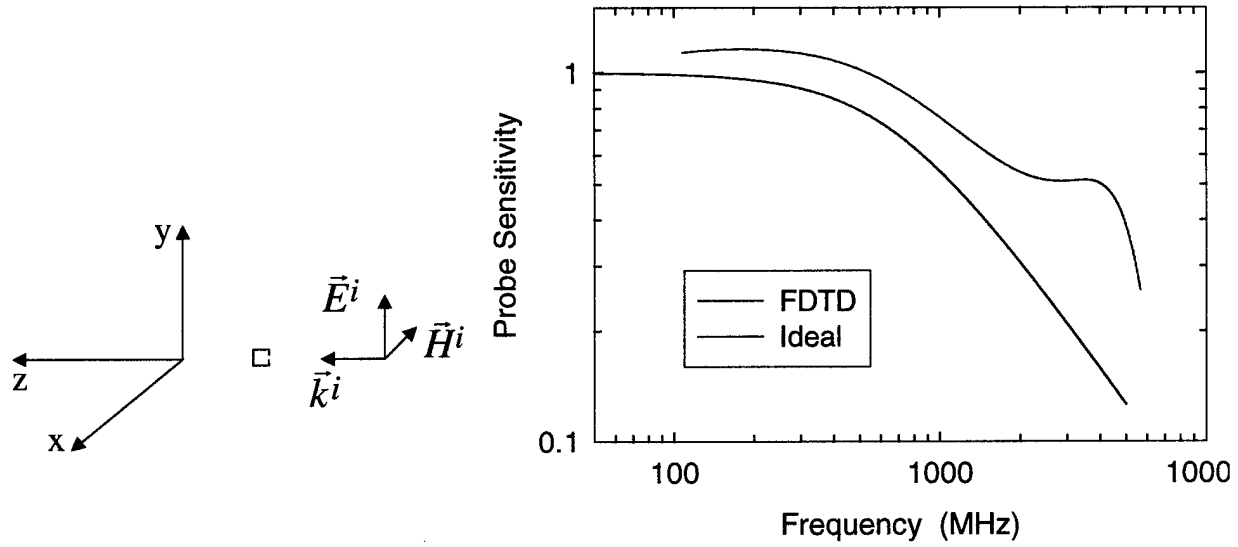

Figure 6-9. Singly-Load loop with load parallel to the electric field.

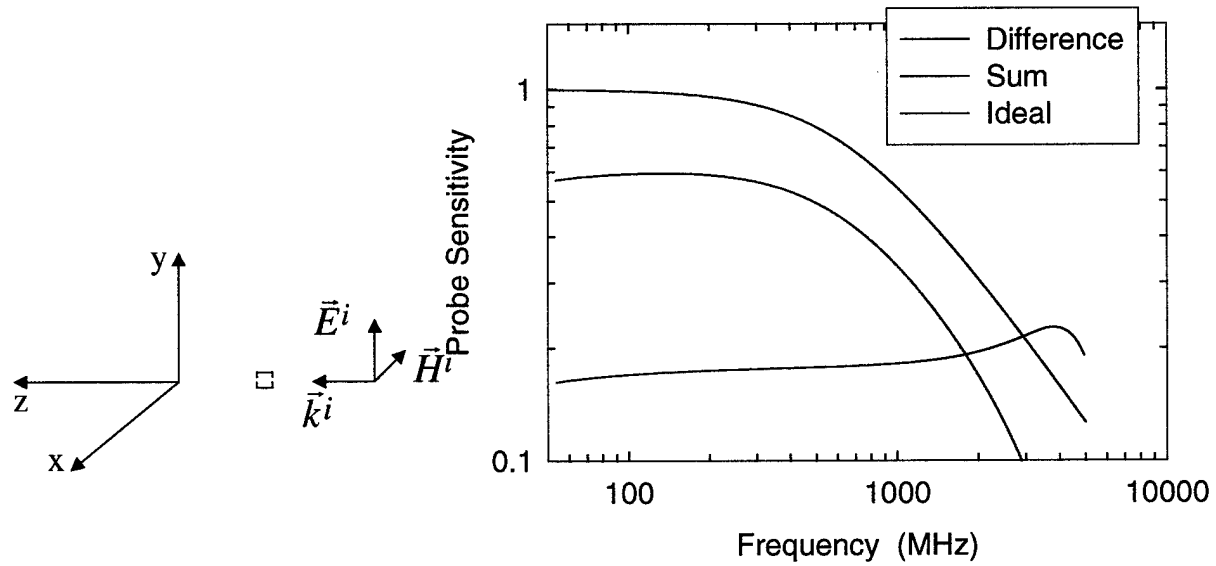

Figure 6-10. Doubly-loaded loop probe with loads parallel to the electric field.

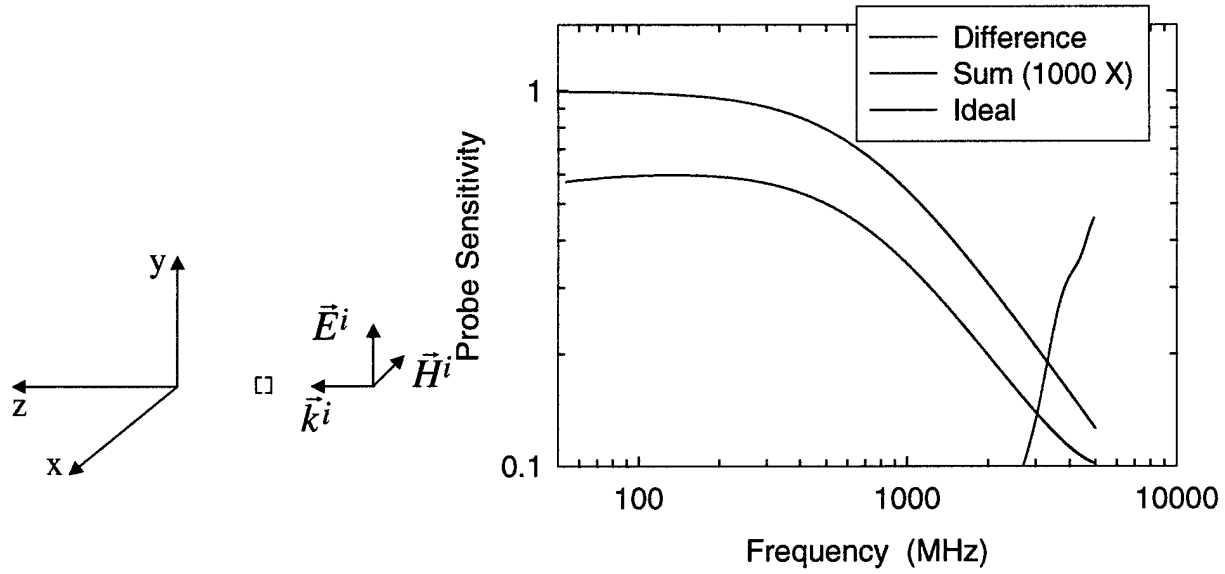

Figure 6-11. Doubly-loaded loop probe with loads perpendicular to the electric field.

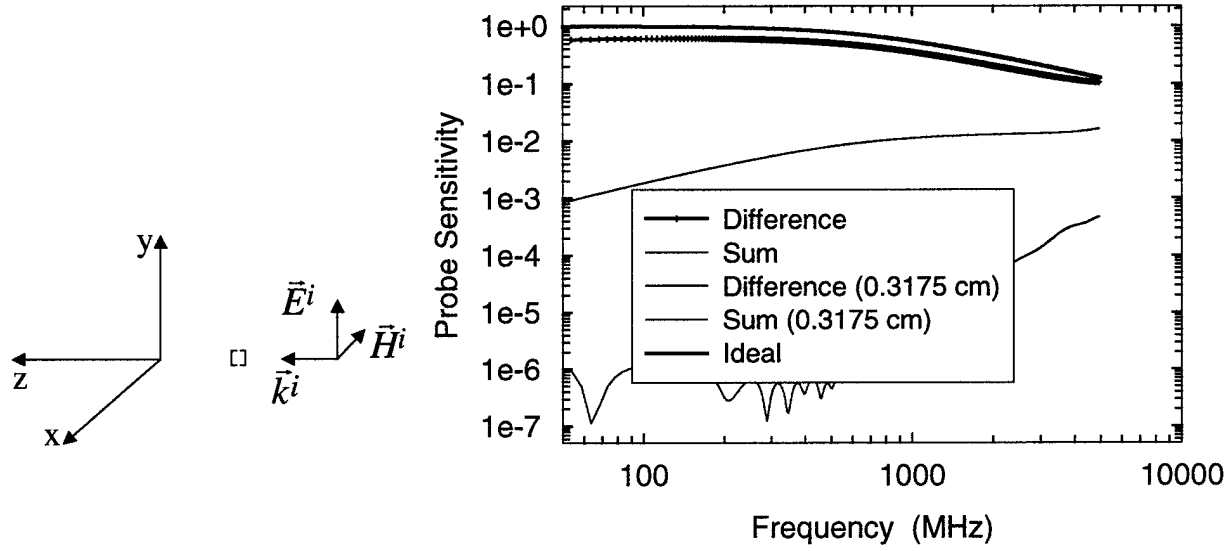

Figure 6-12. Effect of changing line length asymmetrically for doubly-load loop probe with load perpendicular to the electric field. (Asymmetry is not shown in the sketch of the probe. See text for discussion of asymmetry.)

6.2.3.1 The Ideal Loop Response

The sensitivities of the FDTD probe models were compared with that of an ideal loop (Figure 6-23) of similar dimensions to the FDTD model loop. The dimensions of the ideal (circular) loop were taken from those of the FDTD (square) loop to be a = 0.688 mm and b = 7.94 mm. A value

of 100 ohms was used for the load impedance. The inductance and capacitance computed from (2) and (3) for this loop are 25 nH and 0.056 pF, respectively. The inductance is the more significant parameter for this loop and the frequency range of interest (< 3 GHz). These dimensions were based on the FDTD unit cell size of 5.293 mm with 3 unit cells per side of the square loop. The wire radius, a, was based on the approximation that the equivalent wire radius is 13% of the cell size, and the loop radius, b, was roughly estimated as one-half the length of a side of the square loop. These values gave good results in comparison with the FDTD model data. When the loop radius was based on the square loop area, the results did not agree as well.

The probe sensitivity is shown in Figure 6-8 through Figure 6-11 for the numerical models labeled "Loops" in the matrix in Figure 6-7 and compared with that of the ideal loop. The sensitivity for the loop configuration in Figure 6-8 compares well with the sensitivity of the ideal loop model. The discrepancies between the two results are understandable considering that the numerical computation is for a square loop, and the ideal loop is circular. In addition the radius of the wire used in the numerical model is difficult to determine from the discretization but is roughly 13% of the unit cell size. The comparison in Figure 6-9 is not as good, indicating the loop does not exhibit the ideal loop behavior for the electric field parallel with the load. This is because the load acts like a dipole to the incident electric field and therefore is responding to both the magnetic flux enclosed by the loop as well as the electric field sensed by the load.

It is clear from the ideal loop response that the sensitivity of this design is significantly down at the measurement frequency of 2 GHz, since the loop is operating well beyond the 3 dB corner frequency. Therefore, the loop needs to be significantly smaller in size to operate at 2 GHz.

The numerical results in Figure 6-8 and Figure 6-9 indicate that for the singly-loaded loop, the optimum case is with the load perpendicular to the electric field. When the load is perpendicular to the electric field, nulls in the electric field occur at the load because the significant higher order current modes excited by the electric field effectively add to zero at the load and do not contribute to the load voltage. When the load is parallel to the field, it picks up the electric field. The higher order current modes that result contribute to the load voltage and change the low-pass response from that of the ideal loop.

The doubly-loaded probe responses with the loads either perpendicular or parallel to the electric field are shown in Figure 6-10 and Figure 6-11. For this geometry, two outputs are available

from the two loads. The voltage outputs can be combined to provide a response to the magnetic field. For this study, the dipoles on both sides of the loop are polarized in the same directions so that the circulation component of the field or the magnetic component is obtained by taking the difference of the two voltages.

In comparison with the ideal loop probe sensitivity, the best case for the doubly-loaded probe occurs with the loads perpendicular to the electric field. Ideally for the doubly-loaded probe the difference channel (magnetic field output) will behave with the ideal filter characteristic, and the sum channel output will be substantially lower in magnitude than the difference channel output. This characteristic is important because in a real probe, the channels are not completely isolated from each other.

One additional problem with the doubly-loaded loop that does not occur for the singly-loaded loop is the effect of the balance in the loads on the probe performance. If the two loads are not identical or if the line lengths from one load to the coupler differs from the line length from the other load to the coupler, the sum and difference channels of the coupler may not be capable of extracting the magnetic field from the voltage outputs of the probe. To check this problem, the configuration in Figure 6-11 was rerun with an additional length of 3.175 mm (1/8 inch) added to one line by delaying the time domain voltage waveform for that load. The results are compared with the transfer function of the balanced doubly-loaded loop without the shift in Figure 6-12. The magnitude of the difference channel does not change significantly, but the sum channel output increases substantially. Although not shown, the phase response does not change significantly for the difference channel either for the 3.175 mm line length difference. Thus, the probe can tolerate some asymmetry, but it is best to maintain the balanced characteristics as much as possible.

So far, the best case of both the singly-loaded probe and doubly-loaded probe are similar so either one seems feasible. However, when the loads are oriented such that they pick up the electric field (loads parallel to the electric field), the doubly-loaded probe maintains the ideal filter response. In near field measurement conditions the total electromagnetic field is not in a plane wave configuration due to the presence of the scattered field, and, hence, it is not possible to orient the probe such that the loads are always perpendicular to the electric field. Under these conditions, the doubly-loaded probe is better than the singly-loaded probe because it can more effectively isolate the desired magnetic field from the presence of the electric field components.

6.2.3.2 H-Bar and E-Bar Loops

The next two sets of studies were designed to determine an effective orientation for the coaxial cable connected to the probe. The main cases under consideration were the following:

i) H-Bar Loop: Bar parallel to the magnetic field and on either the loop top or side (Figure 6-13 through Figure 6-18)

ii) E-bar Loop: Bar parallel to the electric field (Figure 6-19 through Figure 6-21)

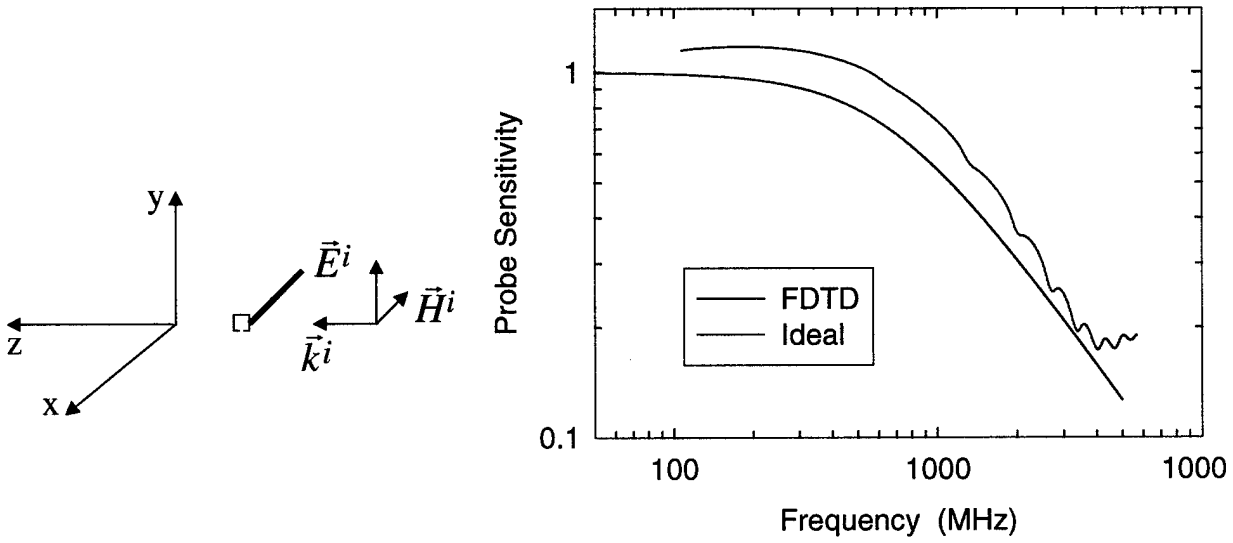

Figure 6-13. Singly-loaded H-Bar loop with load perpendicular to the electric field.

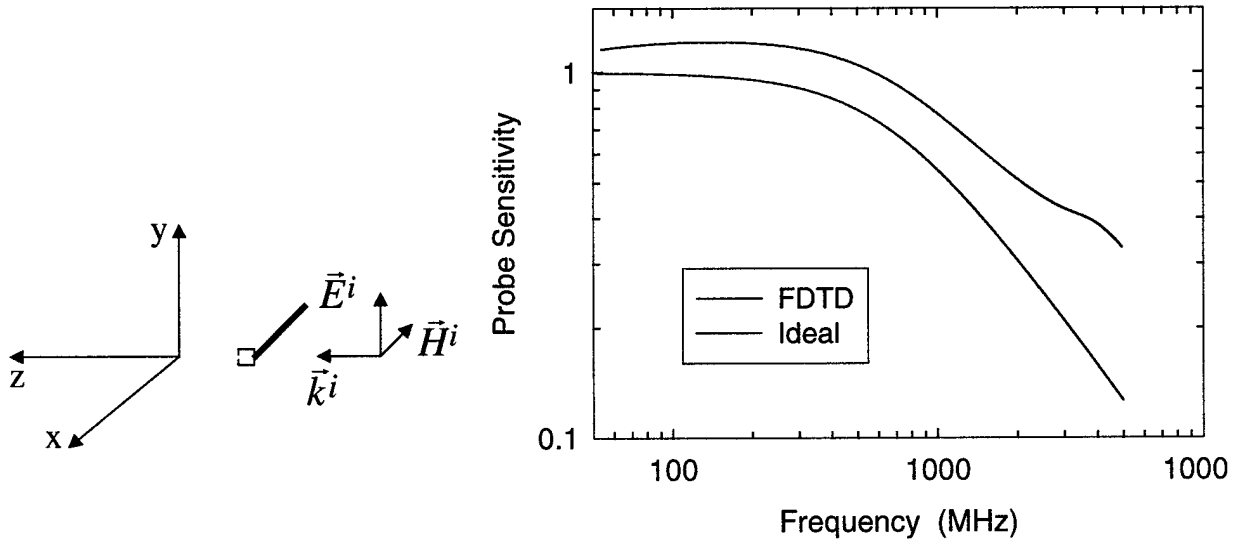

Figure 6-14. Singly-loaded H-Bar loop with load parallel to the electric field.

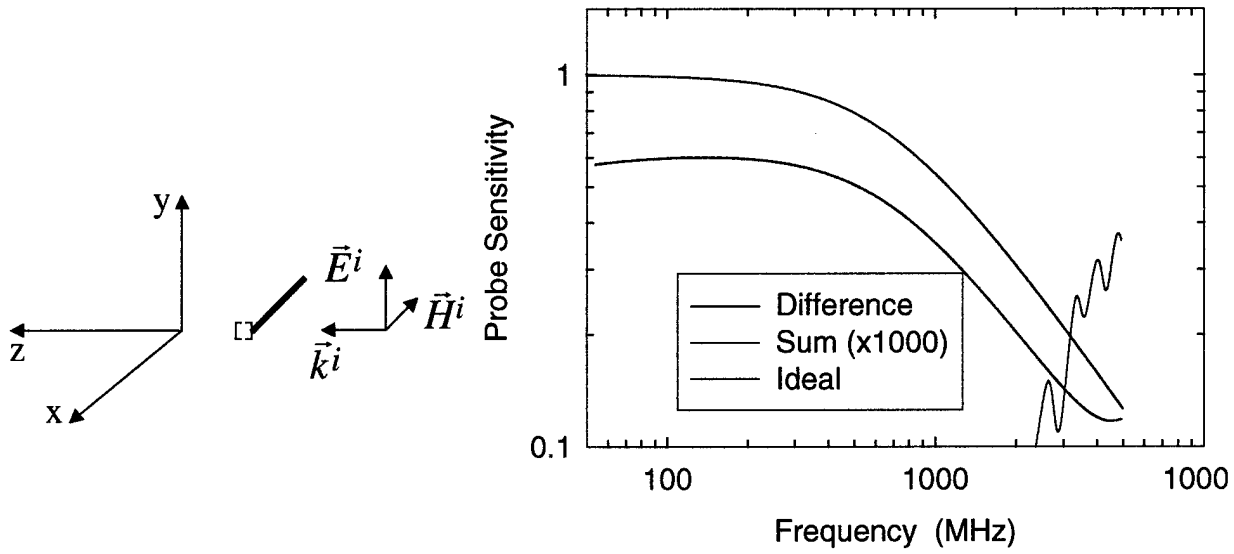

Figure 6-15. Doubly-loaded H-Bar loop with loads perpendicular to the electric field.

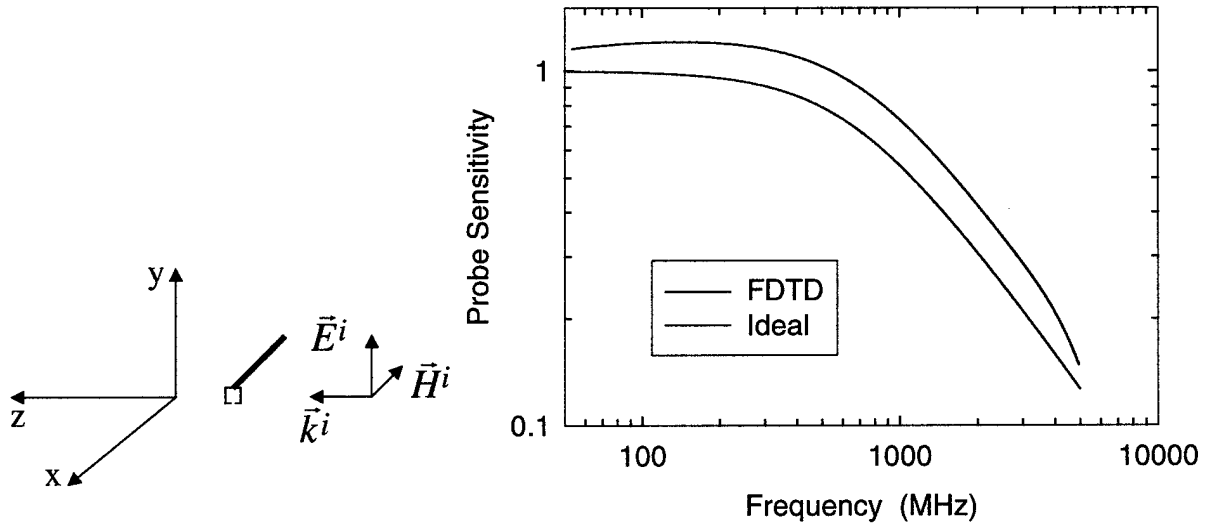

Figure 6-16. Singly-loaded H-Bar loop with load perpendicular to the electric field.

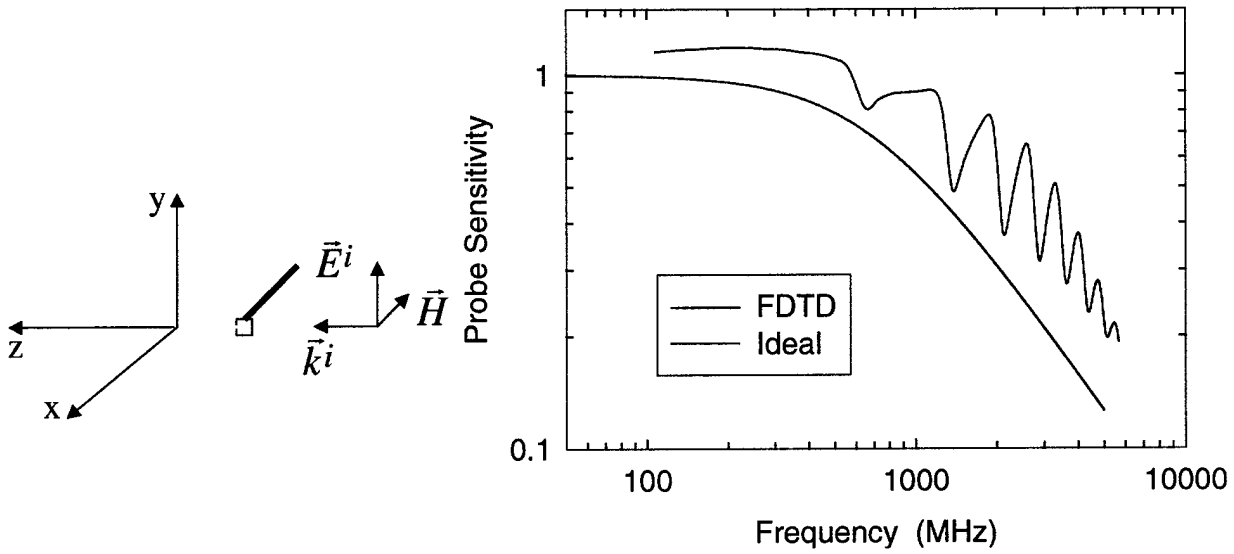

Figure 6-17. Singly-loaded H-Bar loop with load parallel to the electric field.

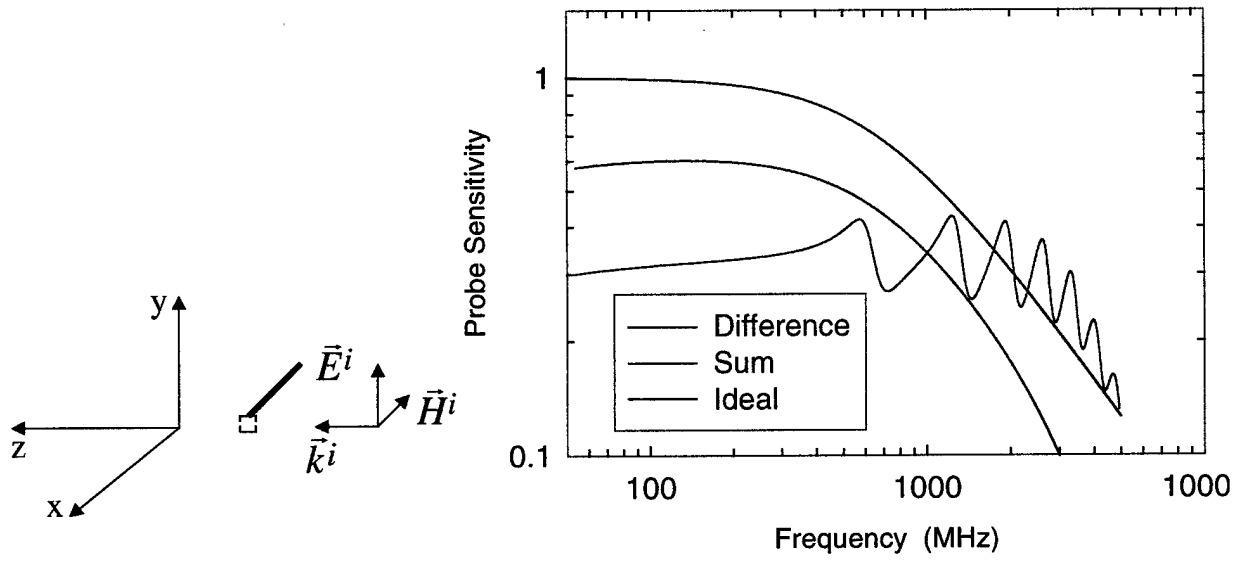

Figure 6-18. Doubly-loaded H-Bar loop with loads parallel to the electric field.

First, consider the bar parallel to the magnetic field and on either the top or side of the loop as shown in the matrix and Figure 6-13 - Figure 6-18. For the singly-loaded cases, the best sensitivity to the magnetic field is for the bar on the top of the loop, opposite the load as shown in Figure 6-16. Note that the load is again perpendicular to the electric field. When the whole assembly is rotated such that the load is parallel with the electric field, the sensitivity is corrupted by the electric field pick up of the load as shown in Figure 6-14.

For the doubly-loaded loop only two orientations were studied as shown in the matrix and Figure 6-15 and Figure 6-18. Both configurations provide a response close to the ideal probe response in the difference channel, but the lowest response from the sum channel occurs as shown in Figure 6-15 for the bar on the side of the loop with the loads perpendicular to the electric field.

Considering that with actual measurements the configuration of the load(s) parallel with the electric field is not always possible to maintain, the doubly-loaded probe is overall better than the singly-loaded probe. In other words, the doubly-loaded probe handles the worst case of the electric field parallel with the loads, whereas, the singly-loaded probe sensitivity becomes unacceptable for this case.

The last part of this study will cover the "E-Bar Loops" in which the bar is parallel with the electric field. The probe sensitivity plots are given in Figure 6-19 - Figure 6-21. The best cases here are the singly-loaded probe in Figure 6-19 and the difference channel of the doubly-loaded probe shown in Figure 6-21. The singly-loaded probe sensitivity appears to approximate the ideal probe response but is slightly different above 3 GHz, so it is probably sensing the electric field as well and is not acceptable. Considering that the singly-loaded loop in free space can respond to the electric field if it is parallel to the loads (Figure 6-9), this geometry will probably also respond to the electric field for this polarization as well, providing further reason not to use this design. The doubly-loaded sensitivity is unacceptable because the magnitude of the sum channel output is larger than the magnitude of the difference channel output.

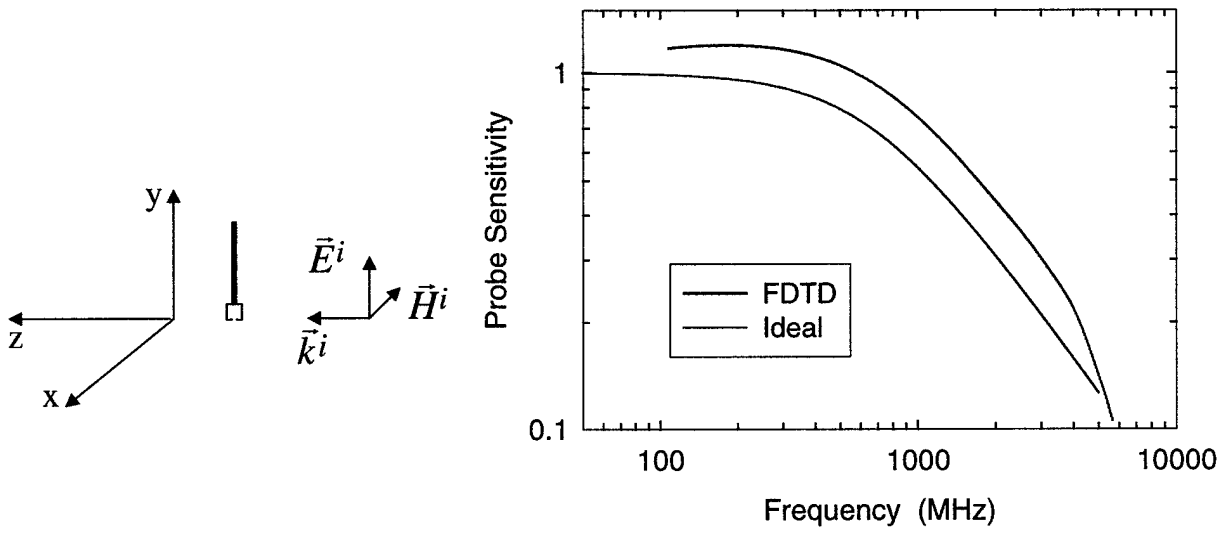

Figure 6-19. Singly-loaded E-Bar loop with load perpendicular to the electric field.

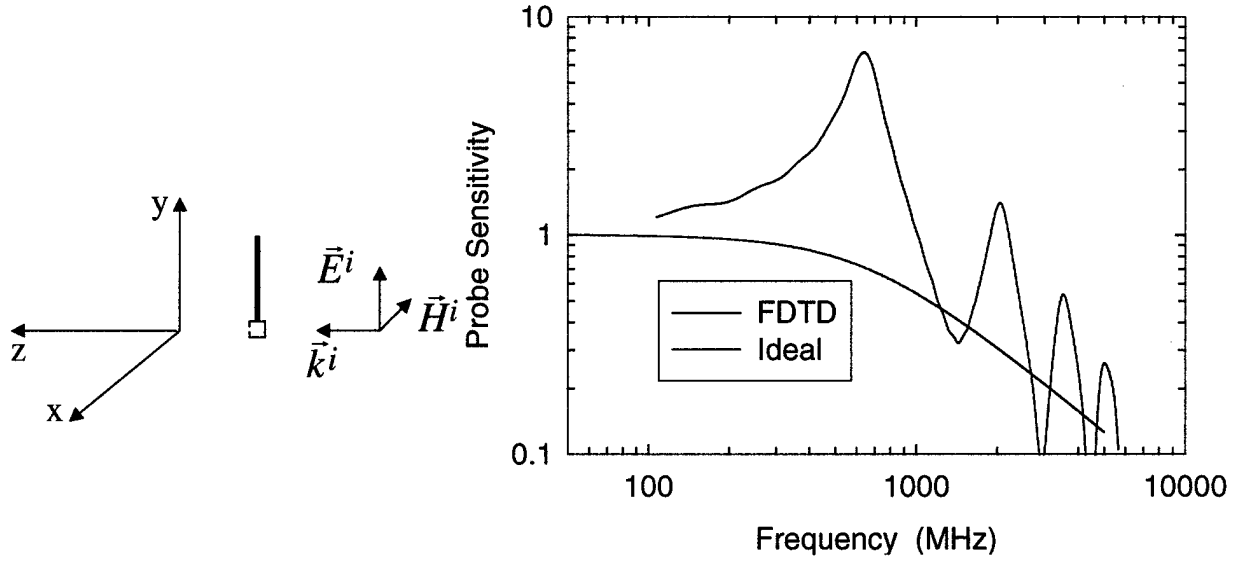

Figure 6-20. Singly-loaded E-Bar loop with load parallel to the electric field.

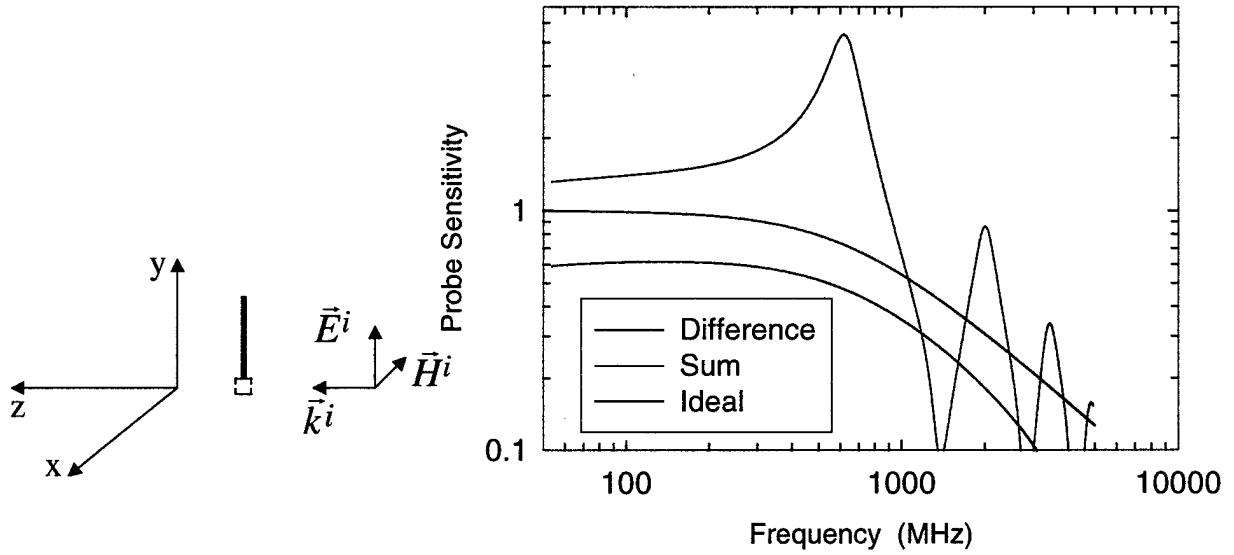

Figure 6-21. Doubly-loaded E-Bar loop with loads parallel to the electric field.

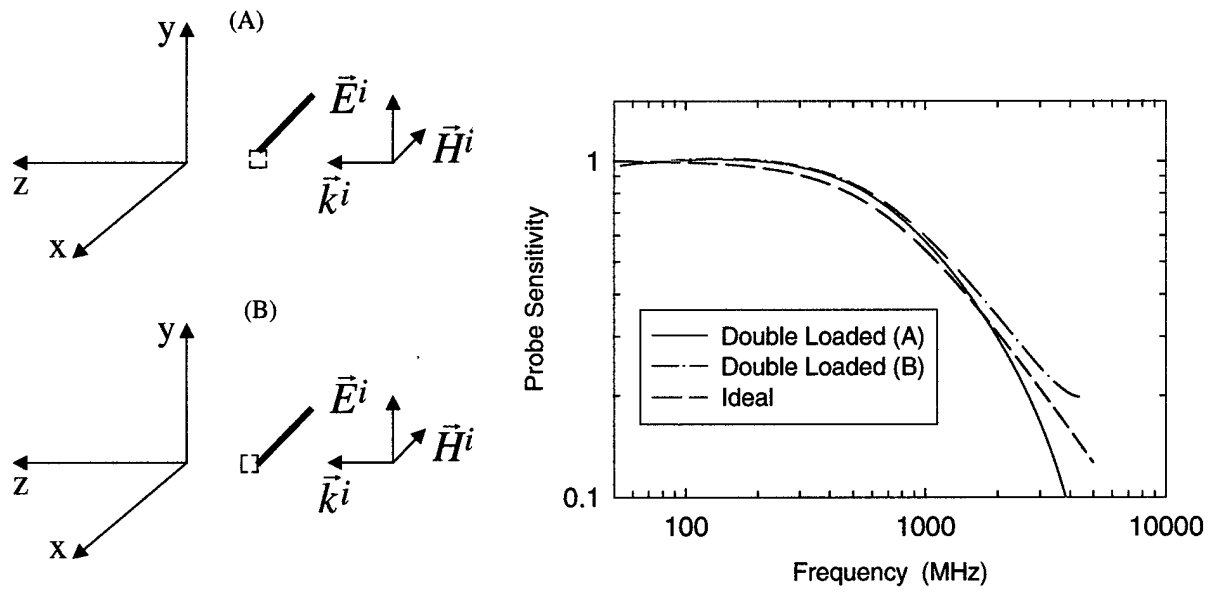

Figure 6-22. Sensitivity of the doubly loaded H-Bar loop for two different orientations with respect to the incident plane wave compared with the sensitivity for the ideal probe. The difference voltage from the doubly loaded probe is shown. (Loop dimensions for the equivalent circuit are a = 0.0688 cm, b = 0.794 cm giving L = 25 nH and C = 0.056 pF.)

These studies indicate the best loop configuration in the matrix in Figure 6-7 is the H-Bar doubly-loaded loop. The probe sensitivity of the other realistic configurations was unacceptable. In the case of the singly-loaded loop geometries, the incident electric field could induce higher order modal currents in the loops, and these currents affected the probe sensitivity. In the case of the failed doubly-loaded geometry (Figure 6-21), the sum channel response was too high.

On the other hand, the H-Bar doubly-loaded loop probe sensitivity shown in Figure 6-22 follows that of the ideal loop. In this figure, the doubly-loaded loop sensitivities are normalized to approximately 1.0 for better comparison with the sensitivity of the ideal loop. Its response is largely independent of the two orientations of the loop with respect to the direction of the incident wave. This result shows the difference-voltage output of the balanced probe configuration is insensitive to the higher order currents, thus it is mainly due to the magnetic field, even when an electric field is present. In practice, the bar is oriented normal to the incident electric field to reduce currents induced on the bar by the incident field.

From these observations several probe design considerations can be summarized:

i) The probe must be as small as possible with respect to the wavelength of interest to keep its operating point below the 3 dB frequency of the probe sensitivity characteristic.

ii) The probe with the double loads should be employed because it is more effective than the singly-loaded probe at sensing the magnetic field under different electric field polarizations.

iii) The doubly-loaded probe must be as symmetric as possible to maintain high isolation between the sum and difference outputs.

iv) The coaxial cable should be oriented perpendicular to the plane of the electric field or designed to minimize the pick up of stray surface currents on the shielding.

Characteristic (i) concerning the probe size is important because the probe works best when it is operated on the flat portion of the low-pass filter characteristic. Characteristic (ii) concerning the double loads is important because, for near field measurements, the probe must be able to accurately sense the magnetic field in the presence of the electric field of any polarization. Characteristic (iii) concerning the need to have an evenly balanced, symmetric doubly-loaded probe is important because under near field measurement conditions, the magnitude of the sum channel output can be significant enough to distort the difference channel output if the isolation between the two outputs is poor.

Criterion (iv) concerning the coaxial cable orientation also affects the probe output voltage, but it is not always possible to prevent the cable from picking up stray currents by orientation alone. In near field measurements, the device being measured can scatter fields of different polarization and in arbitrary directions. Therefore, additional means may be required to reduce the probe sensitivity to surface currents on the coaxial shielding. Two possible methods are to use a filter to prevent standing waves from building up on the cable at the measurement frequency of interest or to coat the cable with absorber. A more expensive approach is to employ circuitry and fiber optics to replace the coaxial cable.

6.2.4 Final Probe Design

For the actual probe geometry, the loop was tear-drop shaped; its inner diameter varied from 0.41 cm to 0.66 cm and the coaxial cable diameter was 0.119 cm (0.047 inches). A sketch of the probe is shown in Figure 6-24. To approximate its sensitivity, we set $a = 0.6$ mm and $b = 2.7$ mm, the average of 0.41 cm and 0.66 cm. The sensitivity (6.6) of the resulting equivalent circuit was approximately -1.5 dB at the measurement frequency of 2 GHz, which was sufficient for our

measurements. The probe was built from two small coaxial cables of approximately equal electrical length. The cables were placed side by side in a metal tube. The two loads of the balanced probe were formed by soldering a small half loop of solid wire, similar in diameter to the coaxial shielding, to the inner conductors of the coaxial cables, which extended slightly beyond the outer shielding. The plane of the loop was at a 90° angle to the metal tube (bar in previous discussion). The difference of the coaxial outputs was obtained with a hybrid junction.

6.3 Measurement and Simulation Procedures

Measurements were made for the slotted plate using the small balanced loop probe and system shown in Figure 6-1 and compared to a simulation of the measurement system performed using the FDTD method. First, the measurement procedure will be described and then the numerical model will be discussed. The network analyzer took data over a range of frequencies at each sampling point for both the slotted plate target and a clear site (i.e., no plate present). The scattered field was then computed by differencing these results. Once the data were taken, the first step of the post processing was to time gate out the multiple reflections between the horn and plate and from other objects in the room. To do this, the frequency measurements were filtered with a Gaussian shaped filter centered at 2 GHz to remove extraneous frequencies but to leave enough bandwidth to see the time-domain signal. Next, an inverse FFT was taken of the Gaussian filtered data to obtain the time signature. In the time domain, the multiple reflections between the plate and horn, for example, were clearly seen to occur at approximately the time $t = 2l/c$ beyond the beginning of the pulse waveform, where l is the distance from the horn to the plate, see Figure 6-1. After removing the spurious reflections, the time-gated results were transformed back into the frequency domain, and then the measured results at 2 GHz were selected.

These data were back-propagated from the scan plane to the plate, and the surface current distribution was reconstructed. Before back-propagation, the measurements at the scan plane were windowed to smoothly taper the measured data at the edges of the scan plane to zero. The window employed for this task was flat in the center and tapered to zero at the edges as a cosine function. Typically, 49% - 72% of the window area was flat, and the rest of the area was tapered.

In addition to the spatial window, a two-dimensional version of the one-dimensional spectral filter given in (4) was employed. The spectral filter parameters were α, k_{xcut}/k_0, and k_{ycut}/k_0. These parameters are adjustable over a limited range. Recall that the maximum usable evanescent

spectrum depends upon the measurement distance, sample spacing, probe size, and noise level, as discussed earlier.

The FDTD method was used to model the horn and slotted plate geometry. The horn was modeled with a staircased grid where necessary, and symmetry was employed to reduce the size of the mesh. An orthogonal grid consisting of cubic unit cells was employed. The unit cell dimension was 0.3175 cm, the mesh size was 600 x 130 x 210 cells, and 4000 time steps were used. The sample spacing between the observed field data at the plate was 0.635 cm. The surface current or normalized scattered field on the plate was computed using the scattered tangential magnetic field at the surface of the plate.

6.4 Measured Results

The measured results for the current distribution on the slotted plate are compared with the results predicted from the FDTD calculations in Figure 6-25 and Figure 6-26. In Figure 6-25, the slots in the plate are parallel to the incident electric field, and in Figure 6-26 the slots in the plate are perpendicular to the incident electric field. Note the ordinate is labeled in terms of normalized scattered magnetic field instead of surface current. This label was chosen because the plots show the field beyond the edges of the plate and across the slots where there is no actual current. The parameters used for the spatial and spectral windows are given in the figures. The spatial windows were smaller than the actual scan area, and the spectral windows included the evanescent modes with k_x ranging from approximately $2.5k_0$ to a maximum of $4k_0$. The spatial and spectral window sizes were chosen so as to smooth out any artifacts near the plate edges in the reconstructed current distribution without losing too much of the useful evanescent spectrum.

The measured data agrees overall with the results computed from the FDTD simulation. Both results show the expected behavior: the current is nearly singular at the edges of the plate that are parallel to the incident electric field—Figure 6-25(a) and Figure 6-26(a), while the current goes smoothly to zero at the other edges—Figure 6-25(b) and Figure 6-26(b). In Figure 6-25(b) and Figure 6-26(b), the spatial resolution (0.25λ and 0.33λ, respectively) is sufficient to resolve the current distribution. However, in Figure 6-25(a) and Figure 6-26(a), the spatial resolution (0.33λ and 0.4λ, respectively) is insufficient for reconstructing the nearly singular behavior of the current at the edges. This is to be expected because the edge singularities require a large spatial spectrum to accurately represent them. More spectrum than used in the figures is available: up to the probe

sample spacing of 0.1λ. However, measurement noise and uncertainties precluded the use of this spectrum. Overall, the measured current agrees fairly well with the simulated results.

6.5 Conclusions

By measuring the magnetic field a small distance in front of the surface of interest, the plane-wave spectral back-propagation technique can be used to obtain an approximate measure of the current distribution on the surface by capturing both the propagating spectrum and a portion of the evanescent spectrum. The main advantage of this approach is that it does not require the object under test to be modified.

The comparison of the measurements with the FDTD simulations showed that the approach is feasible. Practical measurement considerations, such as noise and the size and location of the measurement surface, ultimately limit the spatial resolution of the technique. By adjusting the spatial window the edges of the measurement data can be tapered to zero, and by adjusting the spectral window the more noisy part of the evanescent spectrum can be removed. After processing, the features of the current distribution that are within the resolution of the technique can be reconstructed.

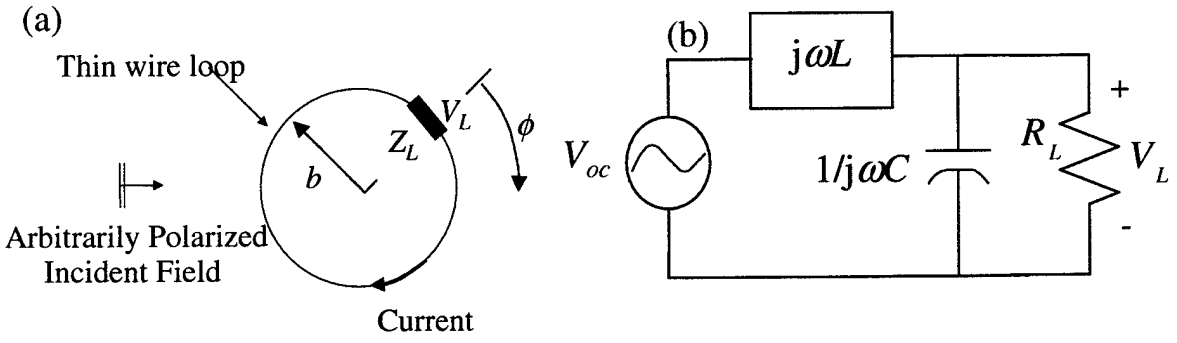

Figure 6-23. (a) Circular loop probe with the load impedance Z_L. (b) Equivalent circuit for the ideal loop probe.

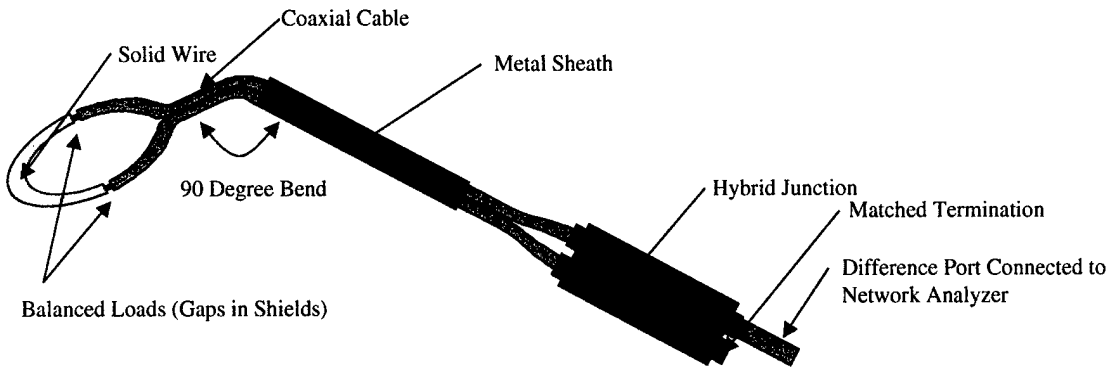

Figure 6-24. Sketch of measurement probe.

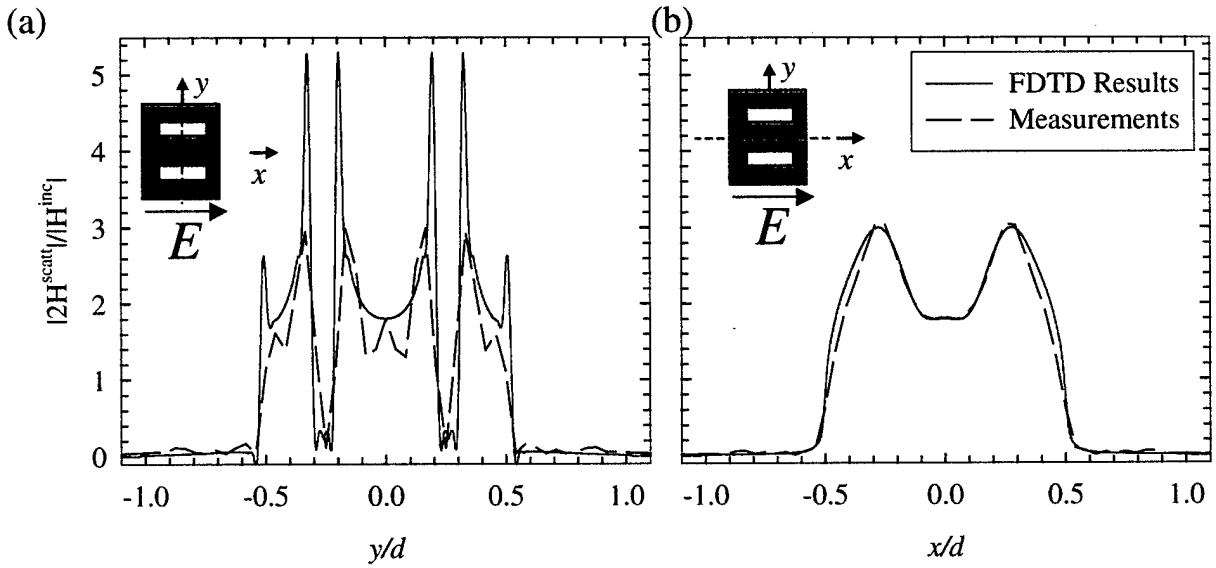

Figure 6-25. Comparison of the measured and predicted current distributions for the slotted plate. Incident electric field is parallel to the slots. Cross sections of the current in the *y* direction (a) and *x* direction (b) are shown. The measurements were normalized by a factor of 0.928. (Spatial window size $w = 1.7d$ x $1.7d$, $\alpha = 0.7$, $k_{xcut}/k_0 = 4$ and $k_{ycut}/k_0 = 3$)

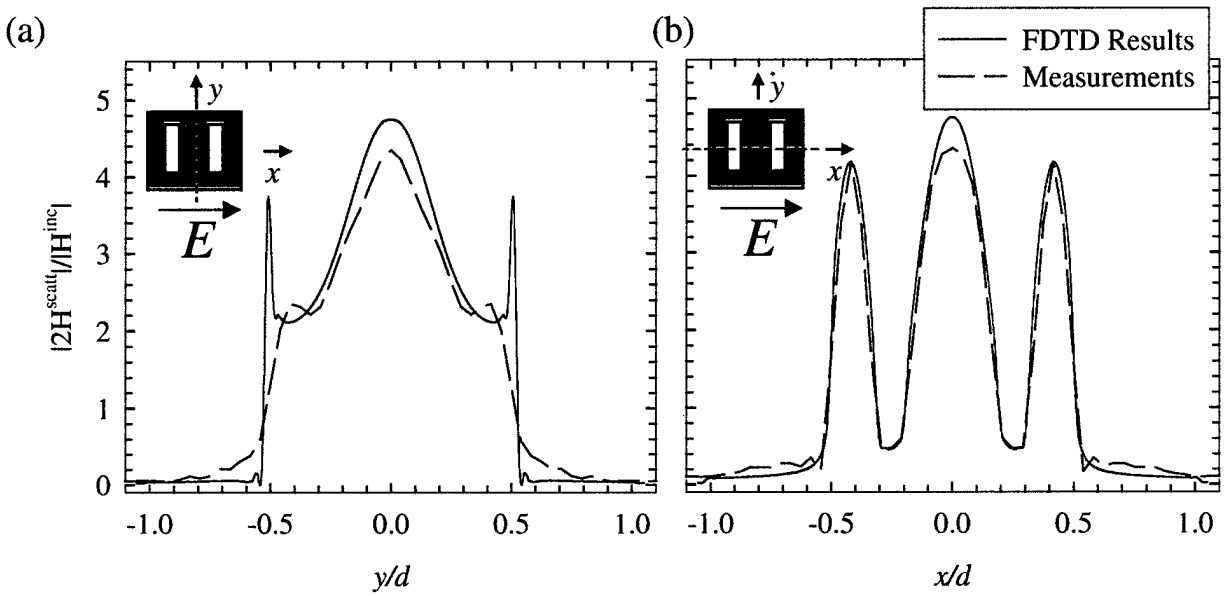

Figure 6-26. Comparison of the measured and predicted current distributions for the slotted plated. Incident electric field is normal to the slots Cross sections of the current in the *y* direction (a) and *x* direction (b) are shown. (Spatial window size $w = 1.5d$ x $1.5d$, $\alpha = 0.7$, $k_{xcut}/k_0 = 3$ and $k_{ycut}/k_0 = 2.5$)

7 Local Back-Propagation

The full back-propagation technique heretofore discussed utilized all the magnetic field data on the measurement surface to obtain the current on the target. This surface extends beyond the edges of the target, and thus, a large number of measurements are required for large targets. As a result, measurement times may prove impractical for large targets. A more efficient approach, presented in this section, is to use a "local" method, as depicted in Figure 7-1, for measuring the currents on a plate. In this figure, the scan plane is a distance s from the flat-surface target (a metal plate) and the magnetic field is sampled on the scan plane at a sample spacing of d. The local probe method uses a small number of measurements over a small portion of the entire scan plane, indicated by a dashed square in the figure, to determine the current at a point centered beneath the local probe. As a result, the measurements need be performed only where the current is desired. Hence, the measurement time is shorter when the current is needed only over a small area. The surface current value is available immediately without post processing.

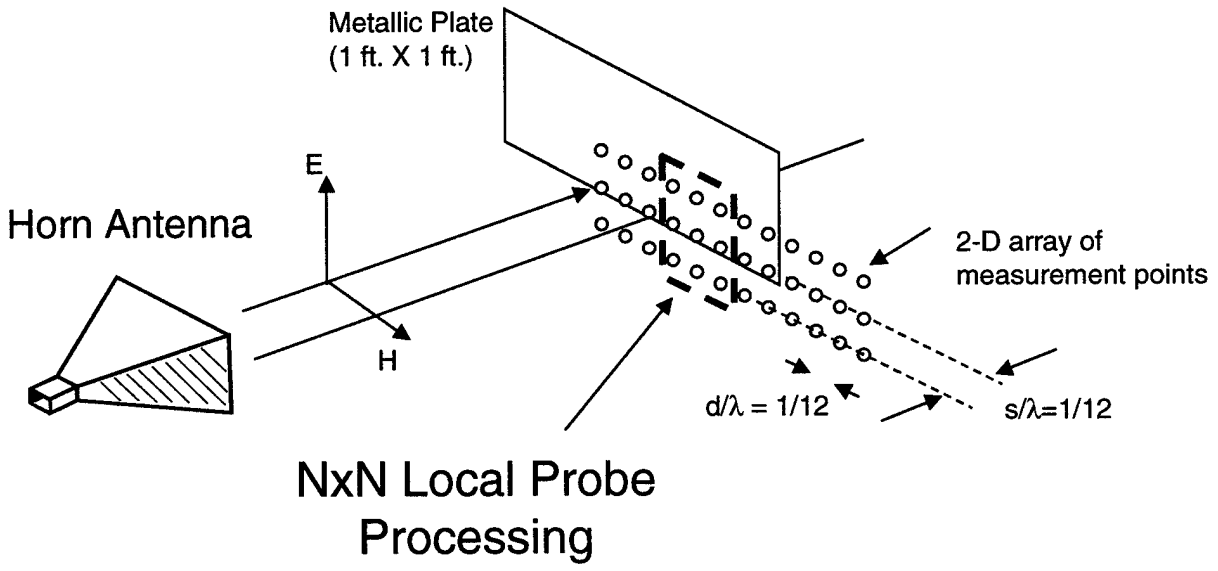

Figure 7-1. Local probe measurement configuration.

7.1 Theory

The approach can be readily understood by considering the behavior of the magnetic field that is scattered from the surface, or, equivalently, generated by the surface current. If the magnetic field is measured at the surface, i.e., $s = 0$, only the magnetic field at the same location as the

current is required to compute it. This fact can be readily seen from the boundary condition for the tangential magnetic field on a flat conductor. As the scan plane is moved away from the surface, the magnetic field spreads out over a greater area, and a larger scan surface is required to capture the significant portion of the field and reconstruct the current at the conductor. As long as the scan plane is close to the surface, a small scan area will suffice to capture the significant portion of the scattered magnetic field necessary for reconstructing the current at a point centered below the scan plane. This small scan plane is employed in the local probe method. With this background, the local probe approach can be readily derived from the full back-propagation technique.

To relate the local probe to the full back-propagation technique, consider the 2-D problem geometry in Figure 7-2, where a line source excites the currents on a conductor of finite width, and the scattered magnetic field is sampled along a line a distance s in front of the plate as shown. For this case, the local probe will cover a small portion of the scan line and can be expressed as

$$J_{sy}(i\Delta x) = \sum_{n=-N_w}^{N_w} w_n H_x^{meas}(i-n), \tag{7.1}$$

where the magnetic field is at the measurement line a distance, s, from the current, w_n are the weights, the total number of weights is $2N_w+1$, and J_{sy} is the current. The number of weights forming the local probe $(2N_w+1)$ is always chosen to be odd, and the probe is centered above the particular point at which the current is to be reconstructed. To compare this representation with the full back-propagation method, consider the matrix form of (1) for computing the current over the whole line simultaneously, which is

$$J_{sy_{N-NW+1x1}} = W_{N-NW+1xN} H^{meas}_{x_{Nx1}} \tag{7.2}$$

where W is a matrix of $N-N_w+1$ local probes used to reconstruct the current at $N-N_w+1$ points. The magnetic field is sampled over N points, but due to the local probe width of $2N_w+1$, the maximum number of current samples that can be reconstructed is $N-N_w+1$.

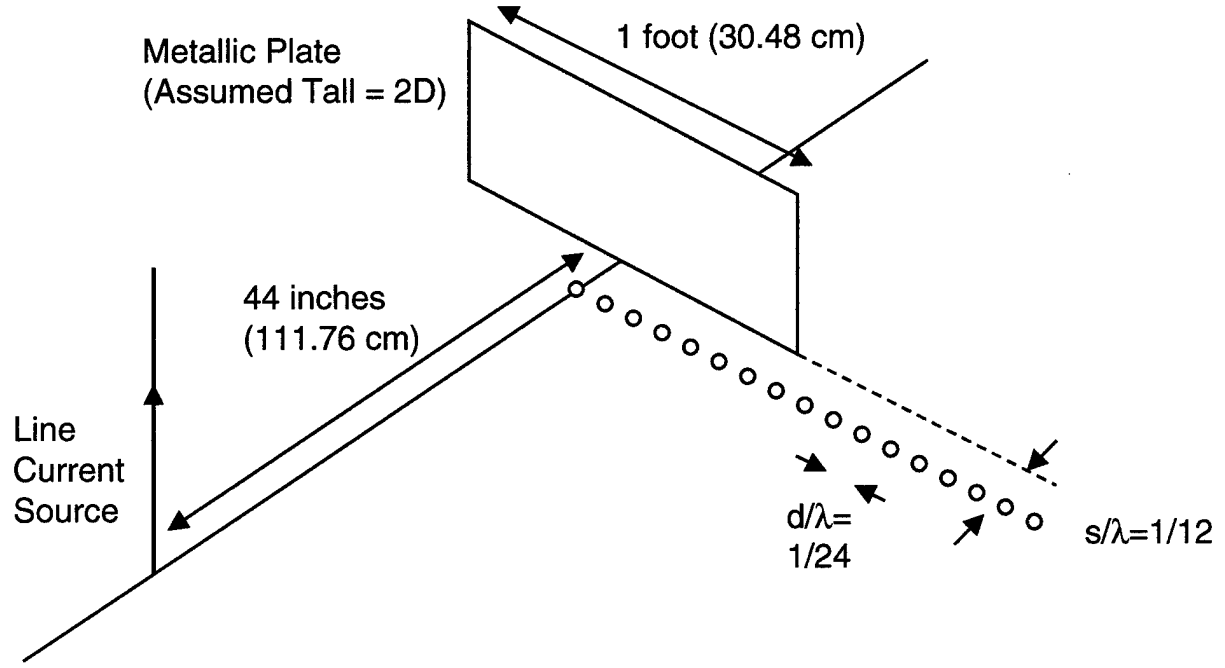

Figure 7-2. Two dimensional geometry, similar to actual measurement configuration, for studying local probe.

For the 2-D case, where the scan plane becomes a scan line, the local probe matrix, W, is a sparse, diagonally dominant matrix with the central local probe weight falling on the main diagonal. The weights on either side of the center weight fall on the next closest side diagonals, and the rest of the matrix elements are zero. For the 3-D case, the matrix is less sparse due to the weights being distributed over a small area instead of a line. The rest of this discussion will focus on the simpler, 2-D case in Figure 7-2, but the principles readily generalize to the 3-D case.

For comparison with the local probe back-propagation technique, the full back-propagation technique can be expressed in matrix form as

$$J_{syNx1} = \left[FT^{-1}\right]_{NxN} \begin{bmatrix} \text{filter}(k_x)\cdot e^{jk_z s} & 0 \\ 0 & \ddots \end{bmatrix}_{NxN} \left[FT\right]_{NxN} H^{meas}_{xNx1}, \qquad (7.3)$$

where FT is forward Fourier Transform, FT^{-1} is the inverse Fourier Transform, filter(k_x) is the spectral domain filter, $e^{jk_z s}$ is the back-propagation exponential, k_z is the propagation constant and s is the distance from the scan plan to the surface of the plate. For the two techniques to be approximately equivalent we need

$$W_{N-NW+1xN} \approx \left[FT^{-1}\right]_{N-NW+1xN} \begin{bmatrix} filter(k_x)\cdot e^{jk_z s} & 0 \\ 0 & \ddots \end{bmatrix}_{NxN} [FT]_{NxN} . \qquad (7.4)$$

This equivalence depends mainly on the diagonal dominance of the full back-propagation matrix, which largely depends upon s. The condition where the two expressions are exactly equivalent is the case where $s = 0$. For this distance, both matrices are a diagonal of twos, assuming the surface current is twice the scattered magnetic field value.

Next, consider the case for $s = 0.1\ \lambda$. The image of the magnitude of the full back-propagation matrix is shown in Figure 7-3, and the plot of the central row or column is shown in Figure 7-4. Both figures clearly indicate that for this distance, s, the full back-propagation matrix is diagonally dominant. Therefore, most of the contribution of the magnetic field to the current is from the field localized to a small scan line above each current sample. As s increases, Figure 7-5, which is a graph of the central row or column of this matrix, shows the matrix becomes less diagonally dominant. Arbitrarily considering weights with values of 0.5 and above as necessary but not necessarily sufficient for the local probe back-propagation technique, Figure 7-6 shows that the minimum number of weights required for the local probe increases with s since the magnetic field distribution spreads out with greater s. Consequently, the local probe must be applied over a greater area/line with increasing s. These results demonstrate the full back-propagation matrix is diagonally dominant as long as s is small, and hence, for small s it can be approximated with a relatively small set of local probe weights.

If $s = 0$, the weights for the local probe can be estimated exactly from a row/column of the full back-propagation technique. However, more practical distances of $s \approx 0.1\lambda$ require a methodology for determining the local probe weights. If the local probe weights are chosen directly from a truncated version of the full back-propagation matrix for these distances, the resulting current reconstruction was found to be poor, because the full back-propagation matrix elements work together in such a way that the off diagonal matrix elements contribute a significant amount even at relatively small distances.

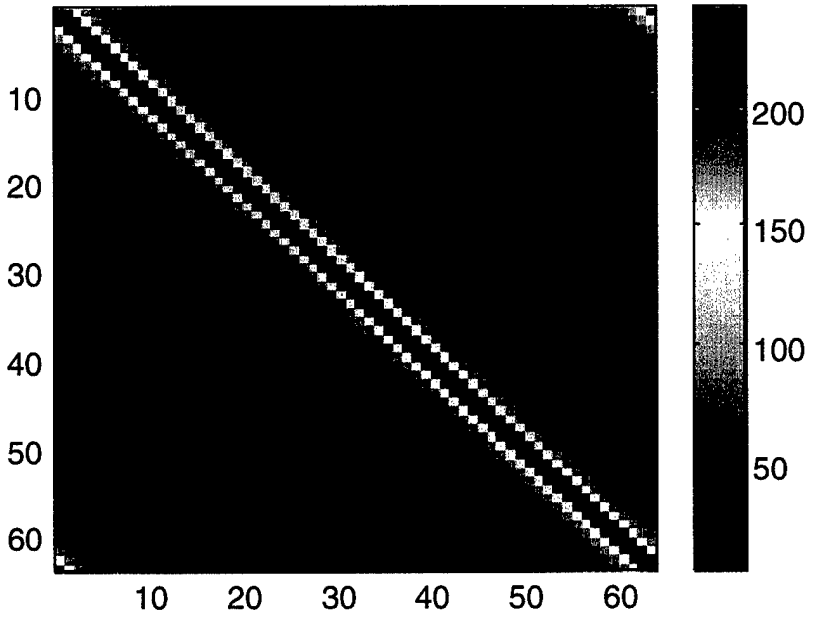

Figure 7-3. Image of magnitude of back-propagation matrix for $s = 0.1\ \lambda$.

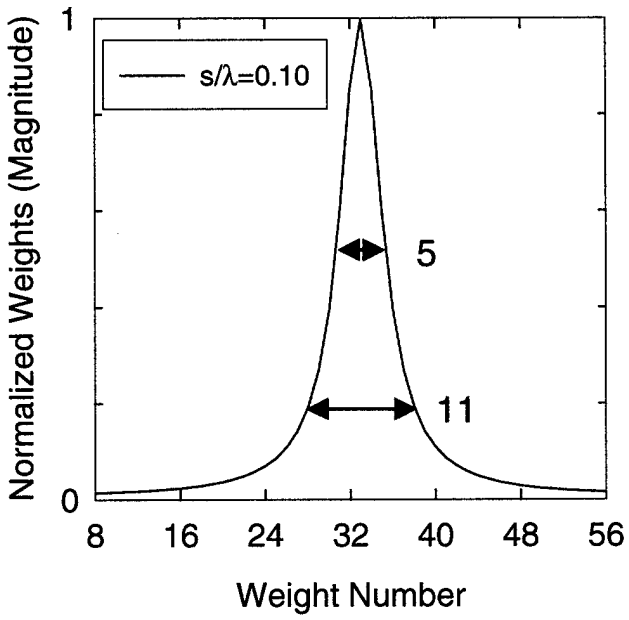

Figure 7-4. Cross-section through matrix in Fig. 1.

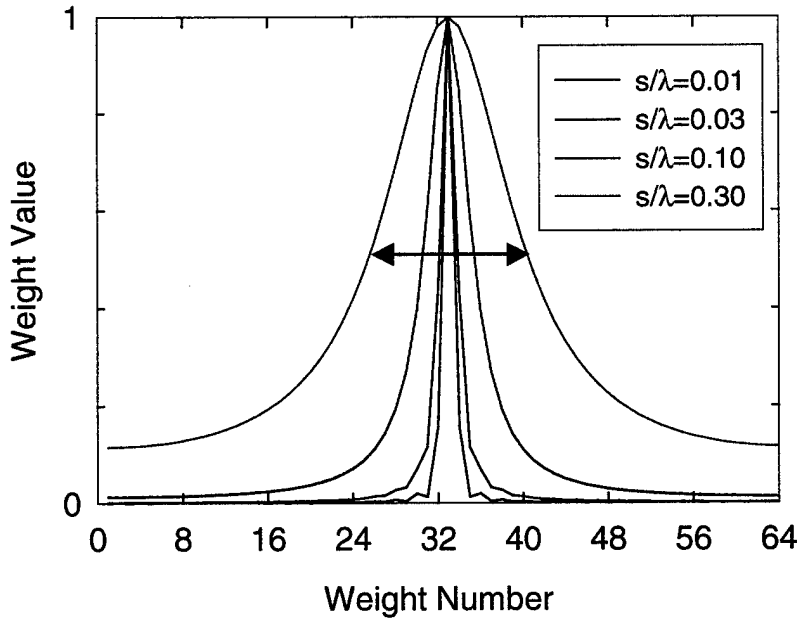

Figure 7-5. Weight value variation with distance, *s*.

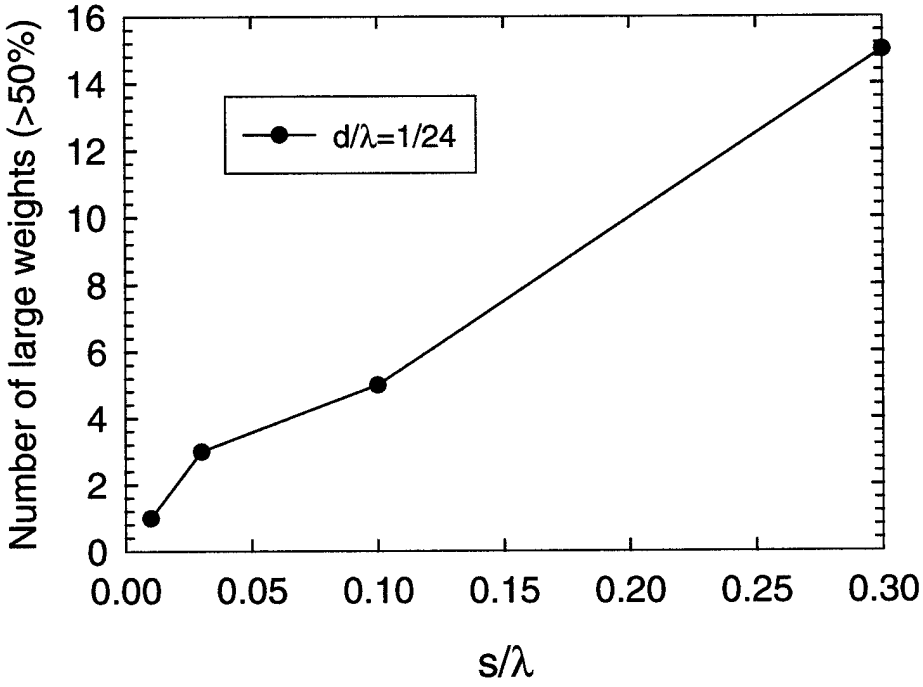

Figure 7-6. Number of weights per distance, *s*, that are greater than a weight value of 0.5 in Figure 7-5.

In this work a novel technique that uses a least squares fit procedure is employed to obtain the weights. The approach is depicted in Figure 7-7. An over-constrained configuration is used to form the matrix equation that is solved with the least-squares method for the weight values. The matrix is filled row by row, where a row consists of $2N_w+1$ elements. Each row consists of the magnetic field at sample points on the scan line due to an ideal dipole source. To form independent rows, either the dipole location is shifted from row to row and the magnetic field observation points remain fixed, or visa versa. The excitation vector for the matrix equation is a set of zeros with a unit source located at the center, assuming the center of the vector corresponds to the location where the current is to be reconstructed.

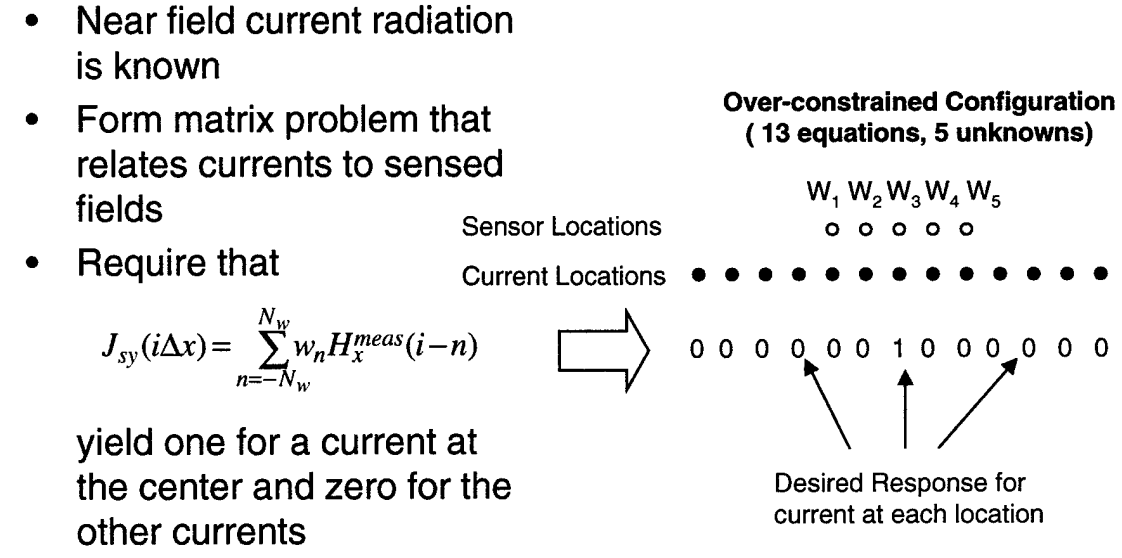

Figure 7-7. Weight Computation.

7.2 Numerical Study of Local Probe

To study the effectiveness of the local probe consider the two-dimensional problem geometry shown in Figure 7-2. For this study the source is a line current which is 111.76 cm (44 inches) in front of a 30.48 cm wide (1 foot) flat conducting plate. (The plate and line source are infinitely tall for the 2-D problem.) The scan line is s = 1/12 λ in front of the conducting plate, and the measurement points are d = 1/24 λ apart. A line of 9 weights was generated with an over constrained matrix constructed from 49 sample points. The real and imaginary parts of the weights are shown in Figure 7-8. The weights oscillate in sign between the probe locations in a manner similar to the edge filters used in image processing.

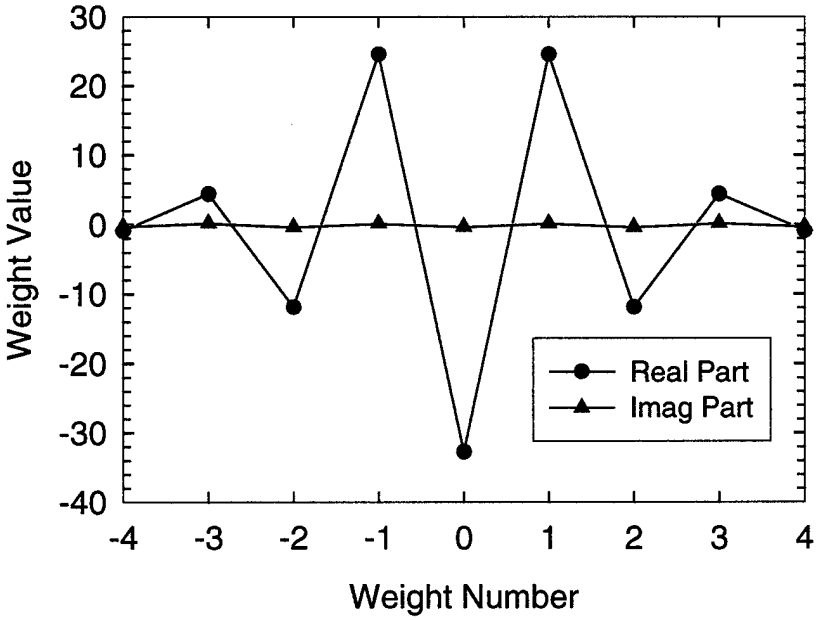

Figure 7-8. Set of 9 weights for local probe in 1-D study.

The geometry in Figure 7-2 is modeled using FDTD to generate the magnetic fields at the scan line points and to generate the "ideal" surface current with which the reconstructed current will be compared. The reconstructed current is obtained by applying the local probe processing, i.e., (7.1), to the FDTD generated data at the scan line.

The comparison of the FDTD data with the local probe reconstruction of the current is shown in Figure 7-9. These results are presented in dB to magnify the behavior at the edges of the plate. The back-propagated results agree well with the FDTD computations (labeled plate data in the figure) for the majority of the current distribution. The results also agree well in depicting the near singular nature of the current at the edges. The most disagreement occurs at the low field regions near and away from the plate edges.

The places at which the local probe has trouble are slightly beyond the edges of the plate. The local probe result transitions from that of the current distribution at the plate to the magnetic field distribution at the scan line away from the plate. If the local probe weights were placed closer together, the number of weights increased, and the local probe stencil size extended, this effect would probably be reduced. However, this solution is at the expense of a larger local probe. An optimal solution to this problem requires further study. It is possible that more development of the technique for determining the weights, i.e., their values as well as the number of weights and the weight spacing, will reduce this error.

7.3 Measurements

The 3-D measurement configuration used for testing the local probe concept is shown in Figure 7-1. The actual measured data that was employed in the full back-propagation method is also employed here. In this case, only a localized set of magnetic field measurements is used to reconstruct the current centered below the local probe, and then the probe is shifted horizontally and vertically to reconstruct the current over the entire plate.

An image of the weights is shown in Figure 7-10. The local probe was formed from a 9x9 set of weights (81 total) spaced 1/12 λ apart, and computed for a distance s = 1/12 λ. The current reconstruction using the local probe with this weight set is compared with the current computed using FDTD in Figure 7-11. Cross sections of these current distributions are shown in Figure 7-12. Before using the local probe, the density of the measured data was increased from 1/12 λ to 1/24 λ by linear interpolation to help smooth out the results. The comparison of the numerical results with the local probe back-propagated results shows the local probe technique worked well. Since the FDTD computations are based on a smaller grid than the local probe, it can resolve the edge behavior of the current better.

The surface current for the plate with two apertures was also reconstructed with the local probe processing of the interpolated measured data and compared with data obtained with FDTD. The results are shown in Figure 7-13. The comparison shows reasonable agreement in overall form. Two differences in the results are the saw-toothed curve in the x/d cross section of the measured data and the slightly lower amplitude of the measured data with respect to the FDTD data.

7.4 Conclusions

This work demonstrates that the local probe concept can be effective for localized surface current measurements in that good agreement was obtained with data from FDTD computations. This technique requires less data and time than the full back-propagation approach for small regions of current. The artifacts that occur with the technique need further study in order to reduce or eliminate them. For example, other weight generation schemes can be employed to provide weight sets with different characteristics.

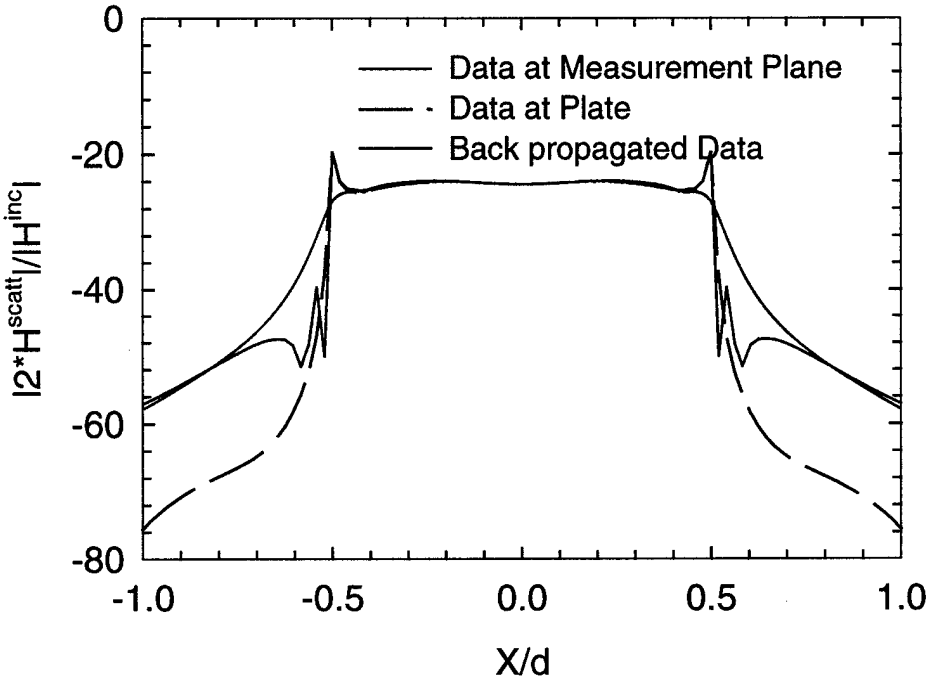

Figure 7-9. Local probe back-propagated FDTD data compared with FDTD data at the plate and at the measurement line.

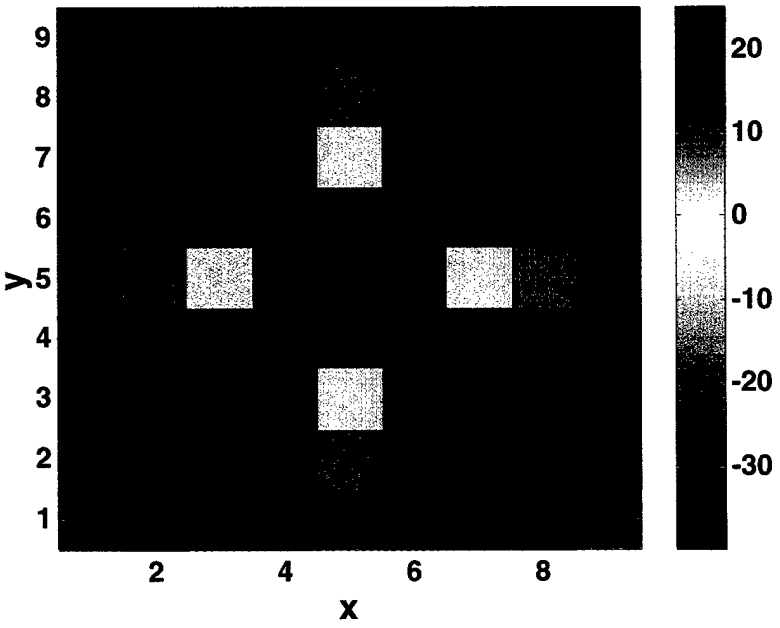

Figure 7-10. Image of weights magnitude (dB) used for the local probe. (9x9 Weights, 39x39 Test Points, d = 1/12 λ, s = 1/12 λ)

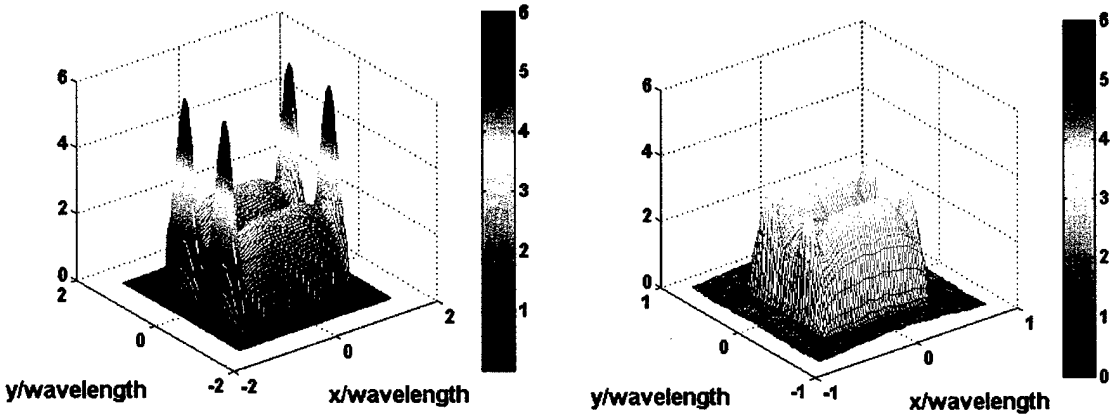

Figure 7-11. Surface current computed with FDTD and compared to that reconstructed using the local probe. The FDTD results are based on a grid of l/48 λ, and the local probe results are based on local probe weights spaced 1/12 λ.

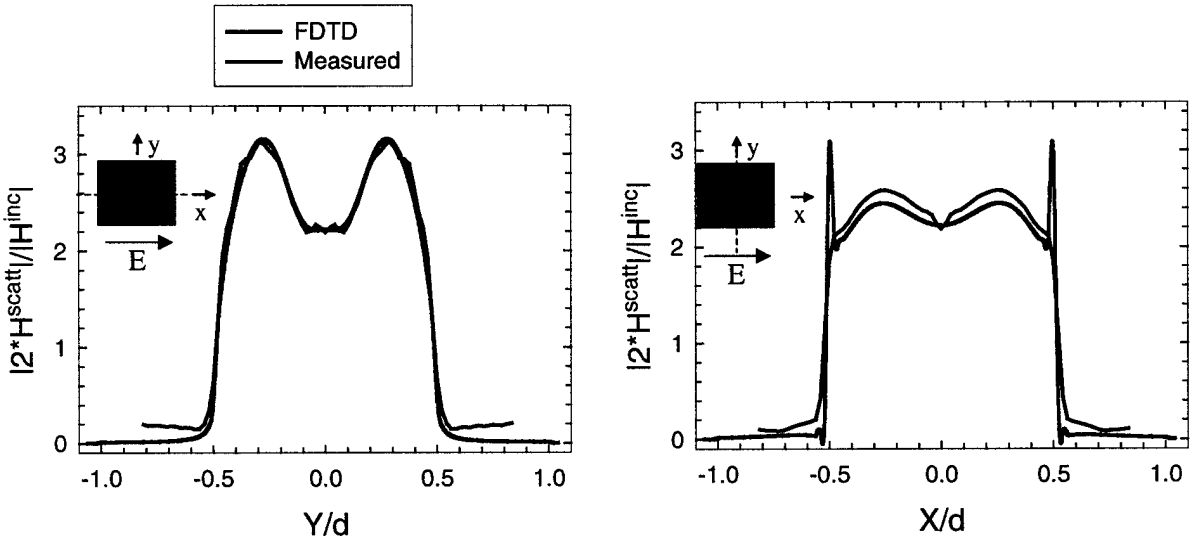

Figure 7-12. Cross sections of current in Figure 7-11.

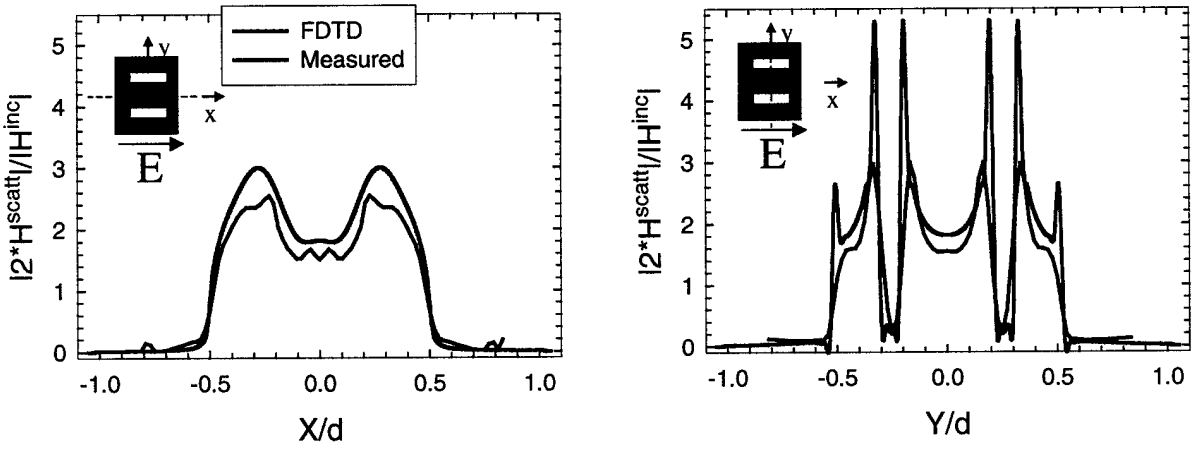

Figure 7-13. Cross sections of surface current for a plate with two apertures. The local probe results are based on local probe weights spaced 1/12 λ.

8 FSS and Pyramid

8.1 Introduction

The use of the local probe back-propagation technique for reconstructing surface currents or fields for high frequency applications was tested on a 4x4 FSS of holes. The FSS was located in a face of a metal pyramid covered by absorber on all but the FSS side. The magnetic fields were measured on a scan plane 0.5 inches in front of the FSS surface and then back-propagated with the local probe. The results are compared with numerical results obtained with FDTD. The $\omega - \beta$ diagrams for the scattering from this structure are also included.

8.2 Geometry

The FDTD model of the pyramid with the FSS on one face and absorber covering all four other faces is shown in Figure 8-1. Each edge length of the pyramid is 2 feet. The FSS consists of 4x4 holes of 2.223 cm (7/8 inch) diameter that are spaced 5 cm apart in the front metal plate of the pyramid in the figure. The reflections from the absorbing material are assumed to be approximately 20 dB below the incident signal. The pyramid FSS face is illuminated with a standard gain horn at an incident angle of 45 degrees with respect to the normal (z) as shown in the top view in Figure 8-2. The pyramid is tilted such that the z coordinate axis is perpendicular to the surface of the FSS. The incident field is polarized with the electric field in the y coordinate direction as shown in Fig. 2. The tangential magnetic field (H_x) is measured with the loop probe 0.5 inches in front of, and parallel to, the FSS surface.

8.3 Numerical Simulation and Measured Results

The numerical and measured results will be discussed next. For both cases the sample spacing was 0.5 cm. Because this sample spacing makes it difficult to see the FSS features, all of the data were interpolated before plotting and before back-propagating with the local probe. The $\omega - \beta$ diagrams were also computed with the interpolated data. Linear interpolation was used to add points among the original field samples to reduce the field sample spacing to 0.25 cm. This interpolation greatly improved the visualizations, but it does not make the actual data more accurate.

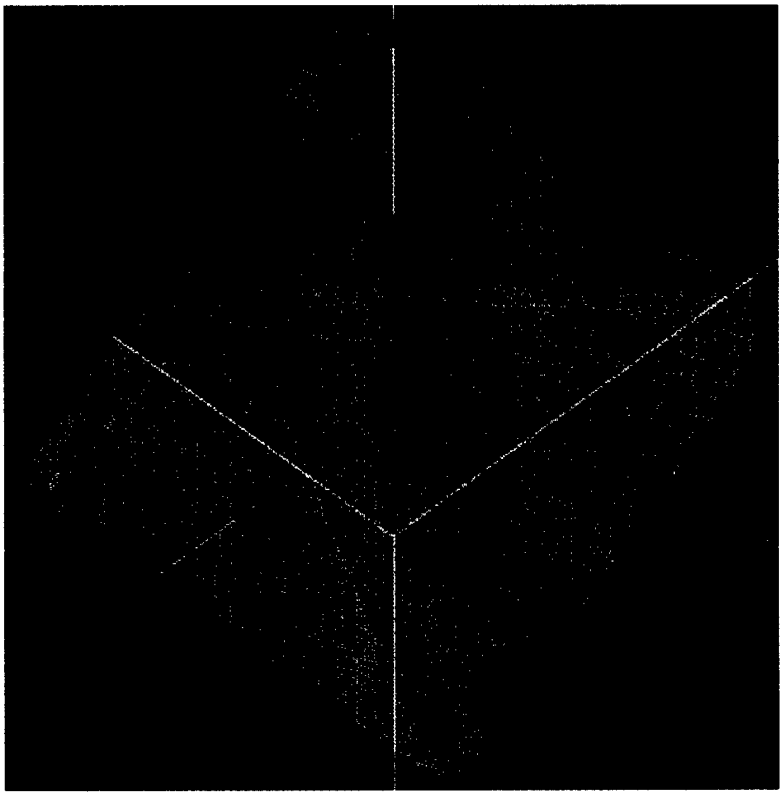

Figure 8-1. FDTD model of FSS and pyramid with absorber.

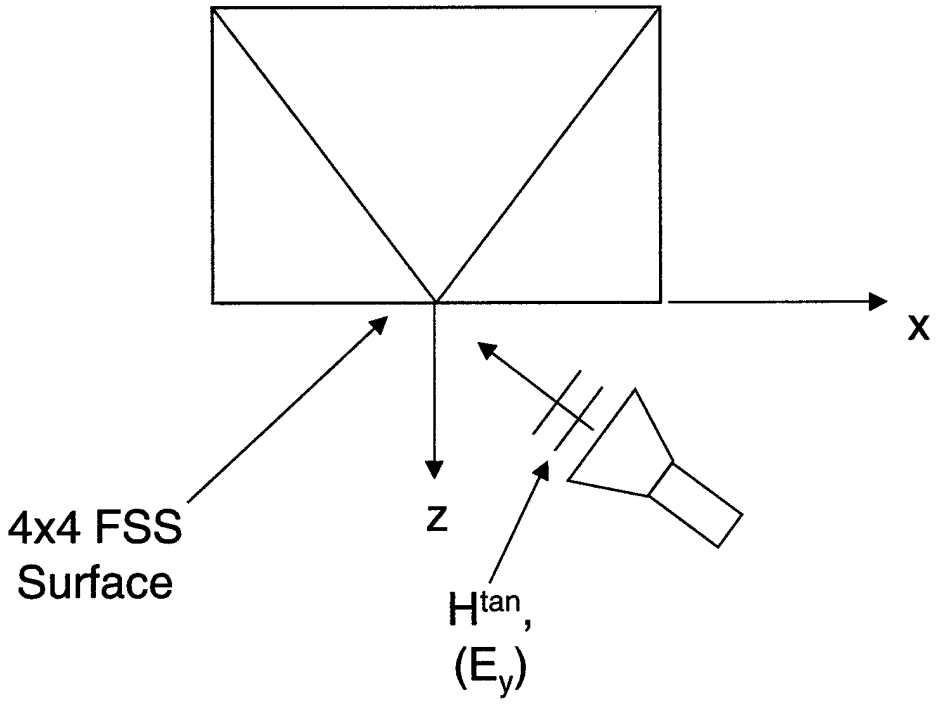

Figure 8-2. Diagram of horn illumination of FSS on pyramid.

8.4 Numerical Simulation

The discretized model of the pyramid and FSS is shown in Figure 8-1, with the holes for the FSS sketched in for emphasis. The actual discretization of the FSS is shown in Figure 8-3. (The figure has a visualization artifact that makes the grid appear to be missing horizontal lines in the grid.) The FDTD technique was used to compute the scattered magnetic fields on the scan plane and on the FSS surface. The horn illumination was approximated with a plane wave due to memory and CPU limitations. The FDTD unit cell size is 0.5 cm per edge. This discretization resulted in slight shifts in the location of the scan plane as well as the location of the observation plane at the FSS surface. The scan plane in the numerical simulation was 2.5 cells or approximately 1.25 cm (0.4921 inches) away from the FSS surface. The observation field at the surface was actually 0.5 cells or 0.25 cm away from the surface. In addition, the discretization resulted in cross-shaped instead of circular holes as shown in Figure 8-3.

The absorbing material parameters were not known, so a three-layer material was designed using a simple multi-layer transmission/reflection analysis program as described in [28]. The absorber consisted of three 1 cm thick layers with different permittivities and conductivities as shown in the Table 1. The absorber was designed for normal incidence, and its response is shown in Figure 8-4. This absorber provides approximately –25 dB of loss at 10 GHz.

Table 1. Absorber Material Parameters

Layer	t (cm)	ε_r (F/m)	s (S/m)
1 (Nearest to PEC)	1	3.0	1.0
2	1	2.0	0.4
3	1	1.0	0.3

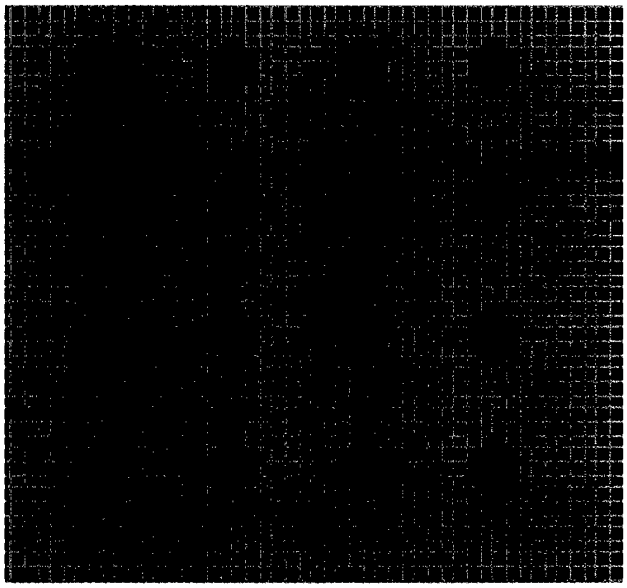

Figure 8-3. Close up view of FSS in FDTD model showing staircase approximation to the round apertures.

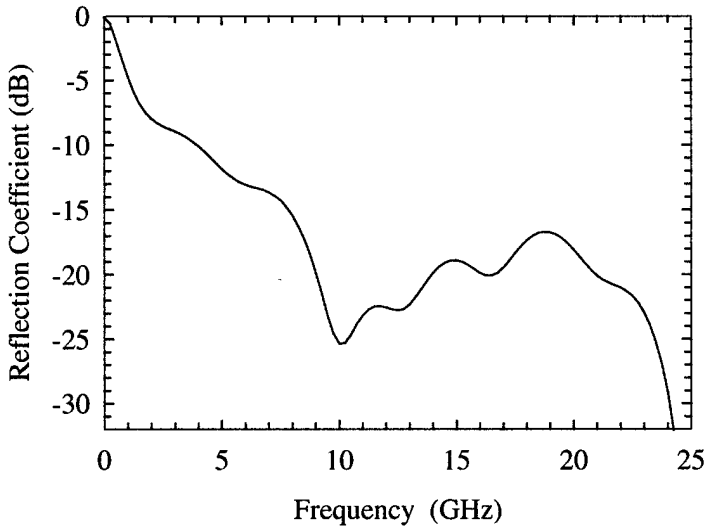

Figure 8-4. Reflection coefficient for 3 layer absorber design.

Images of the scattered magnetic field at 1 GHz obtained with the FDTD simulations are shown in Figure 8-5 - Figure 8-7. The axes units are expressed in terms of the FSS periodic cell

size, T, of 5 cm. The x and y axes directions are shown in Figure 8-2. The incident wave front is propagating in the $-x$ direction.

The scattered magnetic field at the scan plane is shown in Figure 8-5, and the scattered magnetic field at the FSS surface is shown in Figure 8-6. Actually, the field is 2.5 mm in front of the surface due to the cell size used for the FDTD grid. This distance is negligible at the frequencies of interest and is negligible for the majority of the spectral content observed in the $\omega - \beta$ diagrams that follow. (The distance is 1/20 λ or less for spectral components below k_x = 125.) Both images show small spots corresponding to the holes in the FSS, and the phase transitions along the direction of propagation. At the scan plane, the intensity of the spots varies across the surface along the direction of propagation of the incident wave. The field magnitude and phase transitions are sharper at the FSS surface than at the scan plane, and the field magnitude is more visually uniform at the surface. In both figures the FSS holes produced oval shaped scattered field distributions with smaller field oscillations near the hole edges.

A local probe was used to back-propagate this field from the distance s=1.27 cm (0.492 inches). The local probe consisted of a 5x5 square array of weights spaced 1 cm apart. The resultant surface fields are shown in Figure 8-7. Comparing these fields with the FDTD data at the FSS surface in Figure 8-6 shows the results are in good agreement in both magnitude and phase. Due to the lower sampling density of the local probe (2.2 samples per hole diameter), the local probe back-propagated results are not as sharp as those at the FSS surface.

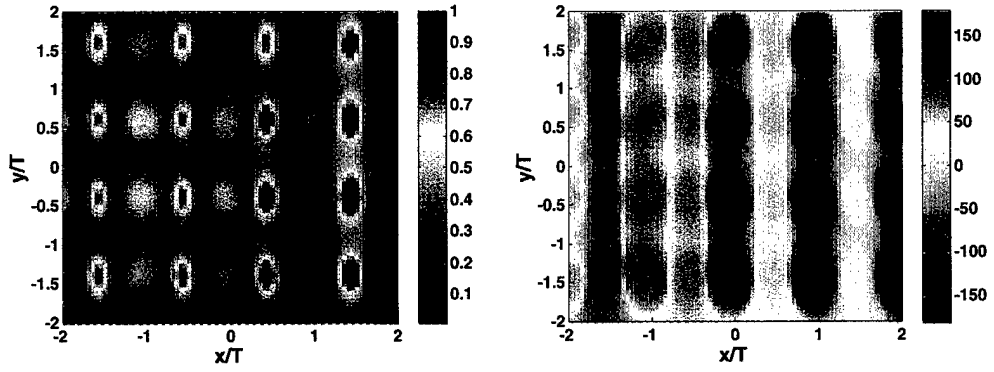

Figure 8-5. Normalized magnitude and phase of the FDTD computed scattered magnetic field at the scan plane at 1 GHz. (Linear magnitude and phase in degrees are shown.)

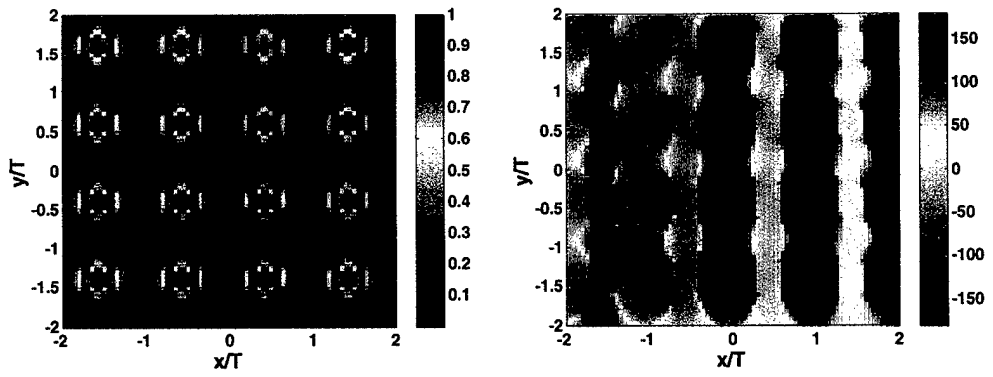

Figure 8-6. Normalized magnitude and phase of the FDTD computed scattered magnetic field at the FSS surface at 1 GHz. (Actually 2.5 mm from surface. Linear magnitude and phase in degrees are shown.)

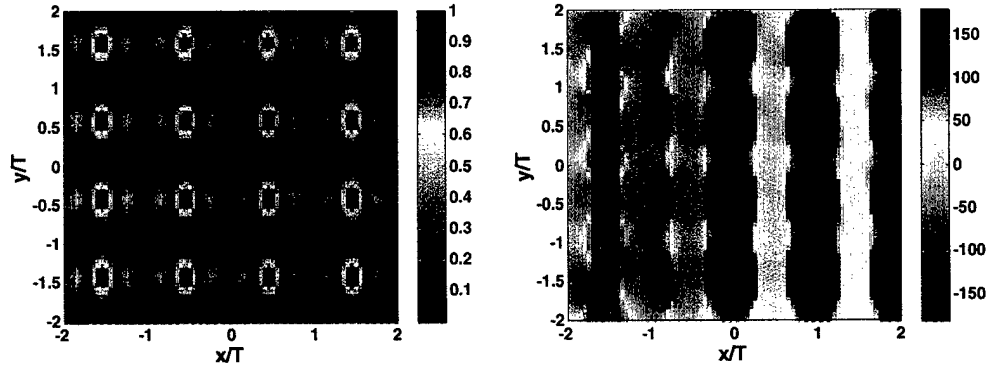

Figure 8-7. Local probe back-propagated results of the FDTD data at 1 GHz. Back-propagated from scan plane (s = 0.492 inches) to FSS surface (s = 0 inches). (Linear magnitude and phase in degrees are shown.)

8.5 Measurements

Images of the scattered magnetic field at 1 GHz obtained from the measurements are shown in Figure 8-8 and Figure 8-9. The magnitude and phase of the measured scattered magnetic field at the scan plane for 1 GHz is shown in Figure 8-8. Comparing these results with the FDTD data at the scan plane in Figure 8-5 shows that both results have similar features; namely, oval spots with varying intensities where the array holes are, and variations in phase along the direction of propagation.

These measured fields were back-propagated with a local probe consisting of a 5x5 square array of weights spaced 1 cm apart. The surface fields reconstructed with this local probe are shown in Figure 8-9. The area of the oval spots in the magnitude image of the scattered magnetic field has

become smaller and the phase transitions sharper than in the scattered magnetic field at the scan plane. Comparing these results with the computed results at the FSS surface in Figure 8-6, shows the local probe back-propagated measured data has characteristics similar to the FDTD data at the FSS surface. The oval spots in the magnitude images are similar in size and shape, although the FDTD results are more uniform in intensity, and the phase transitions both have sharply defined strips of color at x/T = -1.5, -0.5, 0.5 and 1.5. The local probe back-propagated measured results indicate the presence of the 4x4 FSS as seen by this particular component of the magnetic field. A more complete picture could be obtained by back-propagating both magnetic field components.

In conclusion, these comparisons indicate the measured and computed results are in basic agreement. Both show the presence of the FSS elements with oval-shaped regions in the images, and both show a phase transition along the direction of propagation. Most of the errors in the results are attributed to the relatively low sampling density of the local probe (2.22 samples per FSS hole diameter). Other errors, such as the numerical errors, can be attributed to the staircasing approximation used in FDTD to model the FSS and pyramid and the use of an incident plane wave to model the horn illumination. In spite of the relatively low sampling densities employed for this example, the images are useful for indicating the presence of the 4x4 FSS and location of the holes.

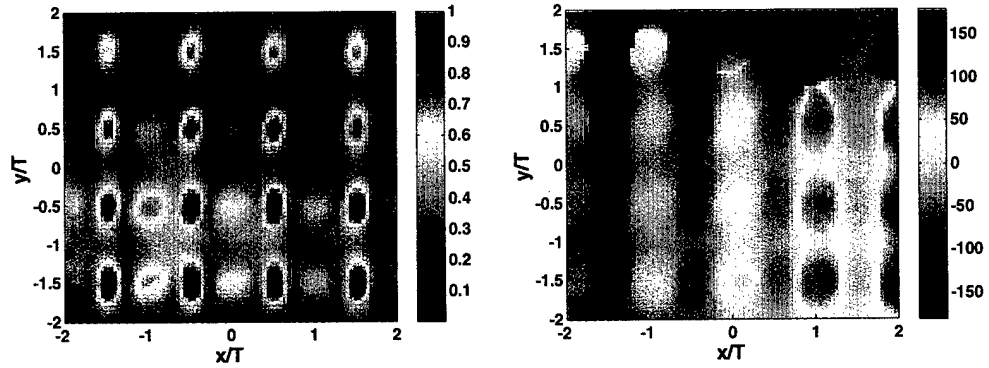

Figure 8-8. Measured data at the scan plane for 1 GHz. (Linear magnitude and phase in degrees are shown.)

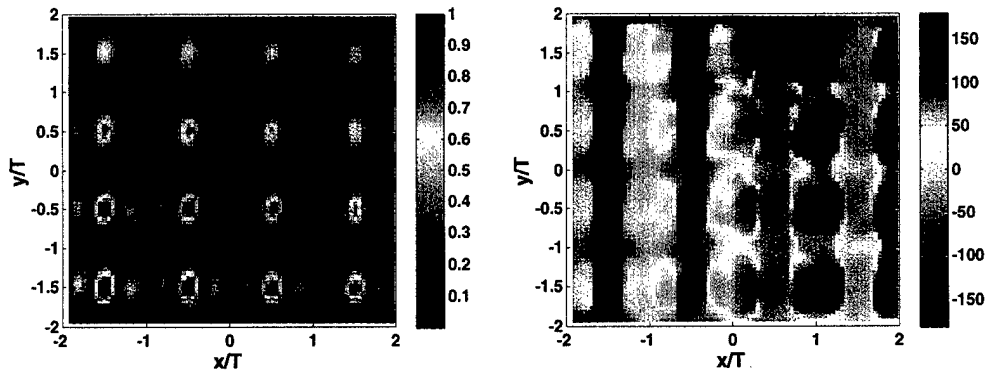

Figure 8-9. Local probe back-propagation of measured data to FSS surface at 1 GHz. (Linear magnitude and phase in degrees are shown.)

8.6 Scattered Magnetic Field Spectrum

8.6.1 Dipole Antenna Array

The scattered magnetic field spectrum at both the scan plane and FSS surface will be studied using $\omega - \beta$ diagrams. To gain understanding for interpreting the results, first consider a $2N \times 2N$ array of ideal point dipoles with an element spacing of d and each element excited with a linear phase shift in x causing the main beam of the array to be directed at 45 degrees with respect to the normal (z) to the array surface. (See Figure 8-10.) This problem approximates the FSS illuminated by a plane wave at an incident angle of 45 degrees, and therefore, it can yield some insight into the analysis for the FSS. The normalized radiated magnetic field at a surface of $s = 0.5$ inches is shown in Figure 8-11 for the 4x4 dipole array at 1 GHz. Comparing it with the normalized scattered magnetic field data at the scan plane for the FSS (Figure 8-5 and Figure 8-8) shows the fields are similar, indicating the point dipole array is an acceptable approximation to the FSS as a starting point for gaining insight into the magnetic field behavior of the FSS.

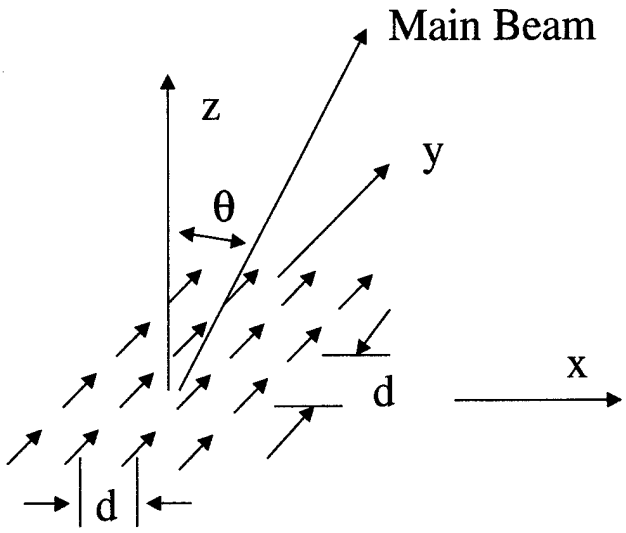

Figure 8-10. Two-dimensional dipole array.

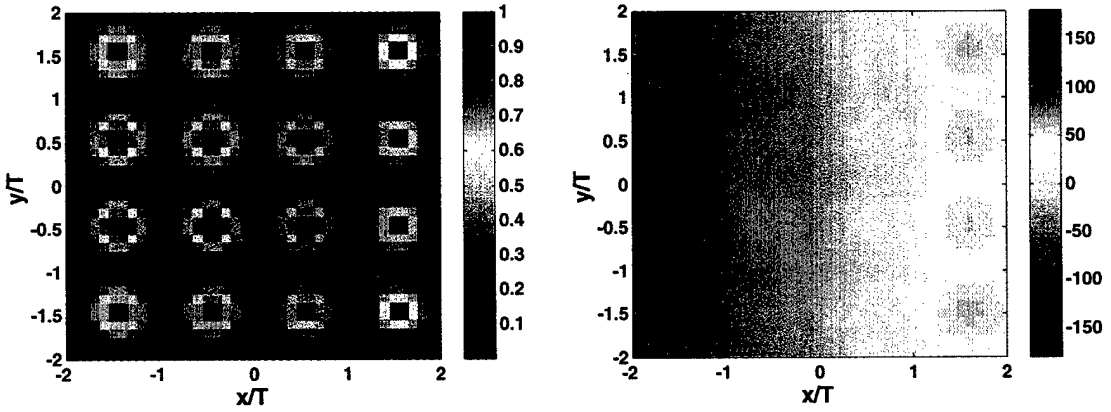

Figure 8-11. Normalized radiated magnetic field at the scan plane of the dipole array at 1 GHz. (Linear magnitude and phase in degrees are shown.)

In the space domain, the magnetic field from the point dipole array can be written as

$$H(x,y,z)=\left[\sum_{m=-\infty}^{\infty}\sum_{n=-\infty}^{\infty} g(x-nd,y-md,z)\cdot e^{jndk_0\sin\theta}\cdot \text{Pulse}(nd,md)\right] \qquad (8.1)$$

where g() is the point dipole pattern function for the magnetic field component, $e^{jndk_0\sin\theta}$ is the excitation of each dipole element, and Pulse() is unity if the dipole is one of the $2N$ x $2N$ dipoles, or zero otherwise. Eq. (1) is effectively a discrete convolution. The Fourier transform of (1) for a given z plane is

$$\tilde{H}\left(k_x,k_y,z\right)=\tilde{g}\left(k_x,k_y,z\right)\cdot\sum_{n=-N}^{N-1}e^{jnd\left(k_x+k_0\sin\theta\right)}\sum_{m=-N}^{N-1}e^{jk_y md}, \tag{8.2}$$

which yields

$$\tilde{H}\left(k_x,k_y,z\right)=\tilde{g}\left(k_x,k_y,z\right)\frac{1-e^{j2Nd\left(k_x+k_0\sin\theta\right)}}{1-e^{jd\left(k_x+k_0\sin\theta\right)}}\frac{1-e^{j2Nk_yd}}{1-e^{jk_yd}}e^{-jNd\left(k_x+k_0\sin\theta\right)}e^{-jNdk_y}, \tag{8.3}$$

Simplifying this gives

$$\tilde{H}\left(k_x,k_y,z\right)=\tilde{g}\left(k_x,k_y,z\right)\frac{\sin\left(Nd\left(k_x+k_0\sin\theta\right)\right)}{\sin\left(d\left(k_x+k_0\sin\theta\right)/2\right)}\frac{\sin\left(Nk_yd\right)}{\sin\left(dk_y/2\right)}e^{-jk_yd/2}e^{-j\left(k_x+k_0\sin\theta\right)d/2}. \tag{8.4}$$

Then, the $\omega-k_x$ diagram for the $k_y=0$ plane is given by taking the limit as $k_y\to 0$ of (8.5) which for the radian frequency ω and the velocity of light in free space c can be written as

$$\tilde{H}\left(k_x,z,\omega\right)=\tilde{g}\left(k_x,z,\omega\right)2N\frac{\sin\left(Nd\left(k_x+\frac{\omega}{c}\sin\theta\right)\right)}{\sin\left(d\left(k_x+\frac{\omega}{c}\sin\theta\right)/2\right)}e^{-j\left(k_x+\frac{\omega}{c}\sin\theta\right)d/2} \tag{8.6}$$

This result shows the magnetic field spectrum is that of a dipole element times an array factor. The array factor is similar to a periodically repeating Sinc function that has its nulls and peaks along the spectral axis at

$$k_x=\pm\frac{n\pi}{Nd}-\frac{2\pi}{c}\sin\left(\theta\right)f,\quad n=1,2,... \tag{8.7}$$

where f is frequency in Hz. Rewriting (6) to obtain the nulls and peaks along the frequency axis gives

$$f=\left(\pm\frac{n\pi}{Nd}-k_x\right)\frac{0.3}{2\pi\sin\theta}GHz\quad n=1,2,... \tag{8.8}$$

The peaks of the array factor occur when the denominator of (5) is zero, which occurs at

$$k_x = \pm\frac{2n\pi}{d} - \frac{2\pi f}{c}\sin\theta, \quad n = 1,2,.... \tag{8.9}$$

This equation can also be solved for frequency in terms of k_x. Since the peak locations are multiples of the null locations setting (8) equal to (6) gives the peak locations at

$$p = \pm 2Nn, \quad n = 1,2,... \tag{8.10}$$

where $2N$ is the number of elements per side of the array. The null-to-null widths of the peaks are $2\pi / Nd$. The null-to-null widths of the 'side lobes' are half of this or π / Nd. The magnetic field magnitude at the peaks of the array factor is given by

$$\tilde{H}(k_x, z, \omega) = \tilde{g}(k_x, z, \omega) 4N^2 \tag{8.11}$$

The $\omega - k_x$ diagram for a dipole array of the same size as the FSS array, i.e., $N = 2$ for a 4x4 array and d = 5 cm for 5 cm elements is shown in Figure 8-12. The array factor peaks and side lobes are tilted with respect to the k_x axis at an angle that is related to the 45-degree angle of the main beam with respect to the normal to the array. The nulls along the k_x axis occur at every 31.4 m^{-1} except when a peak occurs, which is at every $2N^{th}$ null or every 125.7 m^{-1}. The first null on the frequency axis occurs at 2.121 GHz. All of these parameters are seen in the $\omega - k_x$ diagram in Figure 8-12.

The $\omega - k_y$ diagram for the plane $k_x = 0$ is given by

$$\tilde{H}(z, k_y, \omega) = \tilde{g}(z, k_y, \omega) \frac{\sin\left(Nd\frac{\omega}{c}\sin\theta\right)}{\sin\left(d\frac{\omega}{c}\sin\theta/2\right)} \frac{\sin(Nk_y d)}{\sin(dk_y/2)} e^{-jk_y d/2} e^{-j\frac{\omega}{c}\sin\theta d/2} \tag{8.12}$$

The nulls along the spectral axis are given by

$$k_y = \frac{n\pi}{Nd}, \quad n = \pm 1, \pm 2, ... \tag{8.13}$$

and the nulls along the frequency axis are

$$f = \frac{nc}{2Nd\sin\theta} \quad n = \pm 1, \pm 2, \ldots \tag{8.14}$$

For this case, the locations of the null lines for both dimensions are parallel with the respective axes as shown in the $\omega - k_y$ diagram in Figure 8-12. The null locations in k_y are the same as in the $\omega - k_x$ diagram, except that they do not shift with frequency. The first null on the frequency axis (f = 2.121 GHz) is also the same frequency as in the $\omega - k_x$ diagram.

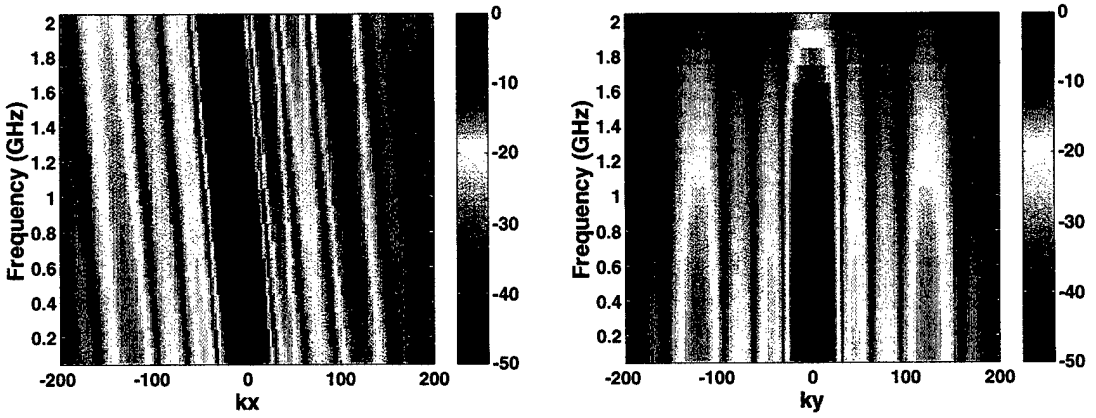

Figure 8-12. ω-β diagrams for the normalized radiated magnetic field at the scan plane for the 4x4 dipole array.

8.6.2 ω-β Diagrams for the 4x4 FSS in the Pyramid

For the actual 4x4 FSS, the $\omega - \beta$ diagrams should have a structure very similar to the dipole array since the array factors are identical. The difference between the geometries is the element factor, which is a hole in a conductor for the FSS and a dipole for the dipole array. In addition, the specular reflection is removed from the FSS results, but its equivalent is not removed from the dipole array results. Thus, the diagrams for the finite FSS should have nulls along the k_x and k_y axes at every 31.4 m^{-1} except where a peak occurs, which is at every $2N^{th}$ null or every 125.7 m^{-1}, and the first null that crosses the frequency axes should be at 2.121 GHz. The $\omega - k_x$ diagram should show a slanted periodic Sinc type structure, and the $\omega - k_y$ diagram should show a rectangular-shaped periodic Sinc type structure similar to those in Figure 8-12.

The computed results are shown in Figure 8-13 to Figure 8-15, and measured results are shown in Figure 8-16 to Figure 8-17. In general, the results agree with the predictions for the nulls,

peaks and the Sinc characteristics in both cross-sections of the spectrum. The null at 2.121 GHz is readily seen in the spectra of the FDTD results and appears to exist in the spectra of the measured results but is difficult to determine because the diagrams of the measured data end near 2 GHz. The spectrum of the dipole array is brighter than that of the FSS results near the frequency axis because the specular has been removed from the FSS results, but its equivalent was not removed from the dipole array results. Other differences in the spectra from that predicted with the dipole array, such as the different behavior in the spectra for the low frequency region (<= 1GHz), are attributed to the use of different elements (dipoles in free space vs holes in metal) and to modeling/measurement errors. In addition, results for the dipole array in Figure 8-12 are for fields observed at s = 0.5 inches, therefore, they should agree better with the scan plane results than those at the FSS surface. Without subtracting the specular equivalent from the dipole results, it is difficult to make precise comparisons, but in general, the evanescent spectrum appears to be relatively low in magnitude at the scan plane for both the dipole and FSS spectra in comparison with the propagating portion of the spectra.

8.6.3 Local Probe Back-Propagation Analysis and the ω-β Diagrams

Beginning with the numerical data, the $\omega-\beta$ diagram of the local back-propagated magnetic field data is shown in Figure 8-15. Comparing it to the $\omega-\beta$ diagram of the FDTD computed data at the FSS (actually 2.5 mm in front of the FSS) in Figure 8-14 shows good agreement, indicating local probe recovered the spectrum at the FSS reasonably well.

Turning to the measurements, the $\omega-\beta$ diagram of the local back-propagated image is shown in Figure 8-17. First, comparing this data with the measured data at the scan plane in Figure 8-16 shows that the local probe amplified the evanescent energy in the $\omega-k_x$ diagram, which is expected for this operation in general. However it is difficult to determine if this was the case for the $\omega-k_y$ cross-section of the spectrum.

A similar behavior is observed in the numerical data, upon comparing the results in Figure 8-13 and Figure 8-15. The change in the $\omega-k_y$ spectrum for the FDTD data from the scan plane to the FSS also did not change much for this cross-section. Thus, the numerical model corroborates this behavior. This result indicates the entire k_x-k_y spectrum is not always significantly changed by the back-propagation operation.

Comparing the local probe back-propagated measured data in Figure 8-17 with the image of the FDTD data at the FSS in Figure 8-14 shows reasonable agreement for both the $\omega - k_x$ results and the $\omega - k_y$ results. This agreement is reasonable considering that a similar level of agreement is seen in the spectra of the fields at the scan plane (Figure 8-13 for the computed results and Figure 8-16 for the measured data). Thus, some of the differences in the spectra of the local probe back-propagated results are due to the differences between the measured and computed data and are not entirely due to artifacts introduced by the local probe.

These results indicate the local probe method can back-propagate the propagating spectrum and a portion of the evanescent spectrum over a band of frequencies for high frequency surface current measurements.

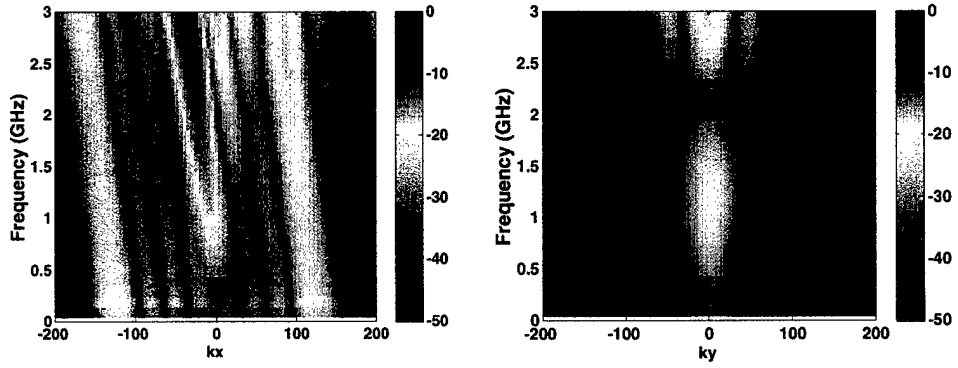

Figure 8-13. ω–β diagrams for the normalized scattered magnetic field at the scan plane computed with FDTD.

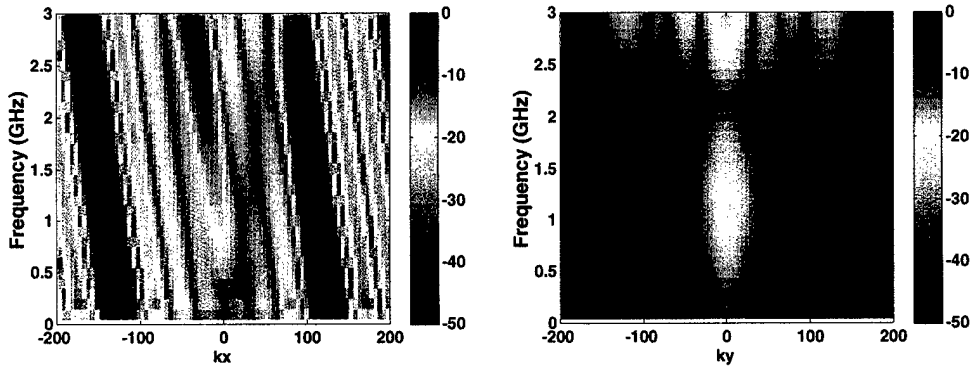

Figure 8-14. ω–β diagrams for the normalized scattered magnetic field at the FSS surface computed with FDTD. (2.5 mm from surface due to FDTD cell size.)

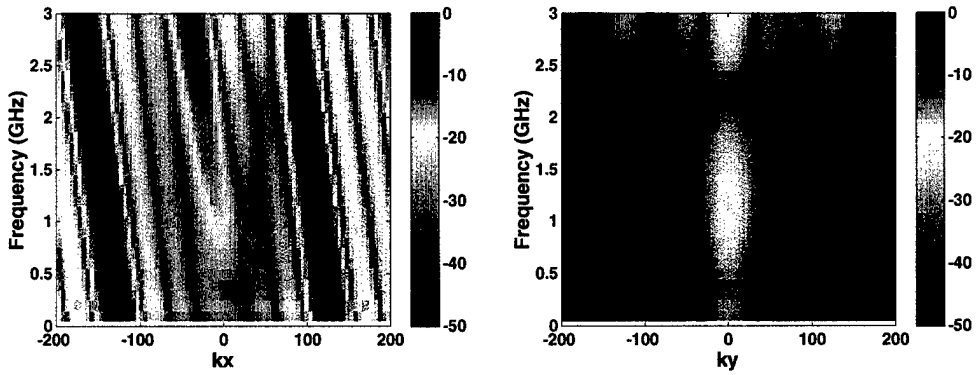

Figure 8-15. ω-β diagrams for the normalized scattered magnetic field computed from the local probe back-propagation of FDTD data at the scan plane.

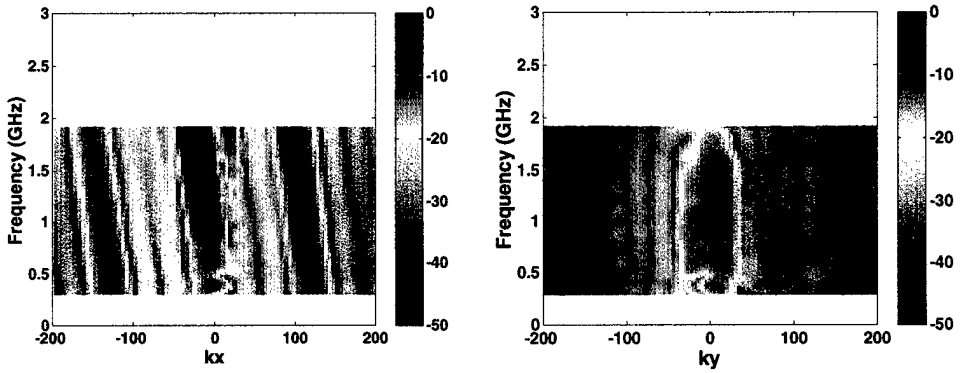

Figure 8-16. ω–β diagrams for the normalized scattered magnetic field measured at the scan plane.

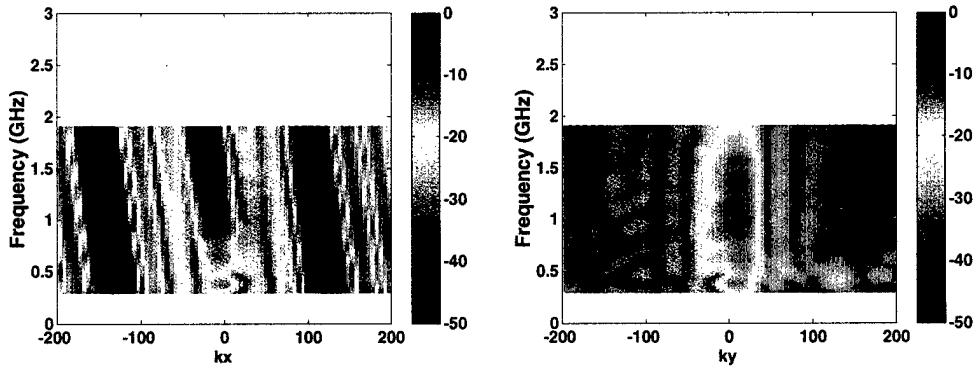

Figure 8-17. ω–β diagrams for the normalized scattered magnetic field at the FSS surface obtained from local probe back-propagation of the measured data at the scan plane.

8.7 Conclusions

The comparisons of the measured data with the computed data indicate the local probe approach can model characteristics of the electromagnetic fields near FSS structures. It is feasible to consider further development of this approach for determining high-frequency characteristics of various structures such as the FSS. For example, the approach can be used to determine FSS/array damage and can provide quality control for repair/maintenance/manufacture of these components.

9 Ship Model

9.1 Introduction

The study of low-frequency characterization with the local probe was carried out with the simple scale model ship shown in Figure 9-1. The goal is to demonstrate the use of the local probe back-propagation method for measuring currents on the ship model which are within the resonance region. The results are compared with numerical results from an FDTD model of the ship. The fields are further analyzed using ω–β diagrams to study their spectra as a function of frequency.

9.2 Ship Model and Measurement System

The actual scale ship model is shown in Figure 9-1, and a sketch of the scale model with the dimensions is shown in Figure 9-2 and Figure 9-3. A duplicate of the ship was employed to simulate the image that would be formed if the ship were on an infinite conducting plane (ocean). A horn antenna was used to illuminate the ship with a vertically polarized incident wave at a 45 degree angle of incidence. The local probe scan plane was $s = 0.5$ inches in front of the model. The sample spacing was $d = 0.25$ inches. In this study, the scattered magnetic field component that is co-polarized with the incident magnetic field was measured at the scan plane and then back-propagated to the ship surface with the local probe.

After scanning the field 0.5 inches from the surface, it was processed, and then the local probe back-propagation method was employed to reconstruct the currents on the surface of the ship. In the following discussions the terms 'scattered magnetic field' and 'surface current' are used interchangeably. It is to be understood that the term 'surface current' refers only to the portion of the field on the observation plane that is over the ship surface whereas the term scattered magnetic field can refer to the field over the whole observation plane, which is the same size as the scan plane.

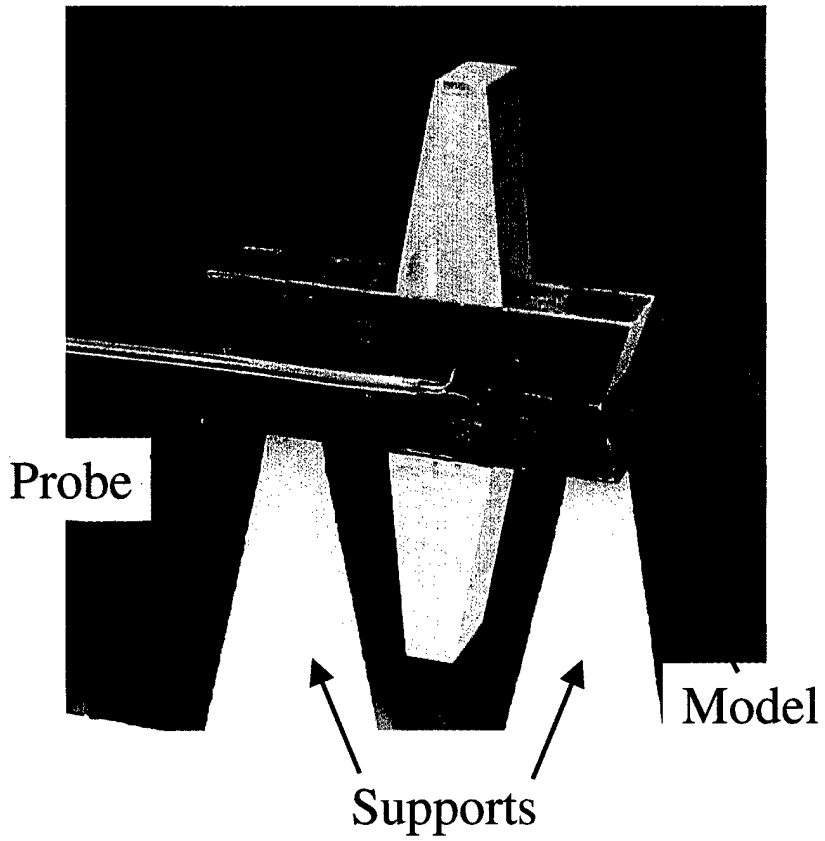

Figure 9-1. Measurement system showing probe and scale model of ship.

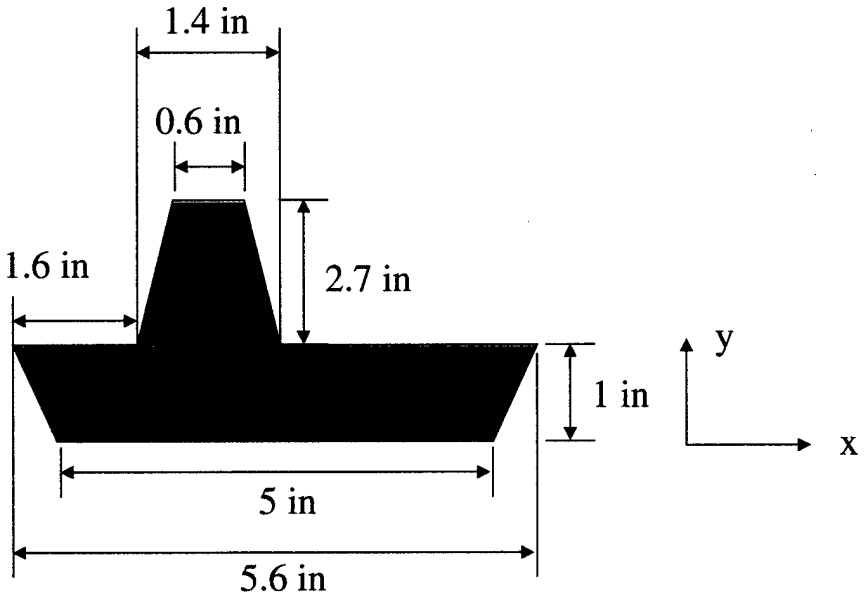

Figure 9-2. Model of ship with dimensions. Image is not shown.

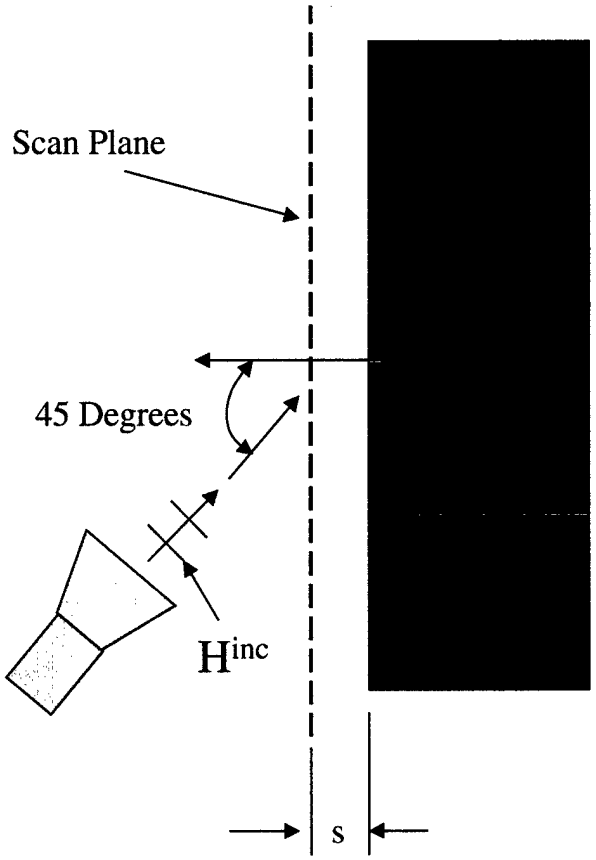

Figure 9-3. Top view of measurement system.

9.3 RCS Model

The purpose of this study is to demonstrate the feasibility of employing the local probe back-propagation technique for measuring the surface currents that contribute to the RCS in the resonance region. To show how the RCS is related to the surface currents for the resonance region, the peak current magnitude (measured and computed) and the computed RCS were obtained for the model ship and are shown in Figure 9-4. This comparison shows the RCS level closely follows the peak current magnitude in the resonance region. Thus, knowledge of the surface currents in the resonance region will provide information on the RCS behavior. For this example, these figures indicate the maximum RCS in the band of measured frequencies occurs at approximately 0.7 GHz. Therefore, we studied the local probe back-propagation method for 0.7 GHz. In addition, we studied the spectra over the entire valid frequency range with an $\omega - \beta$ analysis.

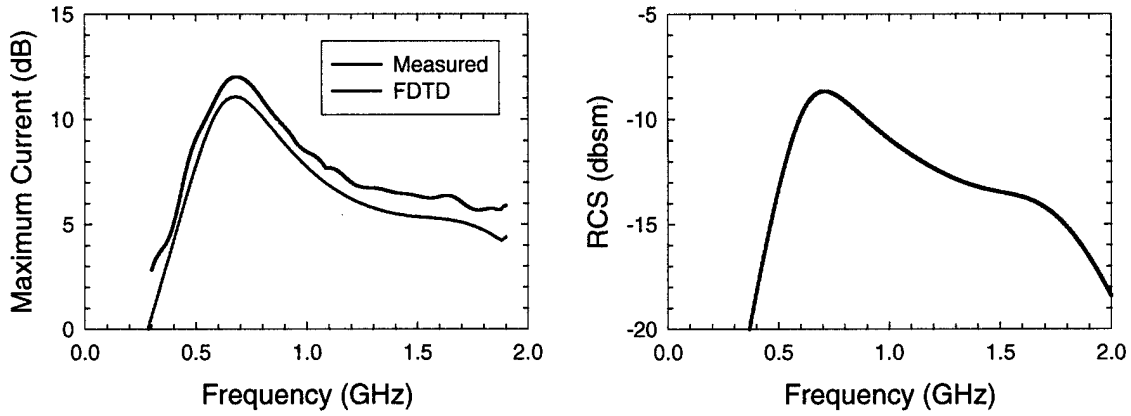

Figure 9-4. Maximum current tracks the RCS in the resonance region.

9.4 Numerical Simulation

The FDTD method was employed for the numerical modeling of the surface current measurements. The FDTD model of the ship is shown in Figure 9-5. The ship was discretized using cubical cells of 0.1 inch per side. The horn excitation was not modeled as it would require too much memory and CPU time. Instead, a plane wave injector box surrounding the model was used to launch a vertically polarized incident plane wave at 45 degrees. It was assumed the spatial field variation from the horn antenna is sufficiently small over the scale model of the ship that it could be approximated with the incident plane wave model in the FDTD analysis.

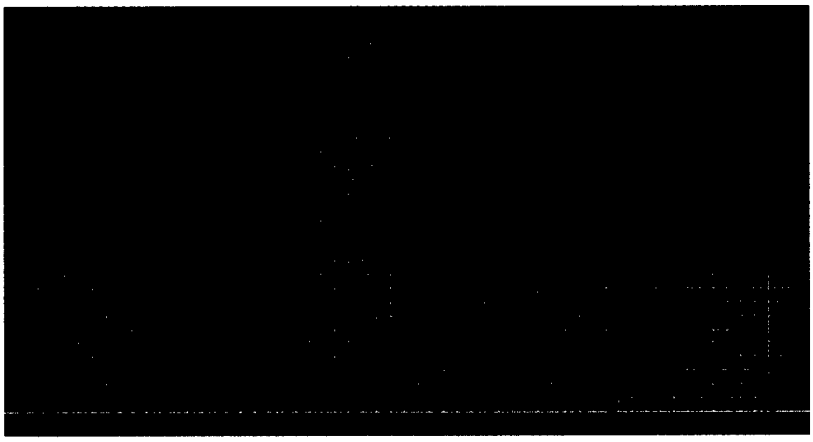

Figure 9-5. FDTD model of scale ship geometry.

The numerical model was used for computing the magnetic field at both the scan plane, 0.5 inches from the ship, and the ship surface. Due to FDTD cell discretization, the magnetic fields were actually 0.05 inches away from these values of $s = 0.5$ and $s = 0.0$. The 0.05 inch discrepancy

from the actual measurement configuration is not very significant as it is small compared to the ship dimensions and the wavelengths of interest. Considering the evanescent spectrum, this dimension is 1/20 λ or less for spatial frequencies less than $k_x = 247$. Other errors such as the magnetic field sample spacing and local probe sample spacing will be more significant than this error at the higher evanescent portion of the spectrum. Thus, we will not further discuss the relatively minor errors introduced by this discretization.

The results of the numerical simulation are shown in Figure 9-6 to Figure 9-8 in terms of images of the field magnitude at the scan plane and ship surface. (Scan plane and ship surface refer to the actual distances of 0.5 inches and 0 inches, respectively.) In Figure 9-6, the results indicate a strong magnetic field or resonance at the mast of the model ship.

The local probe back-propagation technique was employed to reconstruct the surface current on the ship surface from the magnetic fields on the scan plane. An image of the magnitude of the local probe weights is shown in Figure 9-7. For this measurement, the local probe consisted of a square array of 7x7 weights spaced 0.2 inches or 0.012 λ apart at 0.7 GHz. The weights were computed using the least square means procedure over a plane of 23 x 23 test points.

An image of the magnetic fields/surface currents reconstructed with the local probe is shown in Figure 9-8 and compared with the surface magnetic fields computed from the FDTD method. These images show the surface fields are dominated by a dipole like structure. The reconstructed surface fields are similar to the FDTD computed results in that both indicate the leading edge of the ship mast has a strong current/field component and both show similar features in general.

One source of error in the results is due to the differences in magnetic field sampling intervals between FDTD and the local probe. With a local probe weight spacing of 0.2 inches, the results will be less sharp than the FDTD field sample spacing of 0.1 inches. If the local probe weights were placed closer together, the image would be sharper, but the local probe back-propagation procedure becomes very sensitive to inaccuracies in the higher evanescent spectrum, resulting in the image being washed out by large magnitude noise. In conclusion, these results show the technique should work, provided the local probe does not back-propagate too much of the inaccurate portion of the high evanescent spectrum.

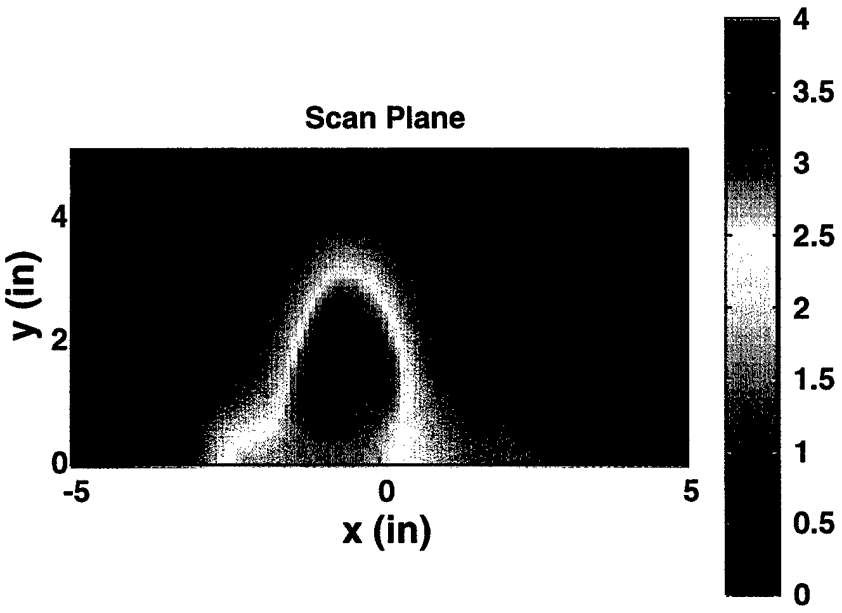

Figure 9-6. Dominant magnetic field computed at the scan plane at 0.7 GHz.

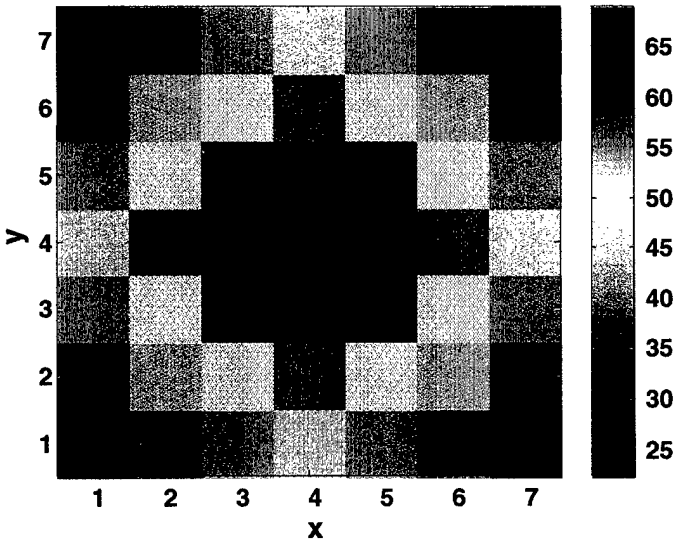

Figure 9-7. Local probe weight magnitudes in dB.

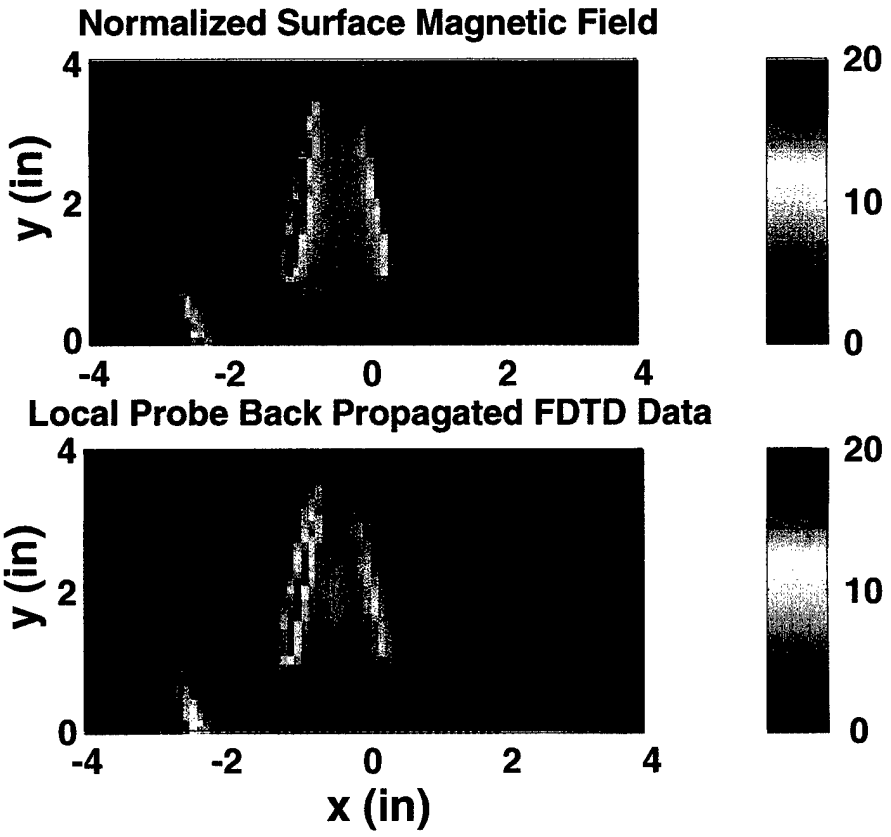

Figure 9-8. Magnetic field at the surface of the ship.

9.5 Measurement Results

The results of the measurements are shown in Figure 9-9 to Figure 9-12. First, the scattered magnetic field at the scan plane is shown, and then the field at the surface of the scale model is shown. The results will be compared with those obtained with FDTD. The image of the magnitude of the measured scattered magnetic field is compared with the FDTD data at the scan plane in Figure 9-9. Considering that the measured data is sampled at 0.25 inches whereas the FDTD data is sampled at 0.1 inches, the agreement is good. Both show the same overall field distribution, the main differences being that the measured results are more discretized due to the larger sample spacing than used for the computed results.

A 7x7 square local probe array with a weight spacing of 0.5 inches (0.03 λ) was employed to reconstruct the surface currents from the field measured at the scan plane. The results are compared to the FDTD data obtained at the ship surface in Figure 9-10. Both images indicate the dipole-like

resonance of the leading edge of the mast, but the lower sampling density of the measurements results in a less defined surface field reconstruction.

To provide a better comparison, cross-sections of the surface fields from Figure 9-10 are shown in Figure 9-11. These results show reasonable agreement between measured and predicted results except for the sharp features. To study the effect of sampling on these results, the sample density of the FDTD data was reduced to an equivalent density of the measurements, with the fields at a sample spacing of 0.25 inches. Then, this data was back-propagated using a local probe identical to the one used with the measurement data. The surface field reconstructed with this data is compared to that reconstructed from the measurement data in Figure 9-12. This less densely sampled FDTD data compares better with the measured results than the more densely sampled results shown in Figure 9-10. This comparison demonstrates that part of the discrepancy seen in Figure 9-10 is due to the differences in sample spacing between the results.

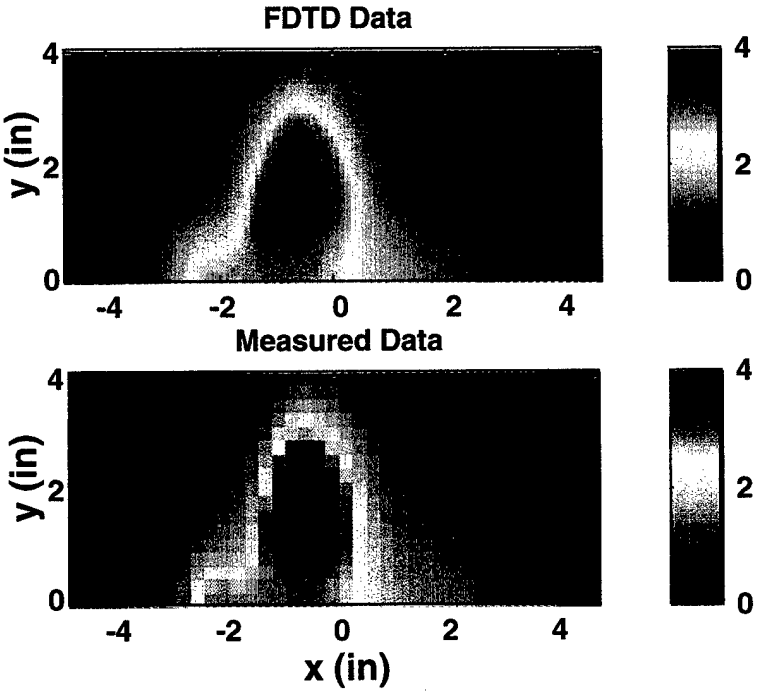

Figure 9-9. Measured data and computed data for the scattered magnetic field at the scan plane.

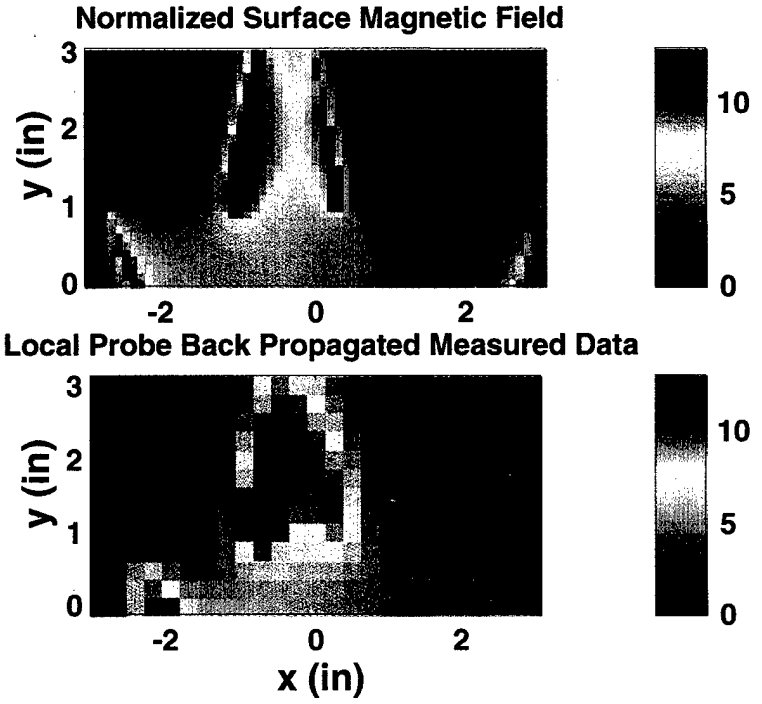

Figure 9-10. Magnetic fields at the ship surface from computed data and reconstructed with the local probe back-propagation technique.

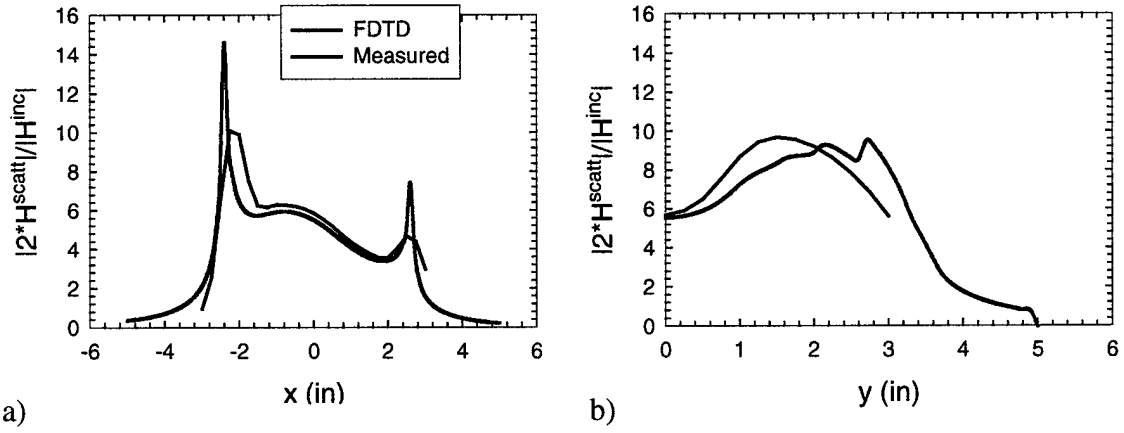

Figure 9-11. Cross sections of the surface magnetic field from Fig. 10. (a) Horizontal cut at image plane. (b) Vertical cut at center of ship.

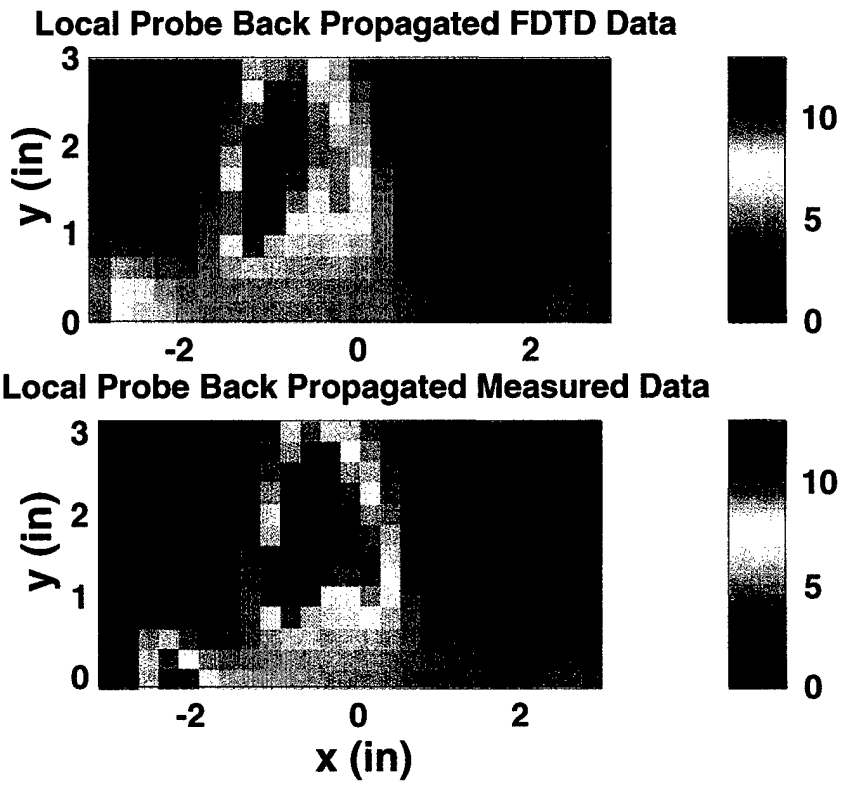

Figure 9-12. Surface fields reconstructed from local probe back-propagation from FDTD data averaged over 0.25 inch spacing and measured data.

9.6 Spectra for the Model Ship

The $\omega-\beta$ diagrams of the measured and computed fields show the evanescent and propagating mode behavior of the scattered magnetic fields at the scan plane and ship surface. The evanescent modes are expected to be stronger closer to the ship surface than at the scan plane. Two cross-sections of the $\omega-\beta$ cube of data are studied. One is for $k_y = 0$ and the other is for $k_x = 0$.

9.6.1 Modes of the Numerical Results

The $\omega-\beta$ diagrams of the FDTD data at both the scan plane and ship surface are shown in Figure 9-13 and Figure 9-14. The evanescent fields are larger at the surface than at the scan plane for the $\omega-k_x$ plots but are only slightly larger for the $\omega-k_y$ plots.

9.6.2 Modes of the Measured Results

The $\omega-\beta$ diagram of the measured data at the scan plane is shown in Figure 9-15. Comparing it with that of the FDTD data in Figure 9-13, reasonable agreement is seen in the mode

structure. The $\omega-\beta$ diagram of the measured data at the ship surface is shown in Figure 9-16. Comparing it with the $\omega-\beta$ diagram of the FDTD data in Figure 9-14 shows reasonable agreement with the FDTD data for the $\omega-k_x$ plot. For the $\omega-k_y$ plots, the results are similar but the evanescent fields of the measurements have a different structure than the FDTD results. These differences are partly due to the differences in sampling densities of the two results.

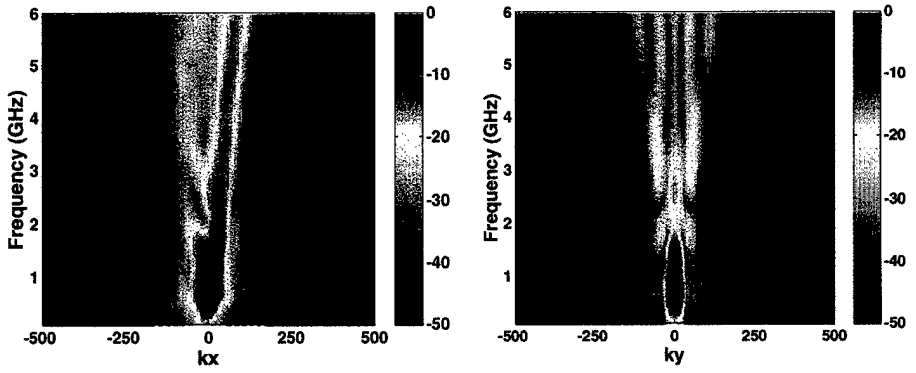

Figure 9-13. FDTD data at the scan plane.

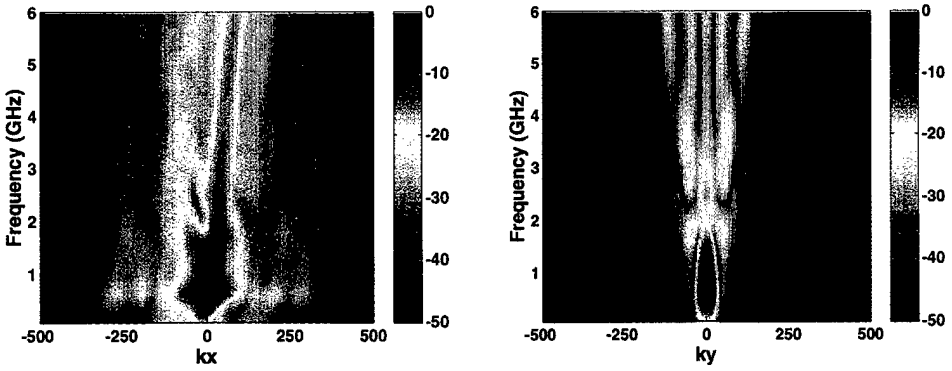

Figure 9-14. FDTD data at the surface of the ship.

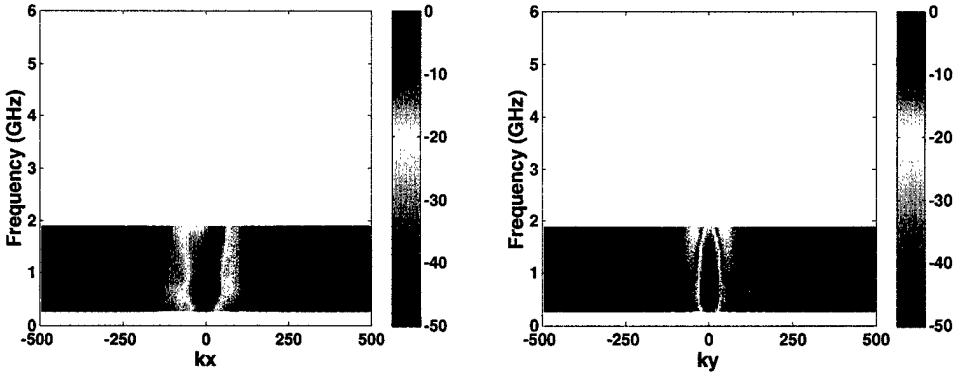

Figure 9-15. Measured data at the scan plane.

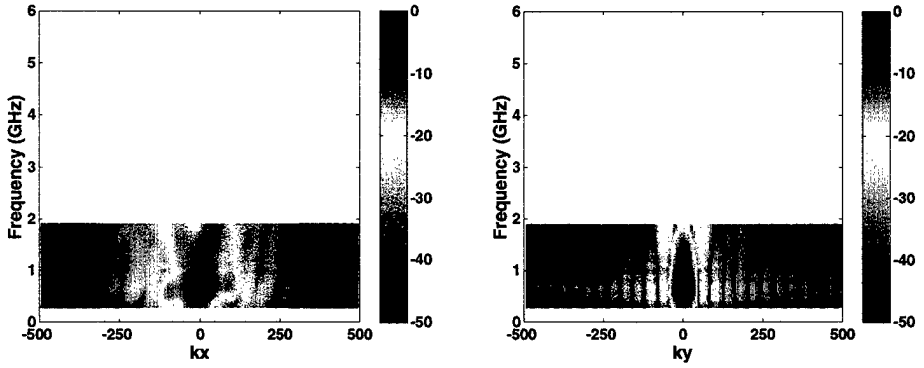

Figure 9-16. Measured data local probe back-propagated from the scan plane to the ship surface.

9.7 Conclusions

This study demonstrated the use of the local probe back-propagation technique for low-frequency resonance current reconstruction. The results of the local probe method agreed reasonably well in comparison with data generated numerically with FDTD. Most of the discrepancies were due to the lower sampling level of the measurements which were sampled at 0.25 inches whereas the FDTD data was sampled at 0.1 inches.

The $\omega - \beta$ diagrams showed the scattered magnetic field was concentrated at the propagation region at the scan plane, but at the ship surface the evanescent modes were significant,

especially for the $\omega - k_x$ cross section. A slight periodicity in the scattered magnetic field is seen mainly in the $\omega - k_y$ diagrams due to resonance in the structure.

10 Angled Back-Propagation

10.1 Introduction

The back-propagation method using measured magnetic field components on a plane parallel to the surface works well in reconstructing the current. In this section, the goal is to determine the feasibility of an angled back-propagation technique, i.e., measuring currents on an oblique surface. Under some measurement conditions, it may be more convenient to place the measurement plane at an angle with respect to the surface instead of parallel to it as shown in Figure 10-1.

10.2 Theory

The approach is initially developed for the two-dimensional case shown in Figure 10-2. The strip of current is constant in y. In this discussion of the 2-D analysis, the current will be referred to as a line of current in the $x-z$ plane, and the measurement surface will be referred to as a measurement line in the $x-z$ plane. The line of current is tilted at an angle, θ, with respect to the measurement line. The measurement window length is w, the current strip length is d, and the perpendicular distance from the measurement line to the center of the current is s. To use the plane wave spectrum (PWS) and the Fourier transform technique, the geometry must be expressible in rectangular coordinates. Thus, two coordinate systems will be used: the source (primed) coordinates in which the current line is parallel with the x' axis, and the measurement (unprimed) coordinates in which the measurement line is parallel with the x axis. (See Figure 10-3) The unprimed coordinates are a rotation through an angle, θ, of the primed coordinate system.

To study angled back-propagation, a strip of current of width d is placed on the primed axes at $z'=0$. Next, the magnetic field at the measurement line is computed via forward propagation. That is, the magnetic field due to the current is forward propagated in the source coordinates (primed coordinates) to the measurement line and then the magnetic field tangential to the measurement line is obtained. (See Figure 10-3) The magnetic field tangential to the measurement line is given by

$$H_x^m(x,z) = H_{x'}^m(x,z)\cdot\cos\theta + H_{z'}^m(x,z)\cdot\sin\theta \tag{10.1}$$

where

$$H_{x'}^{m}(x',z') = \int_{-\infty}^{\infty} \tilde{J}_y(k_{x'}) e^{-jk_{z'}z'} e^{-jk_{x'}x'} dk_{x'} \tag{10.2}$$

and

$$H_{z'}^{m}(x',z') = -\int_{-\infty}^{\infty} \tilde{J}_y(k_{x'}) \frac{k_{x'} e^{-jk_{z'}z'} e^{-jk_{x'}x'}}{k_{z'}} dk_{x'} \tag{10.3}$$

Only the tangential component of the magnetic field along the measurement line is necessary because the other component can be obtained with Gauss's law. However, since the measurement line is at an angle with respect to the source line, the tangential magnetic field component is computed using both H_x and H_z as shown in (1).

The integral in (3) has an integrable singularity at $k_x' = \pm k_0$, since $k_z' = 0$ at these values. (Note: If the strip width is an integral multiple of wavelengths, the numerator is zero for $k_x' = \pm k_0$, and the integral is well behaved for this case.) This singularity is accurately handled by subtracting it from (3), so that the resultant integral can be numerically integrated and then adding back the contribution, which, in this case, is a closed form integral [29].

The back-propagation algorithm is carried out in a similar fashion in the unprimed coordinates as shown in Figure 10-4. The back-propagated magnetic field components at the source line are

$$H_x^s(x,z) = \int_{-\infty}^{\infty} \tilde{f}(x,k_x) \tilde{H}_x^m(k_x) e^{-jk_z(z_s(x)-z_m(x))} e^{-jk_x x} dk_x \tag{10.4}$$

and

$$H_z^s(x,z) = -\int_{-\infty}^{\infty} \tilde{f}(x,k_x) \tilde{H}_x^m(k_x) \frac{k_x e^{-jk_z(z_s(x)-z_m(x))} e^{-jk_x x}}{k_z} dk_x \tag{10.5}$$

where

$$\tilde{f}(k_x,x) = \begin{cases} 1.0, & k_x \le \alpha k_{cut} \\ e^{-(k_x-\alpha k_{cut})^2/\gamma^2}, & k_x > \alpha k_{cut} \end{cases} \tag{10.6}$$

with

$$\gamma = (1-\alpha)\sqrt{\frac{k_{cut}}{|z_s(x) - z_m(x)|}}. \tag{10.7}$$

The surface current is obtained from the magnetic field tangential to the source line, and it is given by

$$J_y(x') = H_x^s(x') \cdot \cos\theta - H_z^s(x') \cdot \sin\theta \tag{10.8}$$

Eq. (5) has an integrable singularity which is handled the same was as for Eq. (3). The filter given by Eqs (6)-(7) is necessary to dampen the inaccurate evanescent modes at the higher spectral frequencies which can become practically infinite when back-propagated, making the integrals in (4) and (5) invalid. The filter is flat out to αk_{cut}, and then falls off rapidly with a Gaussian-shaped roll-off. This filter dampens the noise without adding excessive ringing as would occur for an abrupt truncation (rectangular filter) of the fields to zero. The values of α and k_{cut} determine the starting point and, in conjunction with γ and s, the sharpness of the roll off. A value of $\alpha \approx 0.9$ or greater causes the filter to fall rapidly beyond k_{cut}, approximating a rectangular filter, and a value of $\alpha \approx 0.5$ causes the filter to behave similar to a Hamming window. A value of $\alpha \approx 0.7$ was found to be a good compromise. The parameter, k_{cut}, is chosen according to the distance of the measurement line from the source line. It is initially set to a large value for the portion of the measurement line that is closest to the source line, which in these simulations was at a distance of 0 since the measurement line intersected the source line. Then, the value of k_{cut} was reduced at 1 λ intervals to k_0 at which point the evanescent modes are completely removed. The values of k_{cut} are chosen by observation of the back-propagated spectrum for this study at the 1 λ intervals. For angles of 10 degrees and higher, the value of k_{cut} generally changed over 2 λ from its maximum value to the minimum value of k_0. Linear interpolation was employed to adjust k_{cut} between the values set at 1 λ intervals.

10.3 Verification of Numerical Technique

This approach was verified by comparing the forward propagated magnetic field for the geometry in Figure 10-3 with $\theta = 30$ and $s = 0.8\lambda$ to that computed using the vector potential

approach [30]. Figure 10-5 shows the results agree well. A convergence study was also done to determine the sample spacing and number of points. A sample spacing of $\Delta x = 0.02\lambda$ and 2^{12} points were found to be sufficient for providing results that were well converged. One point to note is that the difference integrands formed by subtracting the singularity from the kernels of (3) and (5) fall off slowly, and they need further study if this technique is employed. For the purposes of this feasibility study though, since the results agreed with the vector potential technique in the forward propagation direction, we assumed these integrals were sufficiently converged for both forward and back-propagation directions.

10.4 Back-Propagation Study

The approach was studied for the case where $\theta = 10$ and $s = 0.2\lambda$. These dimensions were assumed to be the typical ones for which the method would be employed. The magnetic field was propagated to the measurement plane and then back-propagated to the source plane. The results are shown in Figure 10-6. A spectral filter with a varying k_{cut} filter, whose values are indicated in the figure, was chosen to back-propagate the magnetic field on the angled line. The reconstructed current is more accurate (it has higher spectral content) for the current distribution along the portion of the line closest to the angled scan line, and it is poorest (it has lower spectral content) for the portion furthest from the scan line. This figure also shows the current reconstructed from mainly the propagating portion of the magnetic field on the angled measurement line. Even though only propagating modes were employed, the reconstructed current is still asymmetrical. These results show that the angled back-propagation approach produces poor results. The reconstructed current is not symmetric (even though the original current distribution is symmetric) and contains significant erroneous ripples even without additional real world complications such as realistic measurement noise levels.

Several reasons for the poor operation are the following:

i) The reconstructed current details depend upon accurately measuring the evanescent energy. With an angled measurement line or plane, the evanescent energy is not captured uniformly across the line due to the varying distance of the measurement line from the current and consequently, the back-propagated results will by asymmetric even for symmetric current distributions.

ii) Significant contributions of energy to the surface current may be missed if the angled plane or line is not sufficiently big enough. Ideally, the measurement surface must enclose the current completely. This approach relys on the approximation that the majority of the energy radiated by the current is captured by the flat measurement surface. For the angled plane, it is not clear this will always be the case.

iii) The measurement surface must always be to one side of the infinte plane containing the surface current. If it is not, confusion results in how to back-propagate the field using the plane wave spectrum because the portion of the pws due to fields behind the surface current must be forward propagated back to the surface. Once the fields on the entire line are transformed into the spectral domain, it is unclear how to separate those components due to the fields which must be forward propagated.

This technique did work, though, provided the measurement line was angled by only a few degrees with respect to the line of current. However, we did not perform a parameter study to determine the operation range since it could not work well for the typical case studied above.

10.5 Conclusions

This study indicates that back-propagation from an angled line produces results that are not accurate enough for determining the electrical current for a typical scenario in which the measurement line is at an angle of 10 degrees with respect to the current line. The technique works poorly because it captures the evanescent energy in a nonsymmetrical fashion, and the evanescent energy contributions are rapidly lost for the portion of the line that is the furthest from the current. Because the two dimensional technique did not work well, the full three dimensional approach was not developed. In conclusion, the full back-propagation method works best when the measurement surface is parallel or nearly parallel to the surface of the current.

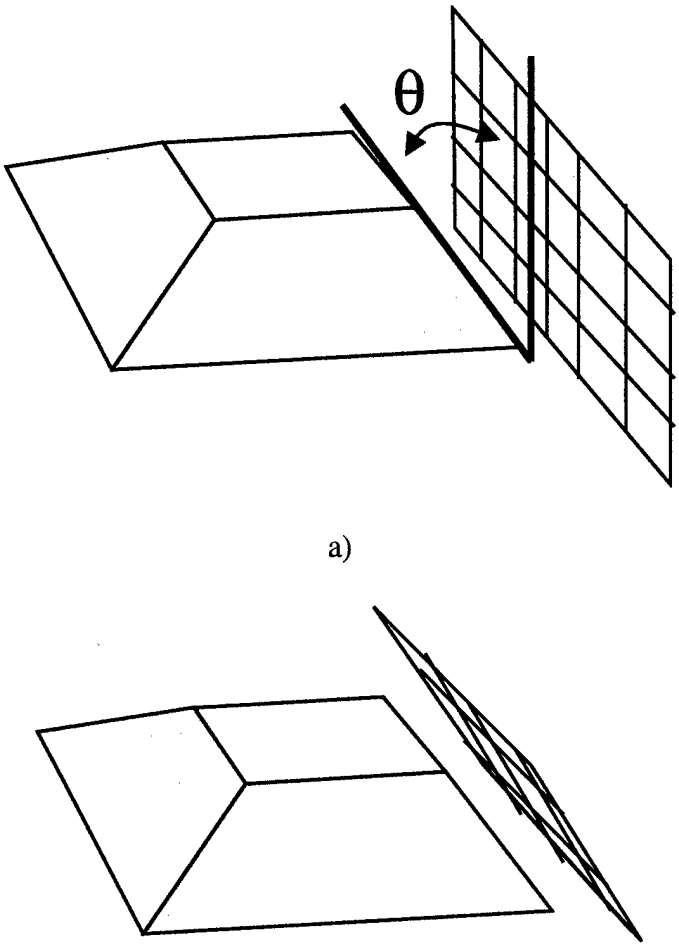

Figure 10-1. a) Measurement plane tilted with respect to surface. b) Measurement plane parallel with surface.

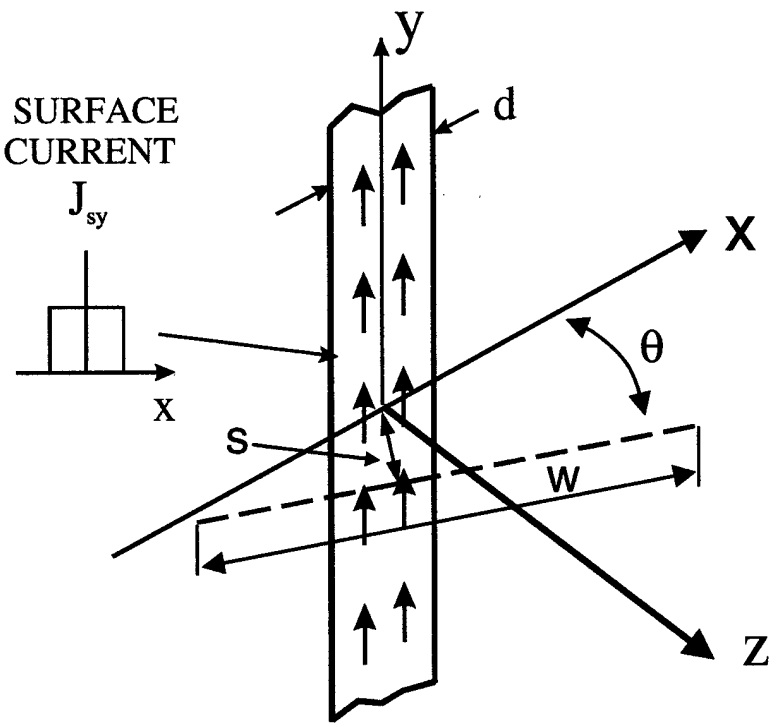

Figure 10-2. Two dimensional geometry for the development of angled back-propagation technique.

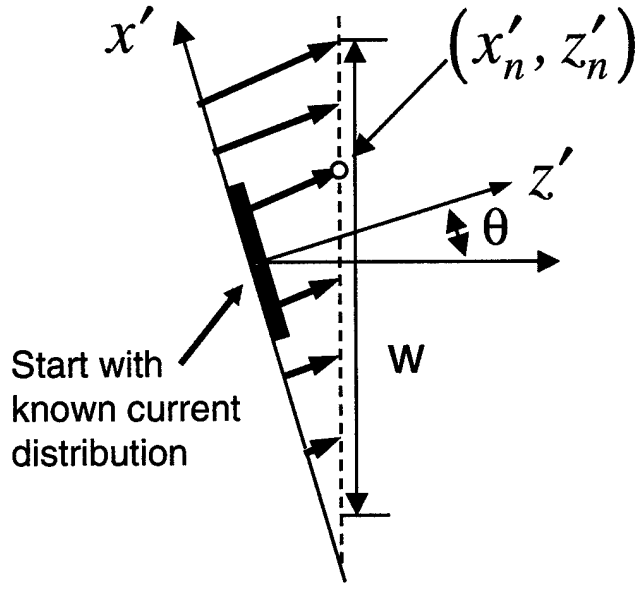

Figure 10-3. Forward propagation to measurement plane.

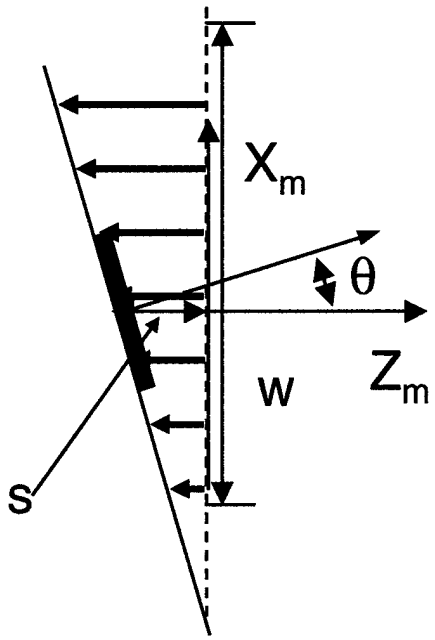

Figure 10-4. Back-propagation to current line.

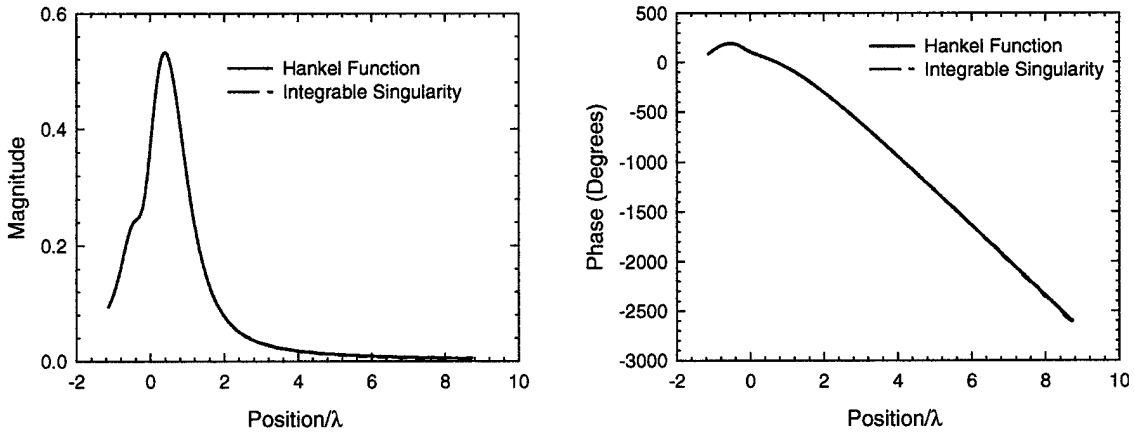

Figure 10-5. Comparison of magnetic field at measurement line computed with PWS and with the vector potential approach for $\theta = 30$, $s = 0.8\ \lambda$ and $d = 1.5\ \lambda$.

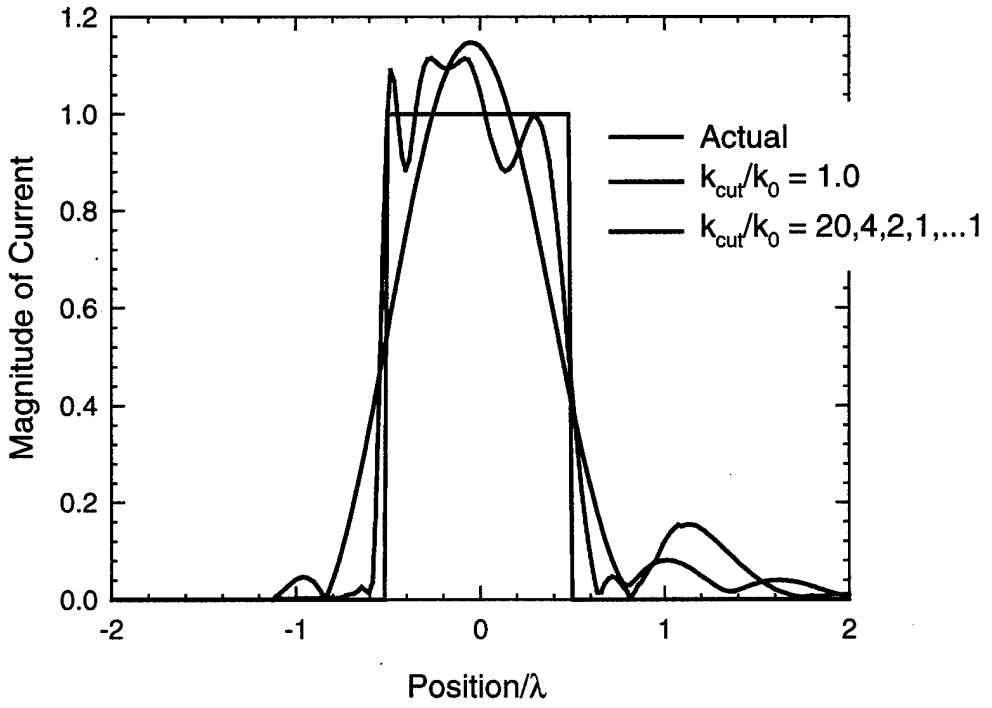

Figure 10-6. Current reconstructed with angled back-propagation approach for $\theta = 10$, s = 0.2 λ and d = 1.0 λ. The spectral filter k_{cut} values are shown in the figure.

11 References

[1] J. D. Maynard, E. G. Williams, and Y. Lee, "Nearfield acoustic holography: I. Theory of generalized holography and the development of NAH," *J. Acoust. Soc. Am.* Vol. 78, pp. 1395–1413, Oct. 1985.

[2] E. G. Williams and J. D. Maynard, "Holographic imaging without the wavelength resolution limit," *Phys. Rev. Let.* Vol. 45, pp. 554-557, 1980.

[3] E. G. Williams and H. D. Dardy, "Generalized nearfield acoustical holography for cylindrical geometry: Theory and experiment," *J. Acoust. Soc. Am.* Vol. 81, pp. 389-407, February 1987.

[4] A. Sarkissian, C. F. Gaumond, E. G. Williams and B. H. Houston, "Reconstruction of the acoustic field over a limited surface area on a vibrating cylinder," *J. Acoust. Soc. Am.*, VOl. 93, pp. 48-54, Jan. 1993.

[5] M. G. Guler and E. B. Joy, "High resolution spherical microwave holography," *IEEE Trans. Antennas Propagat.*, vol. 43, No. 5, pp. 464-472, May 1995.

[6] J. G. Maloney, M. P. Kesler and E. J. Kuster, "Localized short-pulse scattering from coated cylindrical objects: experimental measurements and numerical models," in: *Ultra-Wideband Short-Pulse Electromagnetics 2*, L. Carin and L. B. Felsen, ed., Plenum Press, New York, (1995).

[7] M. P. Kesler, J. G. Maloney, E. J. Kuster, P. G. Friederich and B. L . Shirley, "RCS determination from localized short-pulse scattering measurements: theory and experiment," in: *Ultra-Wideband Short-Pulse Electromagnetics 3*, C. E. baum, L. Carin and A. P. Stone, ed., Plenum Press, New York, (1997).

[8] A. Taflove, *Computational Electromagnetics: The finite-difference time domain method,* Artech House, Inc., Norwood, MA, 1995.

[9] G. S. Smith, *An Introduction to Classical Electromagnetic Radiation,* Cambridge University Press, N.Y., N.Y., 1997.

[10] M. P. Kesler, J. G. Maloney and E. J. Kuster, "Surface current determination from localized scattering measurements," *PIERS, Progress in Electromagnetics Research Symposium Proceedings*, pg. 148, July, 1997.

[11] H. Whiteside, "Electromagnetic Field Probe," Cruft Laboratory Technical Report No. 377, Harvard Univ., 1962.

[12] G. S. Smith, *An Introduction to Classical Electromagnetic Radiation,* Cambridge University Press, New York, 1997.

[13] J. D. Maynard, E. G. Williams, and Y. Lee, "Nearfield acoustic holography: I. Theory of generalized holography and the development of NAH," *J. Acoust. Soc. Am.* Vol. 78, pp. 1395–1413, Oct. 1985.

[14] E. G. Williams and J. D. Maynard, "Holographic imaging without the wavelength resolution limit," *Phys. Rev. Let.* Vol. 45, pp. 554-557, 1980.

[15] E. G. Williams and H. D. Dardy, "Generalized nearfield acoustical holography for cylindrical geometry: Theory and experiment," *J. Acoust. Soc. Am.* Vol. 81, pp. 389-407, February 1987.

[16] A. Sarkissian, C. F. Gaumond, E. G. Williams and B. H. Houston, "Reconstruction of the acoustic field over a limited surface area on a vibrating cylinder," *J. Acoust. Soc. Am.*, Vol. 93, pp. 48-54, Jan. 1993.

[17] M. G. Guler and E. B. Joy, "High resolution spherical microwave holography," *IEEE Trans. Antennas Propagat.*, Vol. 43, No. 5, pp. 464-472, May 1995.

[18] E. S. Gillespie, Guest Ed., "Special issue on near-field scanning techniques," *IEEE Trans. Antennas Propagat.*, Vol. 36, pp. 725-901, June 1988.

[19] W. Chujo, T. Ito, Y. Hori, and T. Teshirogi, "Surface accuracy measurement of a deployable mesh reflector by planar near-field scanning," *IEEE Trans. Antennas Propagat.*, Vol. 36, pp. 879-883, June 1988.

[20] J. J. Lee, E. M. Ferren, D. Pat Woollen, and K. M. Lee, "Near field probe used as a diagnostic tool to locate defective elements in an array antenna," *IEEE Trans. Antennas Propagat.*, Vol. 36, pp. 884-889, June 1988.

[21] C.-S. Wey, A. Xu, M. Mostafavi, "Near-field parameter variations and their effect upon reconstruction of antenna aperture excitations," *Antennas and Propagation International Symposium Digest*, June 24-28, 1991, London, Ontario, Canada, vol. 3, pp. 1454-1457.

[22] M. Kanda, "Standard probes for electromagnetic field measurements," *IEEE Trans. Antennas Propagat.*, vol. 41, pp. 1349 - 1364,.October 1993.

[23] G. Zhou and G. S. Smith, "An accurate theoretical model for the thin-wire circular half-loop antenna," *IEEE Trans. Antennas Propagat.*, vol. 39, pp. 1167 - 1177,.August 1991.

[24] R.W. P. King and G. S. Smith, *Antennas in Matter: Fundamentals, Theory and Applications.* Cambridge, MA: MIT Press, 1981.

[25] H. Whiteside and R. W. P. King, "The loop antenna as a probe," *IEEE Trans. Antennas Propagat.*, vol. 12, pp. 291 – 297,.May 1964.

[26] Cdr. C. W. Harrison, Jr., "Qualitative analysis of loop antenna behavior in linearly and elliptically polarized electric field," *J. Am. Soc. of Naval Engineers*, pp. 369 – 374, May, 1957.

[27] A. Papoulis, *Probability, Random Variables, and Stochastic Processes,* New York, New York: McGraw-Hill, Inc., 1965.

[28] E.F. Knott, J. F. Shaeffer, and M. T. Tuley, *Radar Cross Section.* Norwood MA: Artech House. 1993.

[29] W. H. Press, S. A. Teukolsky, W. T. Vetterling and B. P. Flannery, *Numerical Recipes in C, The Art of Scientific Computing Second Edition.* New York, NY: Cambridge University Press, 1988.

[30] R. F. Harrington, *Time-Harmonic Electromagnetic Fields.* New York, NY: McGraw-Hill Co., 1961.